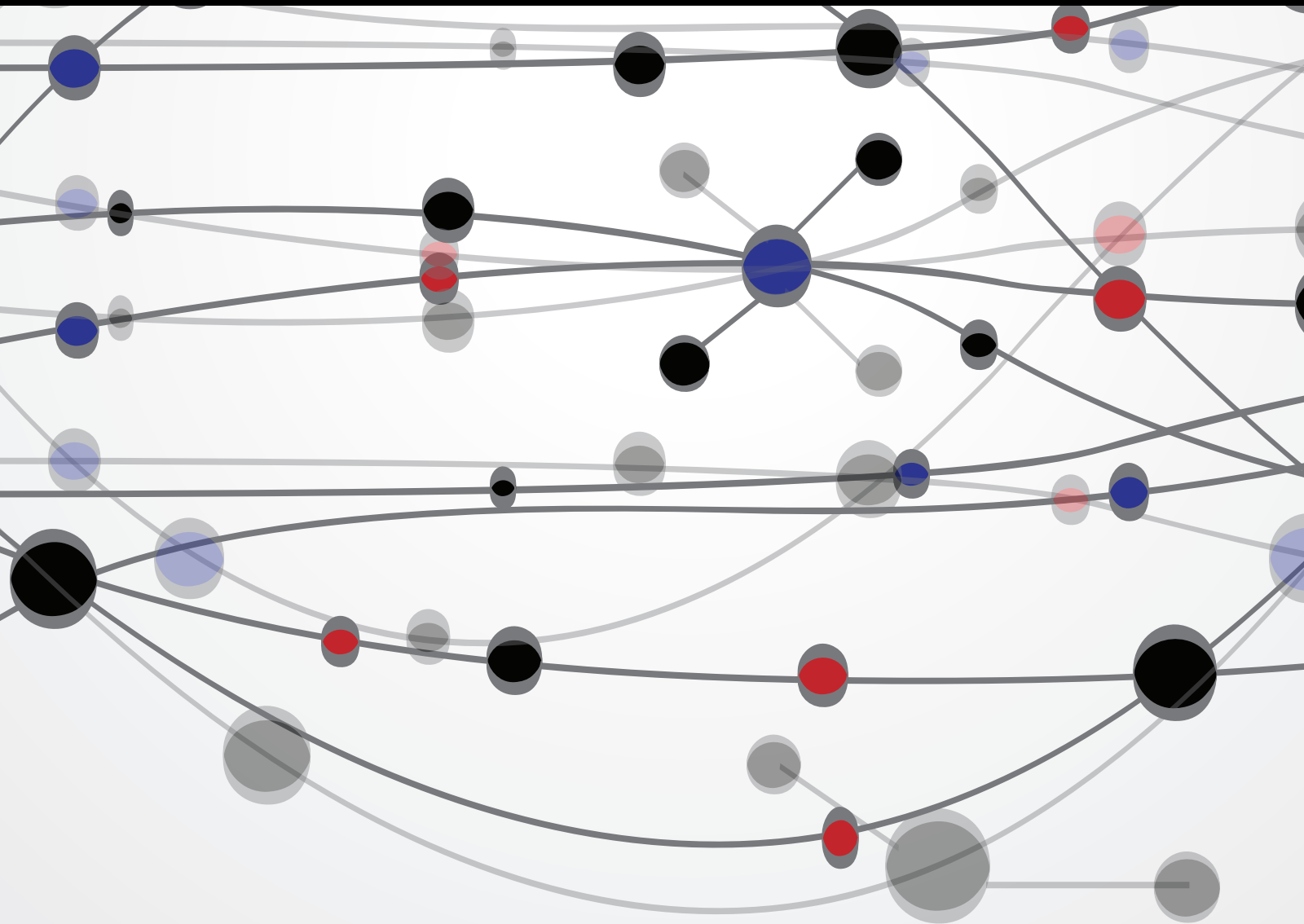


# Modeling, Control, and Optimization Technologies in Electric Drive Vehicles

Guest Editors: Hongwen He, Suleiman M. Sharkh, Caiping Zhang, Xuan Zhou, and Rui Xiong





---

**Modeling, Control, and Optimization  
Technologies in Electric Drive Vehicles**

The Scientific World Journal

---

**Modeling, Control, and Optimization  
Technologies in Electric Drive Vehicles**

Guest Editors: Hongwen He, Suleiman M. Sharkh,  
Caiping Zhang, Xuan Zhou, and Rui Xiong



---

Copyright © 2015 Hindawi Publishing Corporation. All rights reserved.

This is a special issue published in "The Scientific World Journal." All articles are open access articles distributed under the Creative Commons Attribution License, which permits unrestricted use, distribution, and reproduction in any medium, provided the original work is properly cited.

# Contents

**Modeling, Control, and Optimization Technologies in Electric Drive Vehicles**, Hongwen He, Suleiman M. Sharkh, Caiping Zhang, Xuan Zhou, and Rui Xiong  
Volume 2015, Article ID 730347, 2 pages

**Analysis of Ageing Effect on Li-Polymer Batteries**, Simone Barcellona, Morris Brenna, Federica Foadelli, Michela Longo, and Luigi Piegari  
Volume 2015, Article ID 979321, 8 pages

**Hierarchical Control Strategy for the Cooperative Braking System of Electric Vehicle**, Jiankun Peng, Hongwen He, Wei Liu, and Hongqiang Guo  
Volume 2015, Article ID 584075, 11 pages

**A Novel Range-Extended Strategy for Fuel Cell/Battery Electric Vehicles**, Jenn-Jiang Hwang, Jia-Sheng Hu, and Chih-Hong Lin  
Volume 2015, Article ID 363094, 8 pages

**Conventional, Hybrid, or Electric Vehicles: Which Technology for an Urban Distribution Centre?**, Philippe Lebeau, Cedric De Cauwer, Joeri Van Mierlo, Cathy Macharis, Wouter Verbeke, and Thierry Coosemans  
Volume 2015, Article ID 302867, 11 pages

**Charging Guidance of Electric Taxis Based on Adaptive Particle Swarm Optimization**, Liyong Niu and Di Zhang  
Volume 2015, Article ID 354952, 9 pages

**A Traction Control Strategy with an Efficiency Model in a Distributed Driving Electric Vehicle**, Cheng Lin and Xingqun Cheng  
Volume 2014, Article ID 261085, 12 pages

**Optimal Control Strategy Design Based on Dynamic Programming for a Dual-Motor Coupling-Propulsion System**, Shuo Zhang, Chengning Zhang, Guangwei Han, and Qinghui Wang  
Volume 2014, Article ID 958239, 9 pages

## Editorial

# Modeling, Control, and Optimization Technologies in Electric Drive Vehicles

**Hongwen He,<sup>1,2</sup> Suleiman M. Sharkh,<sup>3</sup> Caiping Zhang,<sup>4</sup> Xuan Zhou,<sup>5</sup> and Rui Xiong<sup>1,2</sup>**

<sup>1</sup>National Engineering Laboratory for Electric Vehicles, School of Mechanical Engineering, Beijing Institute of Technology, Beijing 100081, China

<sup>2</sup>Collaborative Innovation Center of Electric Vehicles in Beijing, Beijing Institute of Technology, No. 5 South Zhongguancun Street, Haidian District, Beijing 100081, China

<sup>3</sup>Electro-Mechanical Engineering Research Group, Engineering Science, University of Southampton, Highfield, Southampton SO17 1BJ, UK

<sup>4</sup>School of Electrical Engineering, Beijing Jiaotong University, Beijing 100044, China

<sup>5</sup>Electrical and Computer Engineering Department, Kettering University, Flint, MI 48504, USA

Correspondence should be addressed to Hongwen He; hwhebit@bit.edu.cn

Received 27 April 2015; Accepted 27 April 2015

Copyright © 2015 Hongwen He et al. This is an open access article distributed under the Creative Commons Attribution License, which permits unrestricted use, distribution, and reproduction in any medium, provided the original work is properly cited.

To address the two urgent issues nowadays of protecting the environment and achieving energy sustainability, it is of strategic importance on a global scale to replace oil-dependent vehicles with electric drive vehicles (EDVs). Numerical simulation and optimization are essential to simulate the actual hardware and minimize the development procedure and cost. Accurate and efficient modeling, control, and optimization technologies have been the indispensable tools. EDVs have been continuously improved owing to the advancement of systematic control and power management, energy systems, batteries, and pack technologies, as well as economic and policy incentives, public awareness of energy sustainability/affordability, and environmental concerns. The primary goal of this special section is to provide timely solutions to technological and economic challenges in modeling, simulation, control, and optimization of EDVs. The accepted papers cover a range of different aspects of modeling, control, and optimization technologies for electric vehicles. A brief summary of them is given as follows.

Most of papers are used to investigate the control and power management for EDVs. C. Lin and X. Cheng investigated a traction control strategy with an efficiency model in a distributed driving electric vehicle. S. Zhang et al. studied the optimal control strategy for a dual-motor coupling propulsion electric bus. The dynamic programming is applied to find the optimal control strategy including upshift threshold,

downshift threshold, and power split ratio between the main motor and auxiliary motor. To improve the regenerative braking performance, J. Peng et al. provided a hierarchical control strategy for the cooperative braking system of an electric vehicle with separated driven axles. P. Lebeau et al. explored the possible integration of electric vehicles in urban logistics operations. A fleet size and mix vehicle routing problem with time windows for electric vehicles has been developed. In particular, an energy consumption model was integrated in order to consider variable range of electric vehicles. J.-J. Hwang et al. presented a novel charging strategy for fuel cell/battery electric vehicles. In comparison to the conventional switch control, a fuzzy control approach was employed to enhance the battery's state of charge (SOC).

In terms of the batteries and grouping technology, S. Barcellona et al. proposed a simple method to investigate the effect of the duty cycle on the batteries lifetime through tests performed on different cells for different kinds of cycle. In this way, a generic complex cycle could be seen as a composition of elemental cycles by means of Rainflow procedures. Consequently, the ageing due to any cycle could be estimated starting from the knowledge of simpler cycles from their research results. For the research field of energy systems and networks, L. Niu and D. Zhang analyzed the actual operational data of electric taxis in Shenzhen, China. An electric taxis charging guidance model was established and guides

the charging based on the positions of taxis and charging stations with adaptive mutation particle swarm optimization. The simulation results showed that electric taxis could be evenly distributed to the appropriate charging stations according to the charging pile numbers in charging stations after the charging guidance.

In summary, the included seven papers cover the topics of modeling, control, and optimization technologies in EDVs with the new research achievements; we hope and are sure that the readers of this special issue could find valuable references to their research on EDVs.

### **Acknowledgments**

We very much appreciate all the authors' contributions to the special issue and the reviewers' efforts to rigorously examine the submitted manuscripts.

*Hongwen He  
Suleiman M. Sharkh  
Caiping Zhang  
Xuan Zhou  
Rui Xiong*

## Research Article

# Analysis of Ageing Effect on Li-Polymer Batteries

**Simone Barcellona,<sup>1</sup> Morris Brenna,<sup>2</sup> Federica Foiadelli,<sup>2</sup>  
Michela Longo,<sup>2</sup> and Luigi Piegari<sup>1</sup>**

<sup>1</sup>*Department of Electronics, Information and Bioengineering, Politecnico di Milano, 20133 Milano, Italy*

<sup>2</sup>*Department of Energy, Politecnico di Milano, 20156 Milano, Italy*

Correspondence should be addressed to Federica Foiadelli; federica.foiadelli@polimi.it

Received 21 November 2014; Revised 26 January 2015; Accepted 25 February 2015

Academic Editor: Rui Xiong

Copyright © 2015 Simone Barcellona et al. This is an open access article distributed under the Creative Commons Attribution License, which permits unrestricted use, distribution, and reproduction in any medium, provided the original work is properly cited.

Lithium-ion batteries are a key technology for current and future energy storage in mobile and stationary application. In particular, they play an important role in the electrification of mobility and therefore the battery lifetime prediction is a fundamental aspect for successful market introduction. Numerous studies developed ageing models capable of predicting battery life span. Most of the previous works compared the effect of the ageing factors to a battery's cycle life. These cycles are identical, which is not the case for electric vehicles applications. Indeed, most of the available information is based on results from laboratory testing, under very controlled environments, and using ageing protocols, which may not correctly reflect the actual utilization. For this reason, it is important to link the effect of duty cycles with the ageing of the batteries. This paper proposes a simple method to investigate the effect of the duty cycle on the batteries lifetime through tests performed on different cells for different kinds of cycle. In this way, a generic complex cycle can be seen as a composition of elemental cycles by means of Rainflow procedures. Consequently, the ageing due to any cycle can be estimated starting from the knowledge of simpler cycles.

## 1. Introduction

Energy storage systems, usually batteries, are essential for electric drive vehicles, such as hybrid electric vehicles (HEVs), plug-in hybrid electric vehicles (PHEVs), and all-electric vehicles (EVs) [1]. However, the growing attention to energy aspects that leads to the introduction of renewable sources into a new concept of active electric grids makes storage systems one of the most important and critical research topics of the sector.

Many factors are affecting the operational characteristics, capacity, energy output, and performance of a battery. Different manufacturers have dissimilar approaches to address these issues by different chemical systems, additives, form factors, and dimensions, which will have significant effect to different performances and usages of the batteries [2]. In addition, many automakers have adopted Lithium-ion (Li-ion) batteries as the preferred electric drive vehicles (EDVs) energy storage option, capable of delivering the required energy and power density in a relatively small, lightweight package.

In fact, Li-ion batteries are a key technology for current and future energy storage, whether they are used for mobile or stationary application [3]. They are preferred over other battery technologies since they provide one of the best energy-to-weight ratios, have no memory effect, and have a slow self-discharge [4]. Recently, Li-ion batteries are applied to many sectors, as automotive, aerospace, or defense, due to their high energy density [5]. In particular, in the automotive sector the increasing demand for electric vehicles has forced consideration of other promising battery technologies, such as Li-ion batteries, to replace existing lead-acid batteries. However, this replacement is challenging due to the large power and energy demands placed on such batteries, while guaranteeing their safe operation. So the battery's capacity and performance are crucial for the abovementioned applications. Moreover, Li-ion battery cannot be overcharged and overdischarged because these conditions could damage it.

In this way, a battery management system (BMS) is essential for the system to get accurate knowledge of Li-ion battery's operation condition. In particular, a core function is to provide accurate estimates of state of charge (SOC) and state

of health (SOH) of batteries. Many methods, among which Coulomb counting [6], open circuit voltage monitoring [7], impedance spectroscopy [8], fuzzy logic, [9], neural network [10], and Kalman filter [11–13], were proposed in order to estimate the battery SOC and SOH. All these methods with advantages and disadvantages are summarized in [14].

The extensive use of batteries in hybrid electric vehicles (HEVs) today requires establishing an accurate model of battery ageing and life. Battery ageing can be dissociated into two parts: the calendar ageing and the cycle one [15]. The calendar ageing corresponds to the irreversible proportion of lost capacity during storage. In other terms, it is the degradation caused by the battery storage [16, 17]. On the contrary, cycle ageing is associated with the impact of battery utilization periods called cycles (charge or discharge). It happens when the battery is either in charge or in discharge. This is a direct consequence of the level, the utilization mode, the temperature conditions, and the current solicitations of the battery. As a consequence, during a battery's lifetime, its performance slowly deteriorates because of the degradation of its electrochemical constituents which in turn results in the deterioration of the HEV performance and fuel efficiency. These undesirable effects include the loss of rated capacity, faster temperature rise during operation, less charge acceptance, higher internal resistance, lower voltage, and more frequent self-discharge. The most drastic effect is the loss of rated capacity [18].

For these reasons, identifying ageing and degradation mechanisms in a battery is the main and most challenging goal. Such processes are complicated as many factors from environment or from utilization mode interact to generate different ageing effects.

To get insight into these performances degradation, research efforts were dedicated to model Li-ion ageing, namely, capacity loss or impedance increase, and quantify the impact of ageing factors [19, 20]. In spite of intensive investigations on various positive and negative electrode chemistries, these ageing phenomena are not yet well understood and not quantified, and the combined impacts of temperature (T), SOC, depth of discharge (DOD), and current intensity still remain difficult to quantify and manage. Although most of Li-ion ageing mechanisms have been experimentally identified and described in the literature, these phenomena are complex and can interact with each other, resulting in different evolution shapes for capacity loss and power fade [21]. Such aspects are important over the lifetime of the vehicle and have been extensively studied through long-term experiments on various battery technologies. However, most of the available information is based on results from laboratory testing, under very controlled environments, and using ageing protocols, which may not correctly reflect the actual vehicle utilization. Also the ageing data provided by the battery manufacturers result from standard ageing tests, in which the battery is discharged and charged thousands of times with identical current profiles (or cycles). Therefore, significant differences in ageing and battery life may exist when the batteries are utilized on a vehicle under specific operating conditions and usage patterns, leading to conservative vehicle designs where the battery is typically oversized

to guarantee performance and range near the end of life [22].

The problem of the effect of the duty cycle on batteries lifetime is not a trivial problem. In normal use, the batteries follow a power request that is never a standard discharge up to a fixed SOC. For this reason, it is very important to link the effect of duty cycles with the ageing of the batteries trying to make this complex problem as simple as possible.

In this paper, only the cycle ageing of Lithium-ion batteries is analyzed. A simple method to investigate on the effect of the duty cycle on the batteries lifetime, through tests performed on different cells, has been proposed. Through this method, it is possible to estimate the ageing of the batteries for different cycles starting from the knowledge of few parameters. A generic complex cycle can be seen as a composition of elemental cycles by means of Rainflow procedures [23]. In this way, the ageing due to any also complex cycle can be estimated starting from the knowledge of simpler cycles.

## 2. Experimental Test Procedure

The problem of evaluating the lifetime of batteries is a very hard task up to now not solved. In particular, for EVs, the information of the batteries SOH, together with that of SOC, could be very interesting.

As is well known, the life of batteries depends on many parameters: temperature, current, depth of discharge, voltage, humidity, and so on. Anyway, to take into account all these parameters is a very hard challenge. In this paper, the effect of the duty cycle on the batteries lifetime has been addressed.

The problem of the effect of the duty cycle on lifetime of batteries is a difficult problem. Indeed, the life of batteries is always given by manufacturers with reference to fixed cycles. They refer to discharge up to SOC values (usually 20% and 80% of the depth of discharge). In normal use, the batteries follow a power request that is never a standard discharge up to a fixed SOC. For this reason, it is very important to link the effect of duty cycles with the ageing of the batteries. In this paper, it would be shown that, in some conditions, it is possible to estimate the ageing of the batteries for different cycles starting from the knowledge of few parameters. In order to do it, the battery will be cycled with 2 *elemental* cycles and then with a cycle composed of the first two. Then, the results will be analyzed to understand if the ageing of the composed cycle can be derived from the ageing of the elemental ones. If this is true, any cycle can be decomposed in elemental cycles by means of Rainflow procedures [23] and the ageing for any cycle can be estimated.

In order to evaluate the SOH of the batteries under tests, it has been chosen to consider their capacity as the indicator of SOH. For this reason, during the ageing tests, the batteries are periodically full charged and full discharged for measuring their capacity. Another indicator of SOH could be the internal resistance. For the approach used by the authors, information about internal resistance is considered only as an instrument for a SOH evaluator but is not used for *measuring* the state of ageing. With the aim of verifying the effect of duty cycles on the ageing process of batteries, the tests have been made

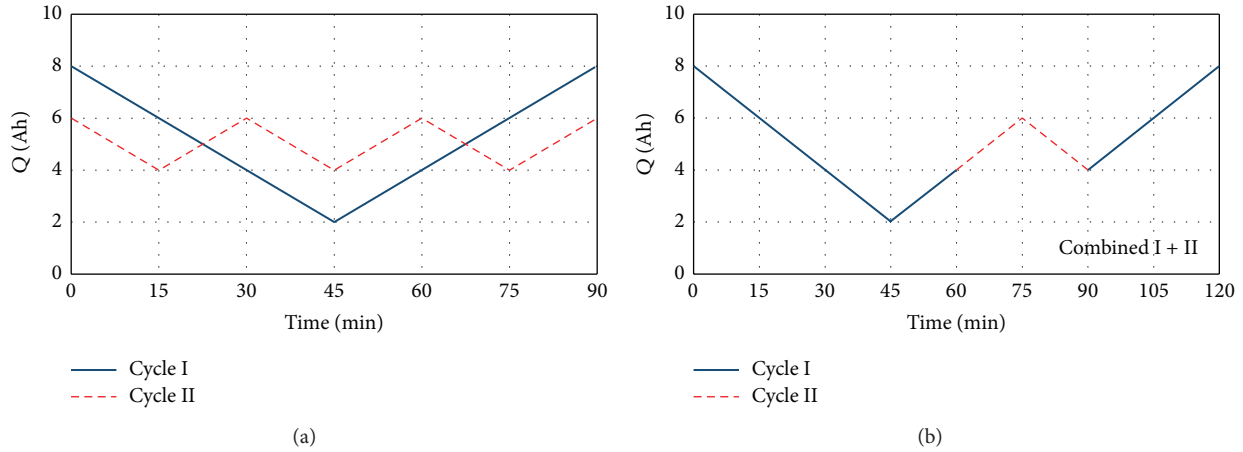


FIGURE 1: (a) Elemental test cycles and (b) combination of the two elemental cycles.

TABLE 1: Main data of the cells under test.

Item	Specifications	Remark
Rated capacity	10000 mAh	0.2 C-5 A discharge, 25° C
Rated voltage	3.7 V	Average voltage at 0.2 C-5 A discharge
Standard charge current	0.2 C-5 A	Working temperature: 0~40° C
Max charge current	1 C-5 A	Working temperature: 0~40° C
Charge cut-off voltage	4.2 V	CC/CV
Discharge current	Continuously, 10 C; max, 15 C	Working temperature: 0~60° C
Discharge cut-off voltage	2.75 V	
Cell voltage	3.7~3.9 V	When leaving factory
Impedance	≤12 mΩ	AC 1 kHz after 50% charge, 25° C
Weight	Approx. 228 g	
Storage temperature		
≤1 month	-10~45° C	
≤3 months	0~30° C	
≤6 months	20 ± 5° C	Best 20 ± 5° C for long-time storage
Storage humidity	65 ± 20% RH	

with noncritical conditions for all the other variables. For this reason, the cells have been cycled in the following conditions:

- (i) under ambient temperature and humidity (the temperature cell has been monitored);
- (ii) with a current lower than the rated current (C1) for avoiding ageing due to high currents;
- (iii) in a SOC region between 80% and 20% in order to avoid ageing occurring in the zones of high or low voltage.

The cell used for the test is a polymer Li-ion battery 8773160K manufactured by General Electronics Battery Co., Ltd. The main data of the cell are reported in Table 1.

The two elemental cycles are defined as follows:

- (1) starting from a SOC equal to 80%, discharge 6 Ah (60%) at 8 A, and charge 6 Ah at 8 A,
- (2) starting from a SOC equal to 60%, discharge 2 Ah (20%) at 8 A, and charge 2 Ah at 8 A,

- (3) the third cycle, composed using the first two, which is constituted by charge and discharge phases at 8 A following the profile reported in Figure 1(b).

Figure 1(a) shows the two elemental tests defined in the above (1) and (2), while in Figure 1(b) the combination of the two elemental cycles is reported.

The three cycles have been applied to three fresh cells and, every 15 cycles, a full charge and discharge cycle has been performed for measuring the capacity of the cell. The tests have been performed at the Department of Electronics, Information and Bioengineering of the Politecnico di Milano using a 100-A booster (VMP3B-100) connected to a potentiostat (SP-150), which were both from Biologic Science Instruments, controlled by a PC via USB with EC-LAB software. Figure 2 shows the experimental setup.

If the age effect of the third cycle can be obtained as a combination of the ageing effects of the first two cycles, it is possible to estimate the ageing of any cycle decomposing it in elemental cycles. The decomposition could be obtained,

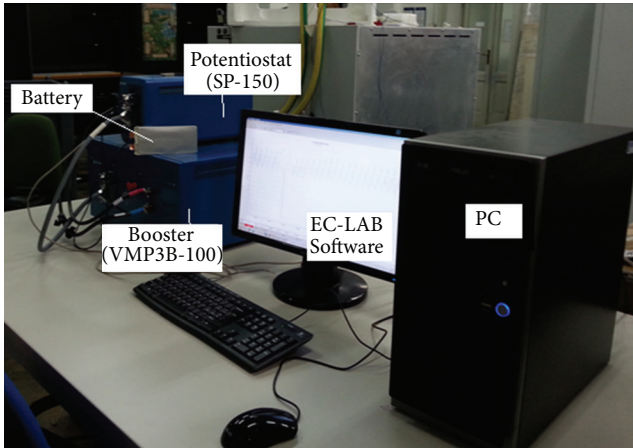


FIGURE 2: Experimental setup.

for example, by using Rainflow algorithms. The application of Rainflow techniques to batteries ageing is out of the scope of this paper in which only the possibility of estimating the ageing as a “sum” of ageing of elemental cycles will be addressed.

### 3. Experimental Results

As discussed in the previous section, the three cells have been tested with the cycles defined in Figure 1. At first, 300 cycles have been performed. Then, it has been verified that 300 cycles of kind 2 are too few for appreciating the ageing of batteries. Therefore, other 300 cycles, for a total of 600 cycles, have been performed on each cell. In the following, the three cells will be indicated with subscripts 1, 2, and 3 corresponding to the cycle to which they have been tested.

The three cells are, of course, different from one another. In order to compare their ageing, a preliminary measurement of their capacity has been performed and this value has been considered as reference value for evaluating the ageing. In particular, the initial measured capacity of the three cells is

$$\begin{aligned} C_1 &= 10.191 \text{ Ah}, \\ C_2 &= 10.290 \text{ Ah}, \\ C_3 &= 10.268 \text{ Ah}. \end{aligned} \quad (1)$$

The following capacity reductions will be calculated per unit using the bases reported in (1). In Figure 3, the capacity reductions (blue line) of the three cells during the 600 cycles are reported.

Looking at the capacities obtained with the two elemental cycles a significant increasing at cycle 300 can be noted. This behavior is due to the pause introduced after 300 cycles. Indeed, as discussed above, initially 300 cycles have been programmed. Then, in order to increase the ageing effect, other 300 cycles have been performed. During the pause, the recovery effect of the batteries implies an increasing in the capacity for some cycles. In the combined cycle this effect is not visible because this cycle, being the last performed, has been executed without the pause. So, the first points after the

pause should not be considered to analyze the ageing effect. In the behavior of the second cell, an increasing of the capacity after the first cycle can be observed. This could be due to effect of initial conditioning of the cell. For this reason, the initial capacity  $C_2$  is probably higher than the first value. In Figure 3 also the cells’ temperature is shown.

Looking at Figure 3, it is possible to see that the temperature variation (green line) is limited in the range 25–40°C. This variation is due to the fact that the first set of 300 test cycles was performed during the summer while the other set was made during the autumn. As a consequence, it is important to report the different tests at the same temperature in order to obtain the battery ageing not depending on the temperature itself. In order to do that, it is necessary to know the variation of battery capacity as a function of the temperature. The latter relation is obtainable making other tests through which the capacity of the battery is measured at different temperatures using the climatic chamber reported in Figure 4.

So the battery capacity was measured in a temperature range of 20–40°C with a temperature step of 2.5°C, testing a new battery of the same kind. Test results are reported in Figure 5 together with a linear interpolated function.

The battery capacity as a function of the temperature, expressed in Ah (Figure 5), is as follows:

$$C(T) = 0.003849T + 10.08, \quad (2)$$

where  $T$  is the temperature expressed in °C.

Figure 3 shows also the ageing of the three batteries reported at the same temperature of 20°C (red line) together with the ageing without the temperature correction (blue line). It is possible to note that the temperature effect is limited, about 1% of the battery capacity change with respect to a temperature variation of 20°C, as confirmed in [24–26].

Looking at the three behaviors of the battery ageing reported at the same temperature a linear decrease of the capacity with the square root of the number of cycles can be recognized. The interpolations, for the three curves, are reported in Figure 6 (green line) and the corresponding functions are the following:

$$\begin{aligned} C_1(n_1) &= 10.164 - 0.0134\sqrt{n_1}, \\ C_2(n_2) &= 10.302 - 0.0093\sqrt{n_2}, \\ C_3(n_3) &= 10.251 - 0.0239\sqrt{n_3}, \end{aligned} \quad (3)$$

where  $n$  is the cycle number and all the capacities are expressed in Ah.

It is worth to note that the ageing coefficient of the combined cycle is almost equal to the sum of the ageing coefficients of the two elemental cycles. Therefore, the ageing seems to be connected to the moved charge as stated for lead-acid batteries in [27] and, in particular, to the square root of the moved charge.

In order to understand if the effects of the two elemental cycles can be combined in the third cycle, (3) have to be expressed as function of the moved charge. Taking into

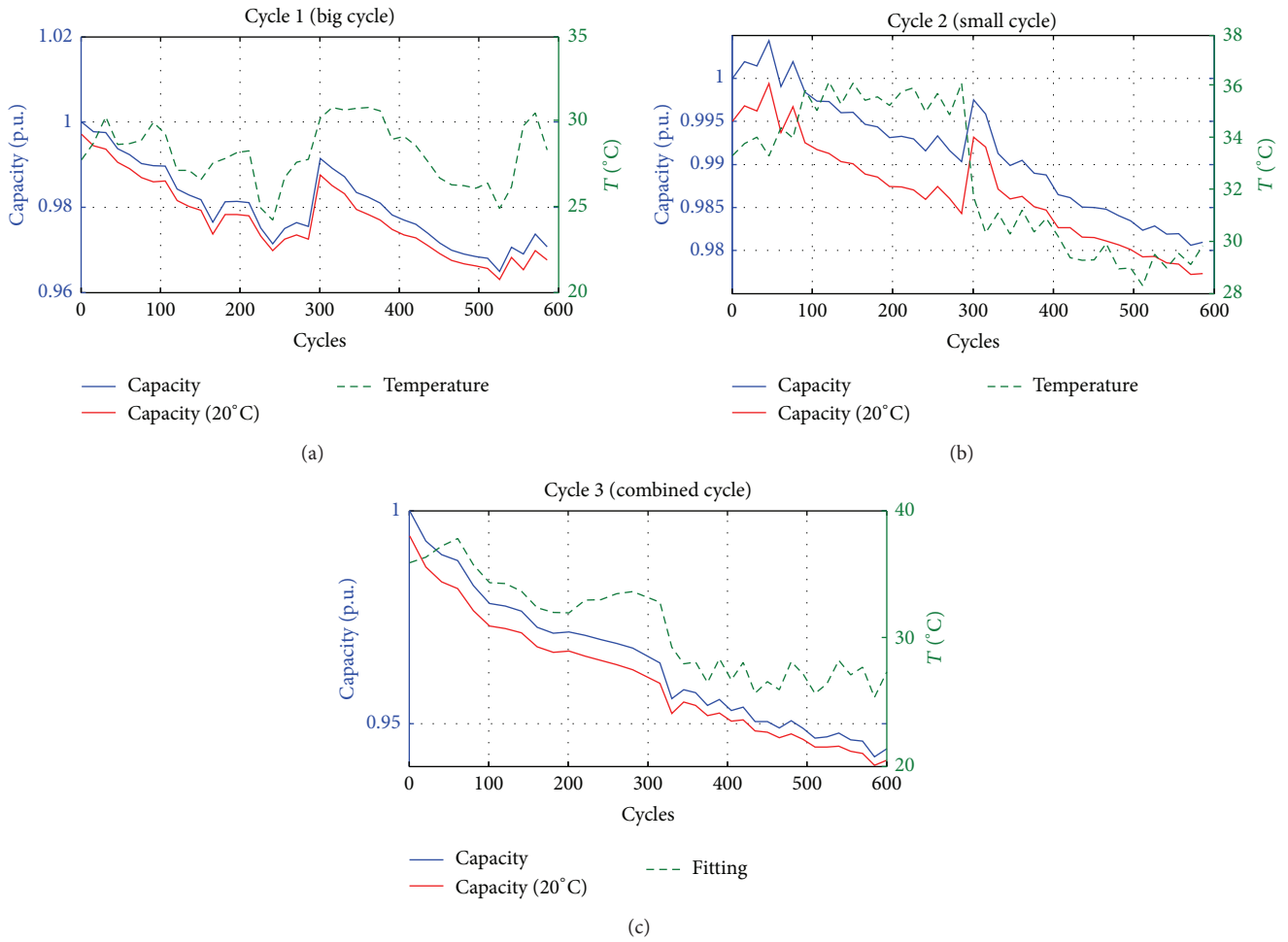


FIGURE 3: Ageing of the three cells as function of the cycles.



FIGURE 4: Climatic chamber.

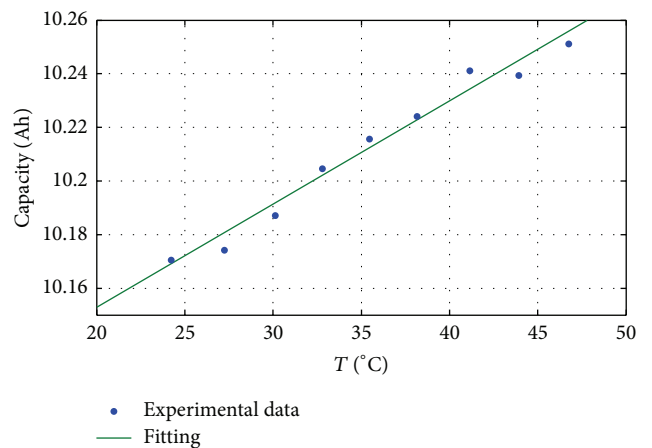


FIGURE 5: Battery capacity in function of the temperature.

account the moved charge of each cycle as reported in Figure 1, (3) can be rewritten as

$$\begin{aligned}
 C_1(q) &= 10.164 - 0.0035\sqrt{q} \text{ [Ah]}, \\
 C_2(q) &= 10.302 - 0.0037\sqrt{q} \text{ [Ah]}, \\
 C_3(q) &= 10.251 - 0.0056\sqrt{q} \text{ [Ah]},
 \end{aligned}
 \tag{4}$$

where  $q$  is the charge, in Ah, moved by each battery. From (4) it is possible to see that the ageing is quite similar for the three batteries if the square root of the moved charge is considered as ageing factor. The coefficients of the two

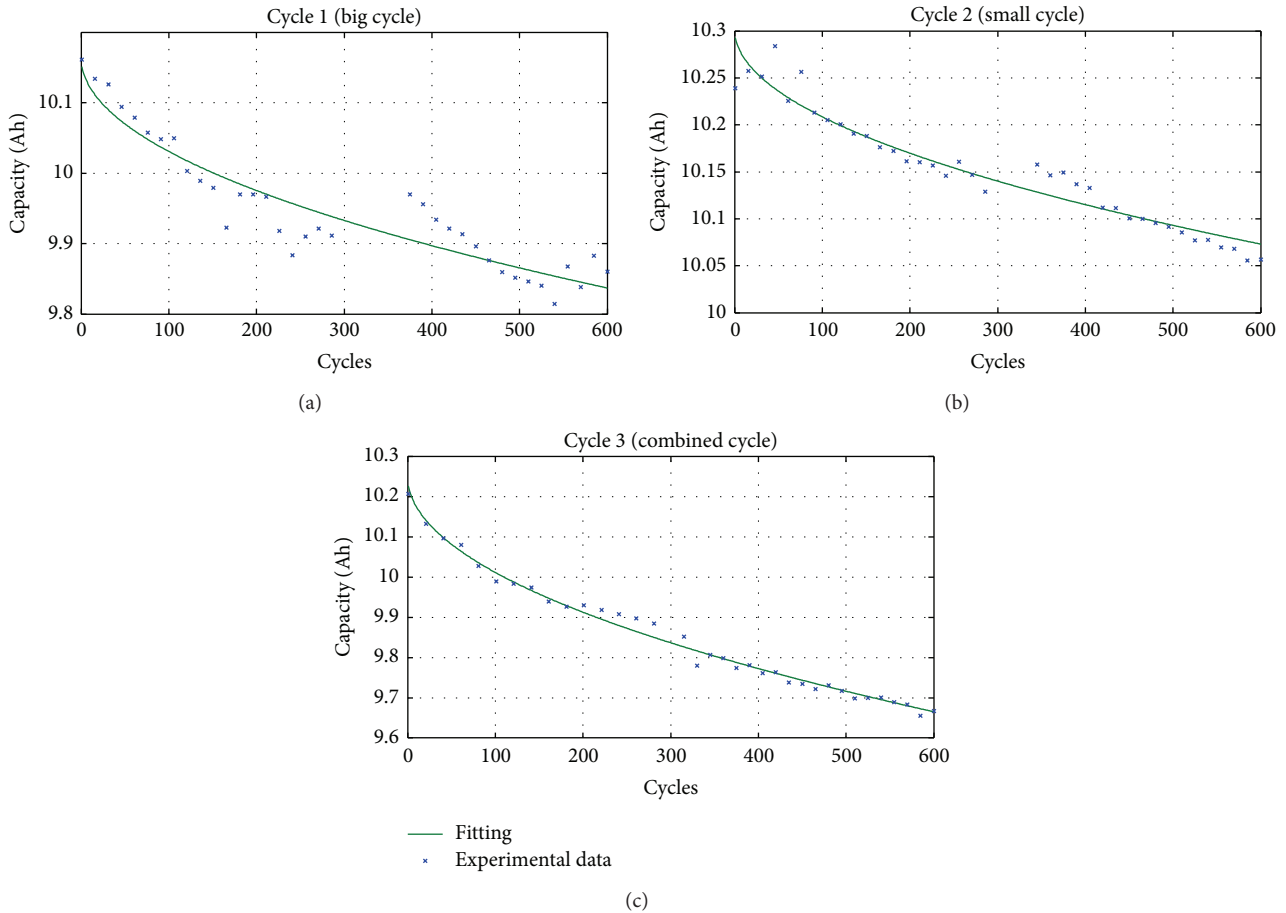


FIGURE 6: Interpolation of the ageing of the three cells.

elemental cycles show a lower ageing in comparison with the combined test. This could be due to the pause after 300 cycles that has been inserted for the two elemental cycles and not for the combined cycle. With reference to the reported tests, moreover, it has to be taken into account that the *moved charge* is influenced also by the charge *moved* during capacity measurements (every 15 cycles). The capacities of the three cells as function of the square root of the moved charge are reported in Figure 7. In order to compare the residual capacities of the three cells, they were normalized on their initial rated capacity, while the moved charge was normalized on the nominal charge of the battery (10 Ah).

From the analysis of Figure 7, it can be stated that the ageing of the three batteries, measured as the reduction of their capacity, can be expressed, with good approximation, as function only of the square root of the moved charge. The interpolating function reported in the figure is

$$C(q) = 1 - 0.0017\sqrt{q} \text{ [p.u.]} \tag{5}$$

Looking at Figure 7 it can be seen that the recovery effect causes an increasing in the shown capacity with respect to the other data. In particular, the black circles, referring to the big cycle, after the pause occurring at approximately 4000 Ah (400 × 10 Ah), are quite higher than the interpolating function.

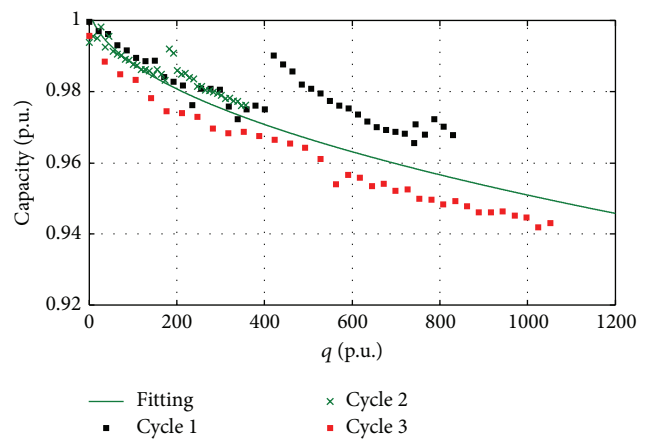


FIGURE 7: Ageing of the three batteries.

According to (5) the useful life of this kind of batteries could be predicted. Considering the end of life for the batteries when a reduction of the capacity of 20% is reached [28], from (5) a total charge of 160 kAh can be moved. Then, it is possible to state that the duty cycle does not practically affect the battery ageing.

It is worth to note that the life prediction does not take into account all the reactions that can occur when the voltage is close to the minimum or to the maximum but refers to the *best* use of the batteries in the *linear* region (i.e., where the voltage is a linear function of the SOC). Anyway, considering a cycle of 80% (i.e., 16 Ah, 8 for discharge and 8 for charge) the predicted life results are equal to 10000 cycles that is higher than the data given by manufacturers for this kind of battery. A change in degradation of the battery after a high number of cycles can be foreseeable. The prosecution of the test campaign will investigate this issue.

#### 4. Conclusions

Many of the modern appliances, from mobile phones to electric cars, employ Li-ion batteries as their source of energy, so their correct operations depend on the actual performances of the battery. Therefore, it is important to estimate the health and the life of the battery considering different applications. Various models have been proposed in scientific literature to estimate the ageing of the batteries. Some of them consider chemical models that need many and often unknown parameters. Often the equivalent circuit models are preferred because of the easiest way to obtain the values of the parameters.

Battery models are essential for any battery-powered system design that aims at extending the battery's expected life and in battery power management.

For this reason, identifying ageing and degradation mechanisms in a battery is the main and most challenging goal. Such processes are complicated as many factors from environment or from utilization mode interact to generate different ageing effects.

Most of the available information concerning the battery ageing is based on results from laboratory testing, under very controlled environments, and using ageing protocols, which may not correctly reflect the actual vehicle utilization. Also the ageing data provided by the battery manufacturers result from standard ageing tests, in which the battery is discharged and charged thousands of times with identical current profiles (or cycles).

The problem of the effect of the duty cycle on batteries lifetime is important to estimate in a correct way the ageing of batteries. In normal use, the batteries follow a power request that is never a standard discharge up to a fixed SOC. For this reason, it is very important to link the effect of duty cycles with the ageing of the batteries.

This paper proposes a novel and simple way, but at the same time efficient, to estimate the life of the battery taking into account the effect of the duty cycle starting from the knowledge of few parameters that can be determined from reproducible tests. In particular, a generic complex cycle can be seen as a composition of different elemental cycles. In this way, the ageing due to any also complex cycle can be estimated starting from the knowledge of simpler cycles.

To this purpose many experimental tests have been carried out on three Li-ion batteries stressed with different charge/discharge cycles in order to estimate their state of health and consequently the effects due to their ageing.

The results, obtained from the analysis of the collected data, show that the ageing of the Li-ion battery is correlated with the total electric charge that flows into the battery cells and in particular with the square root of the total moved charge. Then, it is possible to state that the duty cycle does not practically affect the battery ageing. It is worth to note that the life prediction does not take into account all the reactions that can occur when the voltage is close to the minimum or to the maximum but refers to the best use of the batteries in the linear region. In addition, a change in degradation of the battery after a high number of cycles can be foreseeable. Therefore, further tests are needed to investigate this issue.

#### Conflict of Interests

The authors declare that there is no conflict of interests regarding the publication of this paper.

#### References

- [1] V. Agarwal, K. Uthaichana, R. A. Decarlo, and L. H. Tsoukalas, "Development and validation of a battery model useful for discharging and charging power control and lifetime estimation," *IEEE Transactions on Energy Conversion*, vol. 25, no. 3, pp. 821–835, 2010.
- [2] K. Yiu, "Battery technologies for electric vehicles and other green industrial projects," in *Proceedings of the 4th International Conference on Power Electronics Systems and Applications (PESA '11)*, pp. 1–2, June 2011.
- [3] J. Schmalstieg, S. Kabitz, M. Ecker, and D. U. Sauer, "From accelerated aging tests to a lifetime prediction model: analyzing lithium-ion batteries," in *Proceedings of the World Electric Vehicle Symposium and Exhibition (EVS '13)*, pp. 1–12, Barcelona, Spain, November 2013.
- [4] N. A. Chaturvedi, R. Klein, J. Christensen, J. Ahmed, and A. Kojic, "Modeling, estimation, and control challenges for lithium-ion batteries," in *Proceedings of the American Control Conference (ACC '10)*, pp. 1997–2002, July 2010.
- [5] M. Armand and J.-M. Tarascon, "Building better batteries," *Nature*, vol. 451, no. 7179, pp. 652–657, 2008.
- [6] S. Piller, M. Perrin, and A. Jossen, "Methods for state-of-charge determination and their applications," *Journal of Power Sources*, vol. 96, no. 1, pp. 113–120, 2001.
- [7] L. Lu, X. Han, J. Li, J. Hua, and M. Ouyang, "A review on the key issues for lithium-ion battery management in electric vehicles," *Journal of Power Sources*, vol. 226, pp. 272–288, 2013.
- [8] A. Cuadras and O. Kanoun, "SoC Li-ion battery monitoring with impedance spectroscopy," in *Proceedings of the 6th International Multi-Conference on Systems, Signals and Devices (SSD '09)*, vol. , no. pp. 1–5, March 2009.
- [9] P. Singh, C. Fennie Jr., and D. Reisner, "Fuzzy logic modelling of state-of-charge and available capacity of nickel/metal hydride batteries," *Journal of Power Sources*, vol. 136, no. 1, pp. 322–333, 2004.
- [10] T. Parthiban, R. Ravi, and N. Kalaiselvi, "Exploration of artificial neural network [ANN] to predict the electrochemical characteristics of lithium-ion cells," *Electrochimica Acta*, vol. 53, no. 4, pp. 1877–1882, 2007.
- [11] A. Vasebi, M. Partovibakhsh, and S. M. T. Bathaee, "A novel combined battery model for state-of-charge estimation in lead-acid batteries based on extended Kalman filter for hybrid

- electric vehicle applications,” *Journal of Power Sources*, vol. 174, no. 1, pp. 30–40, 2007.
- [12] G. L. Plett, “Extended Kalman filtering for battery management systems of LiPB-based HEV battery packs—part 2. Modeling and identification,” *Journal of Power Sources*, vol. 134, no. 2, pp. 262–276, 2004.
- [13] J. Lee, O. Nam, and B. H. Cho, “Li-ion battery SOC estimation method based on the reduced order extended Kalman filtering,” *Journal of Power Sources*, vol. 174, no. 1, pp. 9–15, 2007.
- [14] Y. Zou, X. Hu, H. Ma, and S. E. Li, “Combined State of Charge and State of Health estimation over lithium-ion battery cell cycle lifespan for electric vehicles,” *Journal of Power Sources*, vol. 273, pp. 793–803, 2015.
- [15] E. Meissner and G. Richter, “The challenge to the automotive battery industry: the battery has to become an increasingly integrated component within the vehicle electric power system,” *Journal of Power Sources*, vol. 144, no. 2, pp. 438–460, 2005.
- [16] O. Erdinc, B. Vural, and M. Uzunoglu, “A dynamic lithium-ion battery model considering the effects of temperature and capacity fading,” in *Proceedings of the International Conference on Clean Electrical Power (ICCEP '09)*, pp. 383–386, June 2009.
- [17] G. Sarre, P. Blanchard, and M. Broussely, “Aging of lithium-ion batteries,” *Journal of Power Sources*, vol. 127, no. 1-2, pp. 65–71, 2004.
- [18] L. Serrao, Z. Chehab, Y. Guezennec, and G. Rizzoni, “An aging model of Ni-MH batteries for hybrid electric vehicles,” in *Proceedings of the IEEE Vehicle Power and Propulsion Conference (VPPC '05)*, pp. 78–85, September 2005.
- [19] R. Spotnitz, “Simulation of capacity fade in lithium-ion batteries,” *Journal of Power Sources*, vol. 113, no. 1, pp. 72–80, 2003.
- [20] M. Safari, M. Morcrette, A. Teyssot, and C. Delacourt, “Multi-modal physics-based aging model for life prediction of Li-Ion batteries,” *Journal of the Electrochemical Society*, vol. 156, no. 3, pp. A145–A153, 2009.
- [21] E. Prada, D. Di Domenico, Y. Creff, J. Bernard, V. Sauvant-Moynot, and F. Huet, “Physics-based modelling of LiFePO<sub>4</sub>-graphite Li-ion batteries for power and capacity fade predictions: application to calendar aging of PHEV and EV,” in *Proceedings of the IEEE Vehicle Power and Propulsion Conference (VPPC '12)*, pp. 301–308, October 2012.
- [22] A. di Filippi, S. Stockar, S. Onori, M. Canova, and Y. Guezennec, “Model-based life estimation of Li-ion batteries in PHEVs using large scale vehicle simulations: an introductory study,” in *Proceedings of the IEEE Vehicle Power and Propulsion Conference (VPPC '10)*, pp. 1–6, September 2010.
- [23] M. Musallam and C. M. Johnson, “An efficient implementation of the rainflow counting algorithm for life consumption estimation,” *IEEE Transactions on Reliability*, vol. 61, no. 4, pp. 978–986, 2012.
- [24] F. Lenga, C. M. Tana, M. Pecht, and J. Zhanga, “The effect of temperature on the electrochemistry in Lithium-ion batteries,” in *Proceedings of the International Symposium on Next-Generation Electronics (ISNE '14)*, pp. 1–4, Kwei-Shan, Taiwan, May 2014.
- [25] Y. Ye, Y. Shi, N. Cai, J. Lee, and X. He, “Electro-thermal modeling and experimental validation for lithium ion battery,” *Journal of Power Sources*, vol. 199, pp. 227–238, 2012.
- [26] A. N. Jansen, J. A. Clevenger, A. M. Baebler, and J. T. Vaughey, “Variable temperature performance of intermetallic lithium-ion battery anode materials,” *Journal of Alloys and Compounds*, vol. 509, no. 13, pp. 4457–4461, 2011.
- [27] “A study on batteries,” <http://www.verlab.dcc.ufmg.br/projetos/roomba/batteries>.
- [28] C. Sinkaram, V. S. Asirvadam, and N. B. Mohd Nor, “Capacity study of lithium ion battery for hybrid electrical vehicle (HEV) a simulation approach,” in *Proceedings of the 3rd IEEE International Conference on Signal and Image Processing Applications (ICSIPA '13)*, pp. 112–116, October 2013.

## Research Article

# Hierarchical Control Strategy for the Cooperative Braking System of Electric Vehicle

Jiankun Peng,<sup>1</sup> Hongwen He,<sup>1</sup> Wei Liu,<sup>1</sup> and Hongqiang Guo<sup>2</sup>

<sup>1</sup>National Engineering Laboratory for Electric Vehicles, Beijing Institute of Technology, Beijing 100081, China

<sup>2</sup>School of Mechanical and Automotive Engineering, Liaocheng University, Liaocheng Shandong 252000, China

Correspondence should be addressed to Jiankun Peng; pengjk87@gmail.com

Received 21 July 2014; Revised 21 September 2014; Accepted 26 September 2014

Academic Editor: Xuan Zhou

Copyright © 2015 Jiankun Peng et al. This is an open access article distributed under the Creative Commons Attribution License, which permits unrestricted use, distribution, and reproduction in any medium, provided the original work is properly cited.

This paper provides a hierarchical control strategy for cooperative braking system of an electric vehicle with separated driven axles. Two layers are defined: the top layer is used to optimize the braking stability based on two sliding mode control strategies, namely, the interaxle control mode and signal-axle control strategies; the interaxle control strategy generates the ideal braking force distribution in general braking condition, and the single-axle control strategy can ensure braking safety in emergency braking condition; the bottom layer is used to maximize the regenerative braking energy recovery efficiency with a reallocated braking torque strategy; the reallocated braking torque strategy can recovery braking energy as much as possible in the premise of meeting battery charging power. The simulation results show that the proposed hierarchical control strategy is reasonable and can adapt to different typical road surfaces and load cases; the vehicle braking stability and safety can be guaranteed; furthermore, the regenerative braking energy recovery efficiency can be improved.

## 1. Introduction

Cooperative braking is one of the core technologies in electric vehicles [1]. Two advantages can be provided by a good cooperative braking system. First, improved fuel economy can be achieved as a result of energy recuperation when braking [2]. Then, good braking stability can be obtained by a reliable braking force control strategy [3]. Many investigations have been reported for cooperative braking system. General braking condition and emergency braking condition are mainly studied [3–5].

For general braking condition, the peak road adhesion coefficient is high and the wheels will not be locked; the braking strategy focuses on the braking force distribution between front-rear wheels to keep a better braking stability and improve the regenerative braking energy recovery efficiency. For instance, considering the maximum regenerative braking capacity, the road adhesion condition and the braking requirement [4] made an optimal braking control chart for braking force distribution, which can be conveniently applied to engineering. Reference [5] designed a braking force distribution strategy in which the front wheel friction braking

force would be adjusted and the rear wheel braking force is only dependent on the braking pedal travel. Nevertheless, for the control strategies of [4, 5], some key parameters should be precisely estimated, which is not easy work. Reference [6] provided a braking force distribution strategy based on the ideal braking force distribution curve (I curve), by which the optimum braking stability was obtained. However, the ideal braking force curve will change as the variation of the loaded condition changes the mass center of the vehicle. The vehicle may fall into braking instability state if the braking strategy could not adapt to the variation of the ideal braking force curve.

For emergency braking cases, the objective is to avoid the vehicle being locked and improve the regenerative braking energy recovery efficiency meanwhile. The main control strategies can be classified into two types. One is based on the logic-threshold control and the other is based on sliding mode control. Reference [7] has proposed an optimized logic-threshold control strategy to improve the cooperative braking performance. References [8–12] provided fuzzy control strategies to improve the vehicle stability. References [3, 13–16] have made some sliding mode control strategies to

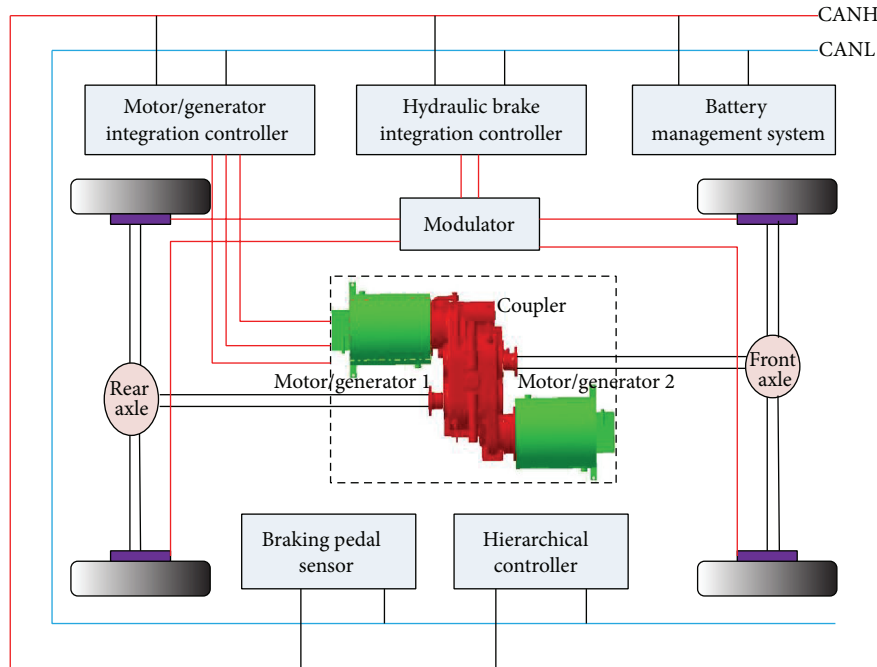


FIGURE 1: The cooperative braking system structure.

optimize the regenerative braking stability. Reference [17] has verified that combination of ABS and regenerative braking system can improve braking stability. All of the control strategies have been verified through simulation or road testing and made great efforts to the engineering application. For all the control strategies of the emergency braking condition, a reliable and good robustness control strategy which can adapt to various emergency braking cases is the key technology [18].

In this paper, a hierarchical control strategy which can meet the requirements of the general and emergency braking conditions is proposed. The hierarchical control strategy is designed to have top and bottom layers. The optimum braking stability is the main objective in the top layer. Considering the variation of the loaded condition, an interaxle sliding mode strategy is proposed, based on which the ideal braking force distribution can be realized. Furthermore, to avoid the braking instability in emergency braking condition, a single-axle sliding mode strategy is also designed to meet various emergency cases. The switching condition between the control strategies is based on the threshold value of slip rate. In the bottom layer, the required braking torque will be reallocated between generators and hydraulic brakes; the optimum regenerative braking energy recovery efficiency is the main objective in this layer.

## 2. The Cooperative Braking System Structure

As shown in Figure 1, a coupler together with two motors/generators is equipped in the electric vehicle, based on which four-wheel drive mode can be realized. Additionally, in order to realize the real-time braking torque distribution of the hydraulic brakes, a modulator is also applied in the

cooperative braking system. Particularly worth mentioning is that the communication of the vehicle is through the CAN bus. During regenerative braking process, motors are used as generators. Generator 1 provides regenerative braking torque to the front axle; generator 2 provides regenerative braking torque to the rear axle. Besides, the slip rates can be real-time calculated by the hierarchical controller due to the fact that wheels speed can be calculated by the motors/generators' speed and the vehicle speed can be obtained by GPS instrument.

## 3. Hierarchical Control Strategy

*3.1. The Flow Chart of the Control Strategy.* Generally, the motors' speed can be obtained real-time from the CAN bus, which is one of the advantages of the electric vehicles. The wheels speed can be calculated from the motors' speed without wheel speed sensors. It is worth noting that because of the vehicle speed which can be directly obtained by the GPS instrument, the slip rates of front and rear wheels can be easily calculated.

Figure 2 shows the hierarchical control strategy. Optimizing the braking stability is the main object of the top layer and maximizing the regenerative braking energy recovery efficiency is the main object of the bottom layer. Based on the switching condition, the top layer can choose a suitable control strategy to maintain the braking stability. If the interaxle sliding mode control strategy is worked, a braking severity signal is also needed, which can be got from the analysis of the driver's braking intention. On the contrary, if the single-axle sliding mode control strategy worked, the top layer can adjust the braking force distribution without the braking severity signal. After adjusting, the distributed

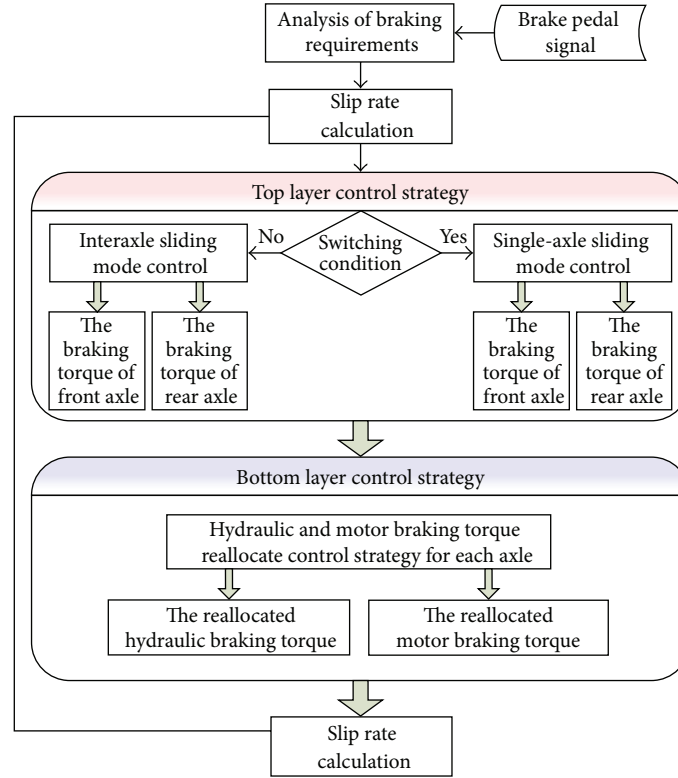


FIGURE 2: The hierarchical control strategy.

braking torque will be delivered to the low layer. Under the control strategy of the bottom layer, the maximum generating torque which is subjected to the generators and battery will be calculated firstly, and, then, a reallocation control strategy will be worked to reallocate the distributed braking torque to the generators and hydraulic brakes.

### 3.2. The Top Layer

**3.2.1. The Switching Condition.** The top layer needs to judge the switch condition real-timely to realize the strategy switch. Generally, if the slip rate is lower than  $S_{opt}$  which is the slip rate corresponding to the peak adhesion coefficient (about 15%~20%), the vehicle will stay in the general braking condition. On the contrary, the vehicle will be in emergency braking condition. The maximum adhesion coefficient is usually around  $S_{opt}$ , which is also the optimum value for the cooperative braking system. However, for the single-axle sliding mode control, the target value is also  $S_{opt}$ , which will lead the slip rate to be fluctuating around this value; namely, if the switch condition is  $S_{opt}$ , both the control strategies will be switched repeatedly. So the switching condition is defined as

$$S_f > S_{shift} \parallel S_r > S_{shift}, \tag{1}$$

$$S_{shift} = S_{opt} - \delta_s,$$

where  $\delta_s$  is the relaxation factor and  $S_{shift}$  is the control mode shift threshold. In this paper, take  $S_{opt} = 20\%$  and  $\delta_s = 5\%$ .

**3.2.2. The Interaxle Sliding Mode Strategy.** According to the top layer in Figure 2, if both of the slip rates are lower than  $S_{shift}$ , the general braking condition will be recognized. As stated in the introduction, the ideal braking force distribution strategy is good for the braking stability. However, it is also a risky control strategy with the variation of the loaded condition. So, how to realize a dynamic ideal braking force distribution strategy in the general braking condition is one of the key technologies in the top layer.

In this paper, an interaxle sliding mode strategy is proposed to equate the front and rear wheels' slip rates by adjusting the distribution of the braking force between front and rear wheels, which can guarantee the braking stability at general braking condition. The excellent adaptability to the parameter fluctuation is a highlighted advantage for the sliding mode control. Additionally, the slip rates of the wheels can always be real-timely calculated under any load case by the top layer. So the ideal braking force distribution strategy will always be obtained and will be unaffected by the varied loaded condition.

According to the definition of the slip rate, the interaxle sliding mode strategy can be realized by the identical wheel speed control. The switching function can be described as

$$s = \omega_f - \omega_r + c \int_0^t (\omega_f - \omega_r) dt, \tag{2}$$

where  $c$  is the weighting parameter which denotes the slope value of the sliding curve and  $\omega_f$  and  $\omega_r$  are the rotation speed of the front and rear wheels, respectively.

Taking a derivative of (2), we can give

$$\dot{s} = \dot{\omega}_f - \dot{\omega}_r + c(\omega_f - \omega_r), \quad (3)$$

where  $\dot{s}$  is the reaching law.

According to the dynamic equation of the vehicle, we have

$$\begin{aligned} \dot{\omega}_f &= \frac{F_f r - T_f}{I}, \\ \dot{\omega}_r &= \frac{F_r r - T_r}{I}, \end{aligned} \quad (4)$$

where  $T_f$  and  $T_r$  denote the braking torque of the rear wheels, respectively,  $F_f$  and  $F_r$  denote the longitudinal braking tire force of the front and rear wheels, respectively,  $I$  is the moment of inertia of the wheels, and  $r$  is the radius of the wheels.

Substituting (4) into (3), we can get

$$T_r - T_f = \dot{s}I + F_r r - F_f r - cI(\omega_f - \omega_r). \quad (5)$$

Generally, the reaching law is vital to accelerate the reaching process. In this paper, we adapt to the exponential reaching law:

$$\dot{s} = -\varepsilon \operatorname{sgn} s - ks, \quad \varepsilon > 0, k > 0 \quad (6)$$

$$s(t) = \begin{cases} \frac{\varepsilon}{k} + \left(s_0 - \frac{\varepsilon}{k}\right)e^{-kt}, & s > 0 \\ -\frac{\varepsilon}{k} + \left(s_0 + \frac{\varepsilon}{k}\right)e^{-kt}, & s < 0, \end{cases} \quad (7)$$

where  $s_0$  is the initial value of  $s$ .

Substituting (6) into (5), another equation can be realized as

$$T_r - T_f = (-\varepsilon \operatorname{sgn} s - ks)I + F_r r - F_f r - cI(\omega_f - \omega_r). \quad (8)$$

During the general braking, the total required braking torque of the vehicle can be obtained by the braking severity, which is the result of the analysis of the driver's braking intention:

$$T_{\text{require}} = \delta mgzr, \quad (9)$$

where  $T_{\text{require}}$  is the total required braking torque of the vehicle,  $m$  is the vehicle mass,  $g$  is the acceleration of gravity, and  $z$  is the braking severity.  $\delta$  is the rotary mass coefficient. In addition,  $T_{\text{require}}$  is also equal to the sum of  $T_f$  and  $T_r$ :

$$T_{\text{require}} = T_f + T_r. \quad (10)$$

Combining (5) with (10), we can get

$$\begin{aligned} T_r &= \frac{(-\varepsilon \operatorname{sgn} s - ks)I + F_r r - F_f r + mgzr - cI(\omega_f - \omega_r)}{2}, \\ T_f &= \frac{mgzr + (\varepsilon \operatorname{sgn} s + ks)I - F_r r + F_f r + cI(\omega_f - \omega_r)}{2}. \end{aligned} \quad (11)$$

**3.2.3. The Single-Axle Sliding Mode Control Strategy.** As shown in the switching condition, if any of the slip rates is bigger than  $S_{\text{shift}}$ , the single-axle sliding mode control will be activated. According to the braking theory, if the slip rates of the tires fluctuated around  $S_{\text{opt}}$ , the longitudinal adhesion ratio and the lateral adhesion ratio will be maximized simultaneously. So both the braking distance and the braking stability will be improved. In addition, similar to the interaxle sliding mode strategy, a good control strategy which can adapt to different road surfaces and load cases also takes a vital important role.

The switching function in this control strategy of the front wheel can be expressed as

$$s_{fi} = S_f - S_{\text{opt}}, \quad (12)$$

where  $S_f$  is the slip rate of the front wheels, which is calculated as follows:

$$S_f = \frac{v - \omega_f r}{v}. \quad (13)$$

Taking a derivative of (12) and (13), we get

$$\dot{s}_{fi} = \dot{S}_f = \frac{-\dot{\omega}_f r + (1 - S_f)\dot{v}}{v}. \quad (14)$$

Combining (14) with (4), we get

$$T_f = \frac{Iv\dot{s}_{fi}}{r} + F_f r - \frac{I(1 - S_f)\dot{v}}{r}. \quad (15)$$

The reaching law of this sliding mode is the same as the interaxle sliding mode:

$$\dot{s}_{fi} = -\varepsilon \operatorname{sgn} s - ks, \quad \varepsilon > 0, k > 0, \quad (16)$$

where  $s(t)$  has the same description as (7).

Substituting (16) into (15),  $T_f$  can be rewritten as

$$T_f = \frac{Iv(-\varepsilon \operatorname{sgn} s - ks)}{r} + F_f r - \frac{I(1 - S_f)\dot{v}}{r}. \quad (17)$$

Similarly,  $T_r$  can be deduced as the same method of  $T_f$ :

$$T_r = \frac{Iv(-\varepsilon \operatorname{sgn} s - ks)}{r} + F_r r - \frac{I(1 - S_r)\dot{v}}{r}. \quad (18)$$

**3.3. The Bottom Layer.** How to reallocate the distributed braking torques to the generators and hydraulic brakes to maximize the regenerative braking energy recovery is the core technology in this paper. Two technologies should be studied: the first one is the real-time calculation of the maximum charging torque and the other is the reallocation strategy between generators and hydraulic brakes.

**3.3.1. The Maximum Charging Torque Calculation.** Generally, the maximum charging torque is affected by two factors. One is the maximum output generating torque of the generators, which is constrained by the given generator speed and the

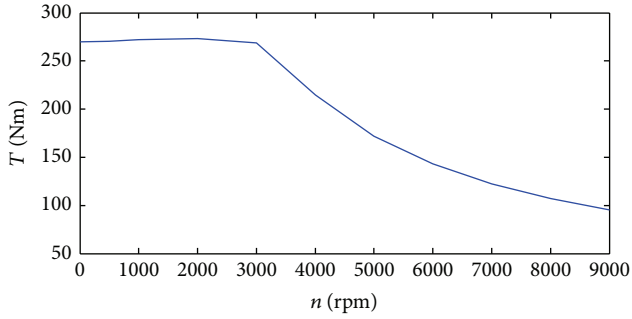


FIGURE 3: The generating torque versus speed curve.

torque characteristics of motor. The other is the maximum input charging torque of the battery, which is restricted by the current state of charge (SoC).

The minimum of the two factors gives the maximum charging torque:

$$T_{\text{charging}} = \min \{ T_{\text{generating}}, T_{\text{recharging}} \}, \quad (19)$$

where  $T_{\text{charging}}$  is the maximum charging torque,  $T_{\text{generating}}$  is the maximum output generating torque of the generators, and  $T_{\text{recharging}}$  is the maximum input charging torque of the battery.

$T_{\text{generating}}$  can be obtained as follows:

$$\begin{aligned} T_{\text{generating}} &= T_{\text{generating}1} + T_{\text{generating}2} \\ T_{\text{generating}1} &= f_{T1}(n_1) \\ T_{\text{generating}2} &= f_{T2}(n_2), \end{aligned} \quad (20)$$

where  $n_1, n_2$  denote the speeds of the generators 1 and 2, respectively,  $T_{\text{generating}1}, T_{\text{generating}2}$  denote the maximum generating torque of generators 1 and 2, respectively, and  $f_{T1}(n_1), f_{T2}(n_2)$  denote the maximum generating torque which can be obtained by Figure 5 through interpolation method.

Additionally, if the generator speed is lower than 500 rpm, the generating efficiency and the control precision will be limited; in this paper, we define that if  $n < 500$  rpm, then make  $T_{\text{generating}} = 0$  (Figure 3).

$T_{\text{recharging}}$  can be calculated as follows.

Firstly, according to the current SoC, the charging power can be expressed as follows:

$$P_{\text{recharging}} = \begin{cases} P_{\text{recharging\_max}} & \text{SoC} \leq 0.3 \\ \frac{0.8 - \text{SoC}}{0.5} P_{\text{recharging\_max}} & 0.3 < \text{SoC} < 0.8 \\ 0 & \text{SoC} \geq 0.8, \end{cases} \quad (21)$$

where  $P_{\text{recharging\_max}}$  is the maximum charging power of the battery and  $P_{\text{recharging}}$  is the recharging power.

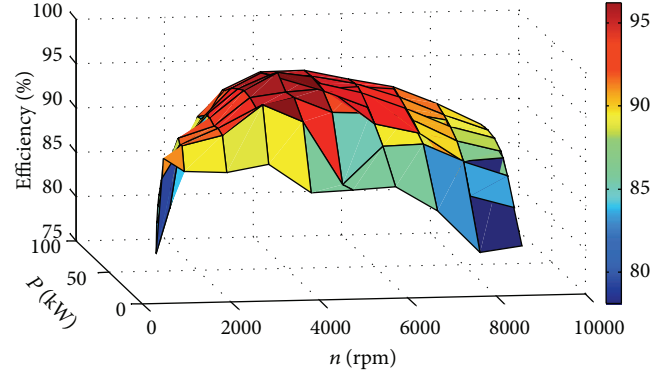


FIGURE 4: The efficiency map of the generators.

Then we can get

$$T_{\text{recharging}} = \frac{9550 P_{\text{recharging}}}{n \eta(n, P_{\text{recharging}})}, \quad (22)$$

where  $\eta(n, P_{\text{recharging}})$  is the efficiency of the generator, which is subjected to the speed  $n$  and the recharging power  $P_{\text{recharging}}$ , as shown in Figure 4.

3.3.2. *The Reallocation Strategy.* The basic principle for the bottom layer is to fulfill the maximum charging torque, for the sake of improving the regenerative braking energy recovery efficiency. It can be described as Figure 5 shows.

With respect to the front axle

if  $T_{\text{charging}}/2$  is bigger than  $T_f$ , then make  $T_{\text{generating}1} = T_f$  and  $T_{hf} = 0$ . If  $T_{\text{charging}}/2$  is lower than or equal to  $T_f$ , then make  $T_{\text{generating}1} = T_{\text{charging}}/2, T_{hf} = T_f - T_{\text{generator}1}$ .

With respect to the rear axle

if  $T_{\text{charging}}/2$  is bigger than  $T_r$ , then make  $T_{\text{generating}2} = T_r$  and  $T_{hr} = 0$ . If  $T_{\text{charging}}/2$  is lower than or equal to  $T_r$ , then make  $T_{\text{generating}2} = T_{\text{charging}}/2, T_{hr} = T_r - T_{\text{generator}2}$ ,

where  $T_{\text{generator}1}$  and  $T_{\text{generator}2}$  denote the reallocated charging torques of generator 1 and generator 2, respectively, and  $T_{hf}$  and  $T_{hr}$  denote the reallocated braking torques of the front and rear hydraulic brakes, respectively.

## 4. Simulation Results and Discussion

Based on the MATLAB/Simulink software, a simulation model of the vehicle is set up. The initial vehicle speed is defined as 64.8 km/h, and the initial SoC is 0.5. Moreover, two load cases are provided to verify the strategy adaptability to parameter changes, which are shown in Table 1.

4.1. *General Braking Condition.* Generally speaking, the braking severity under a dry payment is mainly lower than 0.35, which will take up 95% proportion [18]. In this braking condition, the road surface is defined as dry payment and the

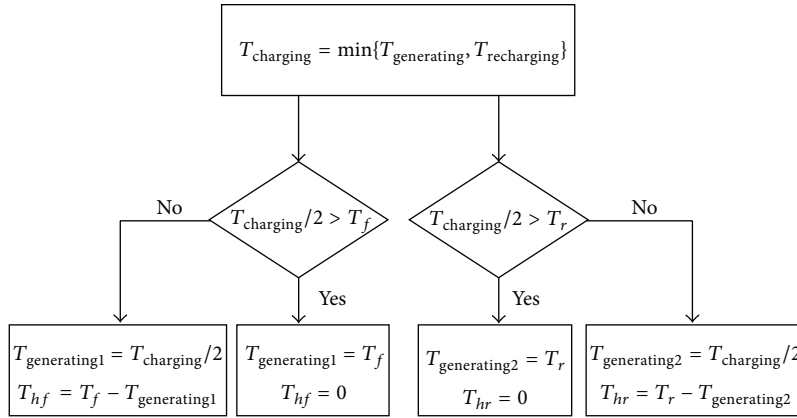


FIGURE 5: The reallocation strategy.

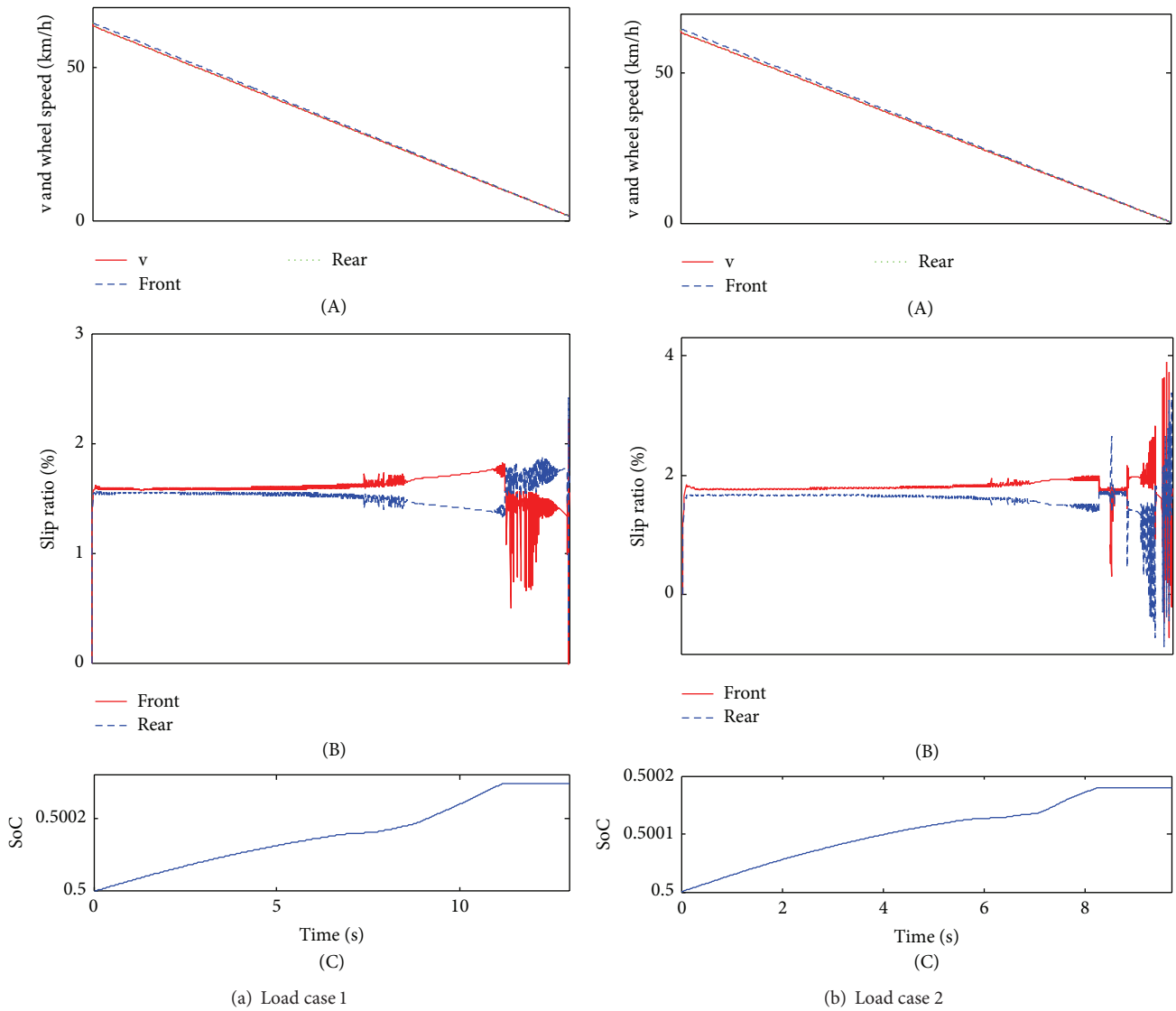


FIGURE 6: The simulation results of braking case 1.

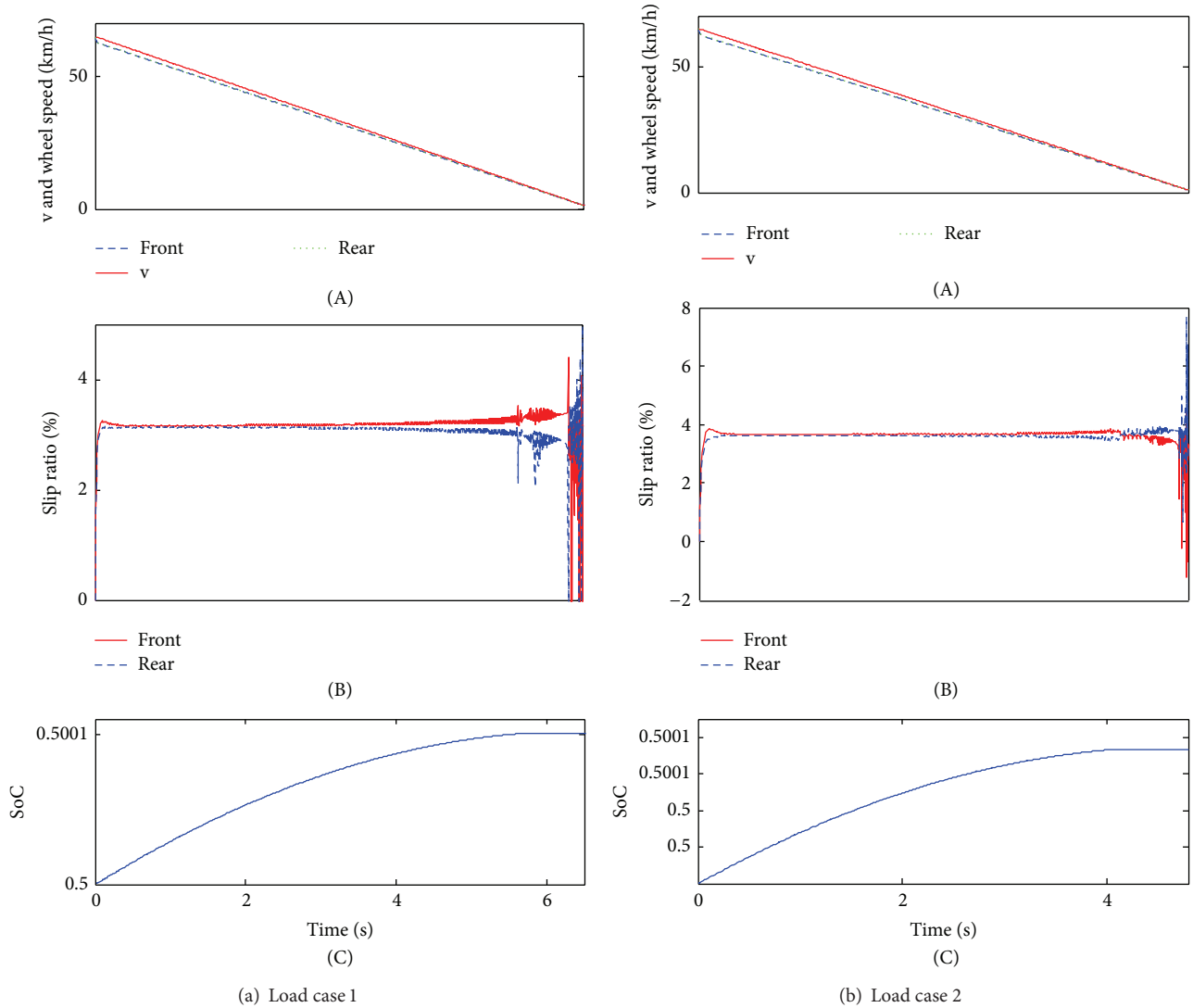


FIGURE 7: The simulation results of braking case 2.

TABLE 1: The load cases.

	Mass (kg)	The front wheel base (m)	The rear wheel base (m)	Centroid height (m)
Load case 1	5000	1.479	1.071	0.603
Load case 2	3550	1.483	0.996	0.569

peak adhesion coefficient is set as 0.8. To verify the interaxle sliding mode strategy, two braking cases are carried out, both of which are the mainly braking cases.

- (1) The braking severity is 0.15, which is defined as braking case 1.
- (2) The braking severity is 0.3, which is defined as braking case 2.

As shown in Figure 6(a), the times taken for stopping the vehicle are approximately 13 s for load case 1 and 9.7 s

for load case 2. Additionally, since the braking severity is relatively small, the wheel speeds can follow the vehicle speed well, which is the contribution of the interaxle sliding control strategy. At the same time, the slip rates between front and rear wheels of the two load cases are extremely close before the braking vehicle speed of 25 km/h (Figure 6(b)). It means that the vehicle can maintain the ideal braking force distribution mode under the control of the interaxle sliding control strategy. Subsequently, from the vehicle speed of about 25 km/h, the slip rates begin to be inconsistent; however, the inconsistency is small, and the most important is that the slip rate of the front wheel is bigger than the rear wheel, which can ensure the braking safety if the vehicle may be locked inevitably (the adhesion ratio of the front wheel is bigger than the rear wheel). At the end of the braking, the slip rates will be fluctuated remarkably, and the interaxle sliding mode control effectiveness is not obvious. The last and one of the most important performances is that SoC are increased to around 0.50021 for load case 1 and 0.50017 for load case 2. What is worth mentioning is that the bigger the vehicle mass

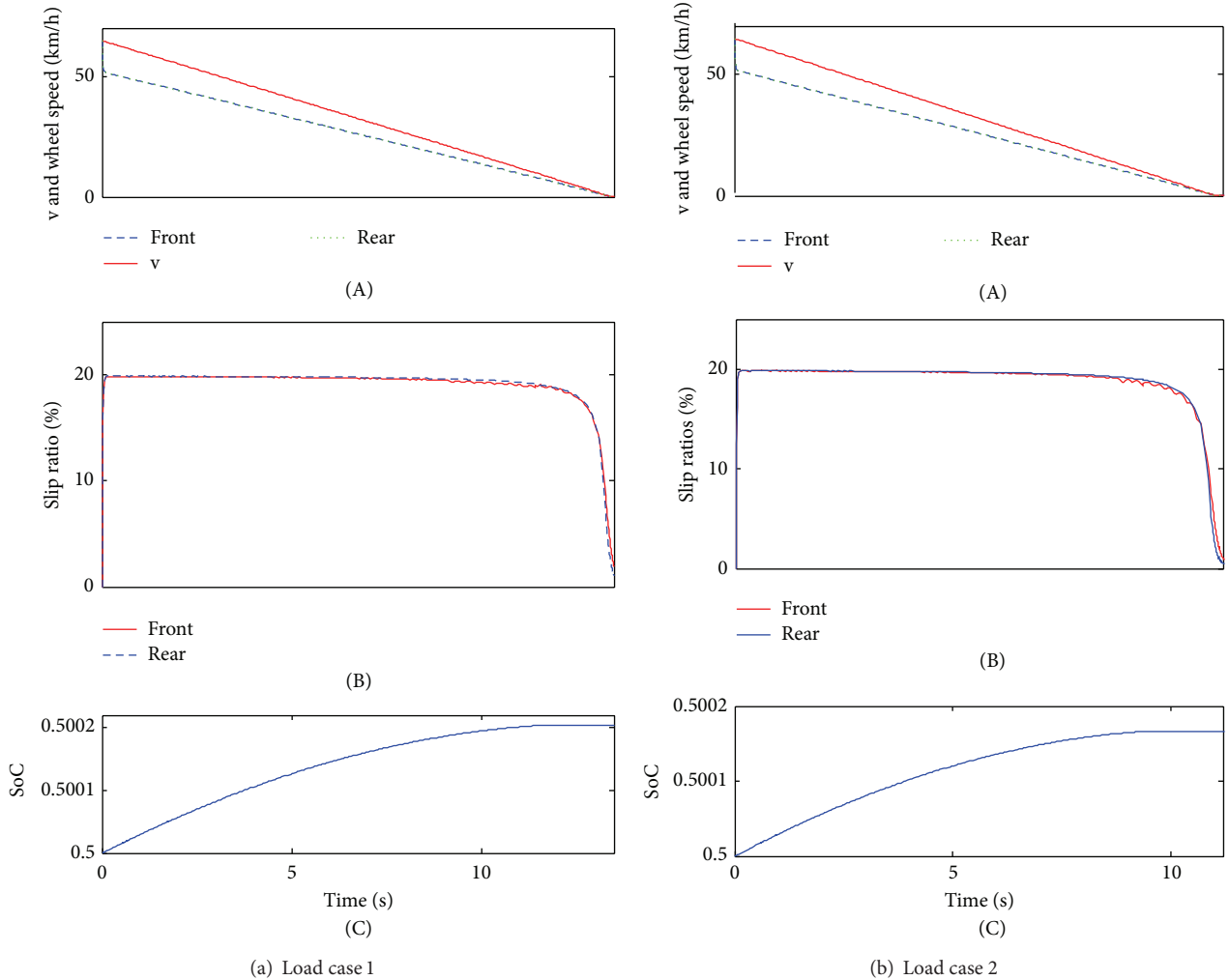


FIGURE 8: The simulation results of low and uniform load surface.

is, the higher SoC will be. In addition, after the braking vehicle speed of 12.5 km/h, SoC will keep a constant value as a result of the bottom layer's control strategy which defined that if  $n < 500$  rpm, make  $T_{\text{generating}} = 0$ .

The simulation results in Figure 7(a) show that the braking time is around 6.6 s for load case 1 and 4.8 s for load case 2. Both of the wheel speeds excellently follow the vehicle speed. Comparing to the slip rates between braking case 1 and braking case 2, the braking case 2 has a better control effectiveness. For load case 1, before the braking vehicle speed of 10 km/h, the slip rates are extremely close; for load case 2, only at the end of the braking deceleration do the slip rates have a little fluctuation. As a whole, the interaxle sliding mode strategy takes good control effectiveness in this braking case. With respect to SoC, obviously, they will increase for both load cases: for load case 1, the SoC will increase to around 0.50008 and, for load case 2, the SoC will increase to around 0.500071. Comparing to the braking case 1, the increasing rate will be relatively small, which indicates that the higher the braking severity is, the lower SoC will be. The same as braking case 1, SoC will also keep a constant value after the braking vehicle speed of 12.5 km/h.

Given the above analysis, the interaxle sliding mode control strategy has a good adaption for different braking cases and load cases. At mainly braking cases, the braking force distribution between the front and rear wheels can reach the ideal distribution; at the same time, the regenerative braking energy recovery efficiency can be further improved.

**4.2. Emergency Braking Condition.** The single-axle sliding mode control strategy aims at keeping the slip rates at about 20%, by which the vehicle can keep great longitudinal force and lateral force simultaneously, thereby improving the braking stability performance. Particularly in the emergency braking condition, a good control strategy can avoid the wheels being locked before stopping. In addition, to verify the adaptability to different road surfaces, two road surfaces are also provided in Table 2. The road surfaces are represented by the peak adhesion coefficient at each wheel.

Figure 8(a) shows that the vehicle stops around 13.5 s for load case 1 and 11.3 s for load case 2 and both load cases will not be locked on the low and uniform road surface. During braking deceleration, the slip rates will be adapted to about 20%, which is the target value of the single-axle sliding mode

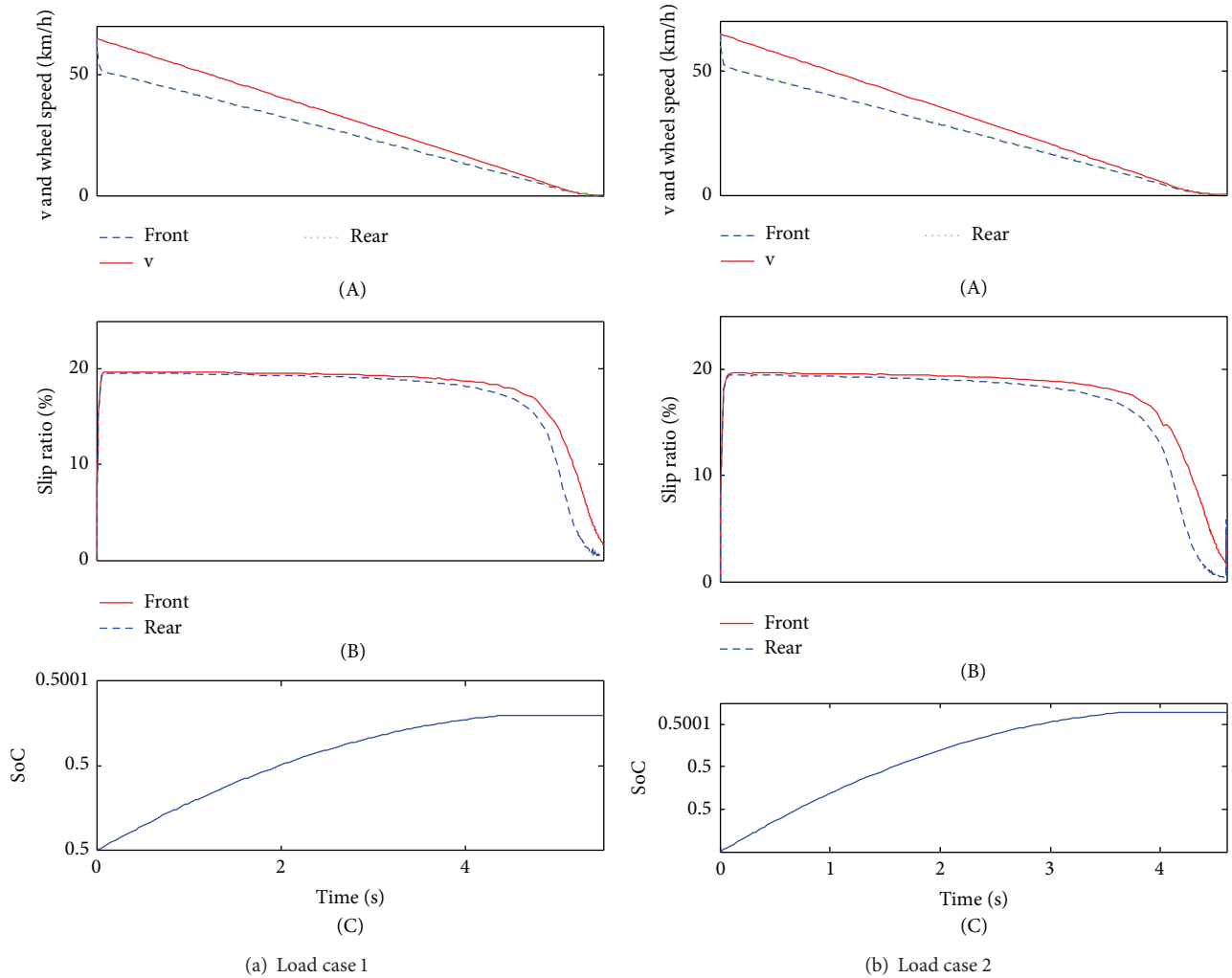


FIGURE 9: The simulation results of joint surface.

TABLE 2: The road surfaces.

Typical road surface	Adhesion coefficients	
	The front wheel	The rear wheel
Low and uniform	0.2	0.2
Joint	0.2	0.8

control strategy. As a result, the vehicle can get the maximum lateral braking force and keep a better braking stability. At the end of braking, the slip rate will slow down sharply, due to the low braking vehicle speed (Figure 8(b)). With regard to SoC, load case 1 has increased to approximately 0.500203; load case 2 has increased to around 0.500166. Comparing to the simulation results of the load cases, the single-axle sliding mode control strategy has preferable adaptability to different load cases.

As shown in Figure 9(a), both load cases will not be locked under the joint road surface. For load case 1, the braking time is about 5.4 s; for load case 2, the braking time is around 4.6 s. The slip rate control effectiveness is also very

preferable for both of the load cases; at the end of braking, due to the low braking vehicle, the single-axle sliding mode control is not obvious (Figure 9(b)). Additionally, SoC will be increased to 0.5008 for load case 1 and 0.500066 for load case 2 (Figure 8(c)). Similarly, the adaptability is also very good for different load cases.

In view of the above analysis, the hierarchical control strategy can adapt to different road surfaces and different load cases. As a result, the vehicle can keep a preferable braking stability during emergency braking condition and improve the regenerative braking energy recovery efficiency.

#### 4.3. Simulation Results When Passing the Complex Surfaces.

As shown in Figure 10(a), the vehicle was designed to pass the pavement from high adhesion surface to the low adhesion surface. The peak adhesion coefficient of the higher side was 0.8, and the lower side was 0.2. On this condition, the vehicle will pass three kinds of typical road surfaces in turn, which are uniform and high adhesion surface, joint adhesion surface, and uniform and low adhesion surface, respectively.

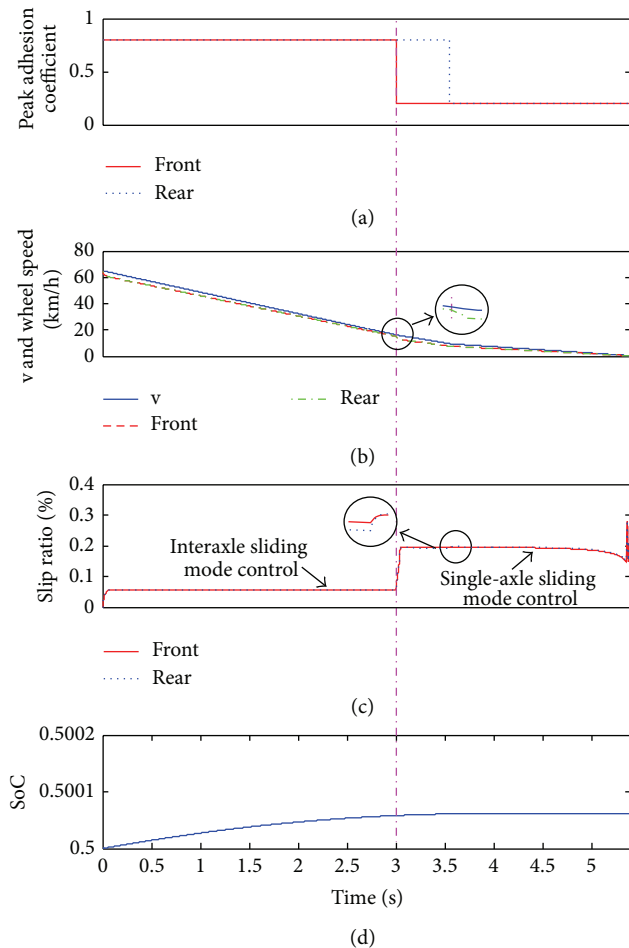


FIGURE 10: The simulation results when passing the complex surface.

The braking severity was defined as 0.3, and load case 1 was used.

From the braking time of 0 to 3 s, the vehicle was braking on the uniform and high adhesion surface; the general braking condition was selected. As a result, the slip rate control was based on the interaxle sliding mode control strategy, and the slip rates between front and rear wheels were extremely close (Figure 10(c)); correspondingly, the wheel speeds will perfectly follow the vehicle speed (Figure 10(b)). In addition, SoC was increasing constantly with the braking process. Subsequently, the peak adhesion coefficient of the front axle declined rapidly to 0.2, and the rear axle was still on the high adhesion side. The slip rate of the front wheel will be increased sharply; once the slip rate meets the switching condition, the top layer will switch to the single-axle sliding mode control strategy; then, the control strategy will strive to keep the slip rates of the front and rear wheels around 20%. It is worth noting that the wheel speeds will decrease suddenly at the switching point, and shortly after that the wheel speed will preferably follow the vehicle speed again. Besides, SoC was always increasing during this braking time until the speed of the generator was less than 500 rpm.

## 5. Conclusions

A hierarchical control strategy, including the interaxle sliding mode control strategy for the general braking condition, the single-axle sliding mode control strategy for the emergency braking condition, and the maximum charging torque strategy for the maximum regenerative braking energy recovery efficiency were studied in this paper.

The simulation results under the general braking condition show that the interaxle sliding mode control strategy could adapt to different load cases and keep the slip rates between front and rear almost consistence. The bottom layer could improve the regenerative braking energy recovery efficiency.

Aiming at the emergency braking condition, two typical road surfaces were also proposed and verified through the single-axle sliding mode control strategy. The simulation results indicate the slip rates were preferably controlled to about 20% for different emergency braking cases and different load cases. Moreover, the regenerative braking energy recovery efficiency was also improved.

A simulation was also carried out to verify the vehicle braking from one road surface to another, which proves that the hierarchical control strategy has a strong adaptability to different types of surfaces.

The hardware in the loop experiment for hierarchical control strategy and the vehicle road test will be considered in our next step work.

## Conflict of Interests

The authors declare that there is no conflict of interests regarding the publication of this paper.

## Acknowledgments

This work was supported by the National High Technology Research and Development Program of China (2012AA111603 and 2013BAG05B00), in part, the Program for New Century Excellent Talents in University (NCET-11-0785), and Beijing Institute of Technology Postgraduate Students Innovation Foundation in part.

## References

- [1] J. Kim, S. Ko, G. Lee, H. Yeo, P. Kim, and H. Kim, "Development of co-operative control algorithm for parallel HEV with electric booster brake during regenerative braking," in *Proceedings of the 7th IEEE Vehicle Power and Propulsion Conference (VPPC '11)*, pp. 1-5, Chicago, Ill, USA, September 2011.
- [2] S. A. Oleksowicz, K. J. Burnham, A. Southgate et al., "Regenerative braking strategies, vehicle safety and stability control systems: critical use-case proposals," *Vehicle System Dynamics*, vol. 51, no. 5, pp. 684-699, 2013.
- [3] T. K. Bera, K. Bhattacharya, and A. K. Samantaray, "Bond graph model-based evaluation of a sliding mode controller for a combined regenerative and antilock braking system," *Proceedings of the Institution of Mechanical Engineers I: Journal of Systems and Control Engineering*, vol. 225, no. 7, pp. 918-934, 2011.

- [4] W.-C. Lin, C.-L. Lin, P.-M. Hsu, and M.-T. Wu, "Realization of anti-lock braking strategy for electric scooters," *IEEE Transactions on Industrial Electronics*, vol. 61, no. 6, pp. 2826–2833, 2014.
- [5] C. Jo and H. Kim, "Performance analysis of electro-mechanical brake system for a hybrid electric vehicle using HILS," in *Proceedings of the 23th International Electric Vehicle Symposium and Exhibition (EVS '07)*, pp. 979–988, Anaheim, Calif, USA, December 2007.
- [6] J. Zhang, C. Lv, J. Gou, and D. Kong, "Cooperative control of regenerative braking and hydraulic braking of an electrified passenger car," *Proceedings of the Institution of Mechanical Engineers Part D: Journal of Automobile Engineering*, vol. 226, no. 10, pp. 1289–1302, 2012.
- [7] J. Zhang, D. Kong, L. Chen, and X. Chen, "Optimization of control strategy for regenerative braking of an electrified bus equipped with an anti-lock braking system," *Proceedings of the Institution of Mechanical Engineers, Part D: Journal of Automobile Engineering*, vol. 226, no. 4, pp. 494–506, 2012.
- [8] Z. Zhang, G. Xu, W. Li, and L. Zheng, "The application of fuzzy logic in regenerative braking of EV," in *Proceedings of the 2nd International Conference on Intelligent Human-Machine Systems and Cybernetics (IHMSC '10)*, pp. 124–128, Nanjing, China, August 2010.
- [9] L. Chu, L. Yao, J.-K. Yin, L.-B. Chao, and W. Wei, "Study on the braking force allocation dynamic control strategy based on the fuzzy control logic," in *Proceedings of the IEEE 18th International Conference on Industrial Engineering and Engineering Management (IE and EM '11)*, pp. 635–639, September 2011.
- [10] A. Ahmed and S. Cui, "Control and analysis of regenerative power distribution on electrical variable transmission using fuzzy logic on HEV system," in *Proceedings of the International Conference on Electrical Machines and Systems (ICEMS '11)*, pp. 1–6, August 2011.
- [11] C.-L. Zhang, Y.-J. Zhang, M.-D. Yan, and G.-P. Wang, "Fuzzy control modeling and simulation of regenerative braking system for pure electric vehicle with dual-source energy storage system," *Journal of System Simulation*, vol. 2, no. 4, 2011.
- [12] W. Liu, H. He, and J. Peng, "Driving control research for longitudinal dynamics of electric vehicles with independently driven front and rear wheels," *Mathematical Problems in Engineering*, vol. 2013, Article ID 408965, 17 pages, 2013.
- [13] J. Cao, E. Shiju, X. Zhu, H. Jiang, and B. Cao, "Simulation research on neural network sliding mode control of energy-regenerative braking of electric vehicle," *Applied Mechanics and Materials*, vol. 37-38, pp. 1187–1190, 2010.
- [14] A. Fazeli, M. Zeinali, and A. Khajepour, "Application of adaptive sliding mode control for regenerative braking torque control," *IEEE/ASME Transactions on Mechatronics*, vol. 17, no. 4, pp. 745–755, 2012.
- [15] G. Zhao, M. Wei, Y. Li et al., "The study on the regenerative anti-lock braking system of electric vehicle based on sliding mode control," *Modern Manufacturing Engineering*, pp. 1–10, 2012.
- [16] H. He, J. Peng, R. Xiong, and H. Fan, "An acceleration slip regulation strategy for four-wheel drive electric vehicles based on sliding mode control," *Energies*, vol. 7, no. 6, pp. 3748–3763, 2014.
- [17] J. Peng, H. He, and N. Feng, "Simulation research on an electric vehicle chassis system based on a collaborative control system," *Energies*, vol. 6, no. 1, pp. 312–328, 2013.
- [18] M. Mitschke and H. Wallentowitz, *Vehicle Dynamics*, Tsinghua University Press, Beijing, China, 4th edition, 2009.

## Research Article

# A Novel Range-Extended Strategy for Fuel Cell/Battery Electric Vehicles

Jenn-Jiang Hwang,<sup>1</sup> Jia-Sheng Hu,<sup>1</sup> and Chih-Hong Lin<sup>2</sup>

<sup>1</sup>Department of Greenery, National University of Tainan, Tainan 700, Taiwan

<sup>2</sup>Department of Mechanical Engineering, National Cheng Kung University, Tainan 701, Taiwan

Correspondence should be addressed to Jia-Sheng Hu; [jogson@gmail.com](mailto:jogson@gmail.com)

Received 15 September 2014; Revised 5 December 2014; Accepted 7 December 2014

Academic Editor: Rui Xiong

Copyright © 2015 Jenn-Jiang Hwang et al. This is an open access article distributed under the Creative Commons Attribution License, which permits unrestricted use, distribution, and reproduction in any medium, provided the original work is properly cited.

The range-extended electric vehicle is proposed to improve the range anxiety drivers have of electric vehicles. Conventionally, a gasoline/diesel generator increases the range of an electric vehicle. Due to the zero-CO<sub>2</sub> emission stipulations, utilizing fuel cells as generators raises concerns in society. This paper presents a novel charging strategy for fuel cell/battery electric vehicles. In comparison to the conventional switch control, a fuzzy control approach is employed to enhance the battery's state of charge (SOC). This approach improves the quick loss problem of the system's SOC and thus can achieve an extended driving range. Smooth steering experience and range extension are the main indexes for development of fuzzy rules, which are mainly based on the energy management in the urban driving model. Evaluation of the entire control system is performed by simulation, which demonstrates its effectiveness and feasibility.

## 1. Introduction

In order to reduce our dependence on petrochemical resources and decrease the deterioration of the earth's environment, the United Nations (UN) passed the "Kyoto Protocol" in December of 1997. Basically, the Kyoto Protocol progressively restricts the emissions of carbon dioxide (CO<sub>2</sub>) in every industrialized country. Consequently, this protocol has resulted in a massive impact on vehicle engineering. The result is a new challenge to the design of revolutionary vehicles for the future. Thus, the proposal of novel, low-pollution, and pollution-free vehicles has increased including concepts such as hybrid, ethanol, hydrogen fuel cell, and electric-power motor cars. In these next-generation automobiles, the fully electric motor vehicles have pollution-free benefits, which drive further research and development [1–3]. Compared to their conventional gasoline counterparts, these electric cars can achieve quieter and pollution-free operation. Electric cars are driven by electrical motors and are powered by batteries. Therefore, the prospects of the electric automobile industry are brightening. However, with respect to the driving experience, the electric vehicle has the following drawbacks.

- (a) The battery charging requires ample time—several hours for common home chargers.
- (b) Currently, the maximum range of a battery-powered car is less than its gasoline engine counterpart, which thus creates range anxiety.

In order to endow the electric vehicle with a similar driving experience as the gasoline engine car, the range-extended electric vehicle (REEV) [4, 5] is proposed. The range-extended electric vehicle is presented to mitigate the range anxiety of electric vehicles. Conventionally, the electric vehicle is range-extended by a gasoline/diesel generator. The generator charges the battery during times of rest. This idea can assist the battery's state of charge (SOC) in maintaining a higher level. Consequently, as the generator is in operation, the vehicle is not in a pollution-free mode, which, to the dismay of many, is therefore not compliant with the aim of zero-CO<sub>2</sub> emission. The fuel cell range-extended electric vehicle (FC-REEV) is presented in response to these concerns. Unlike the hybrid vehicles, the fuel cell only acts as the energy supplier to the battery. The entire powertrain is in a cascade formation. Of course, if the fuel cell power is sufficient, a fuel cell generator can supply electricity to

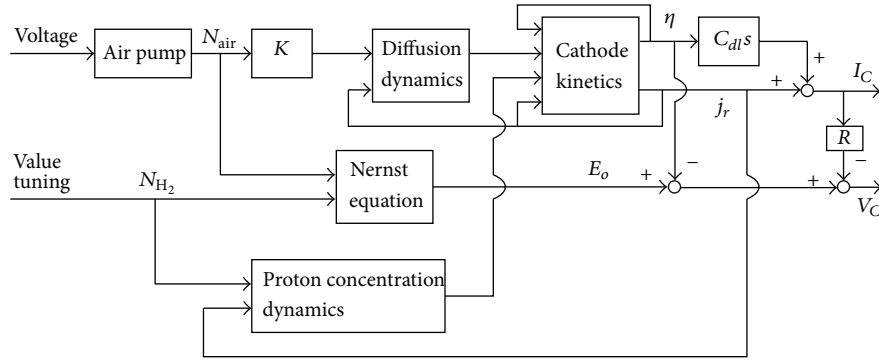


FIGURE 1: PEMFC dynamics.

the battery and electric motor simultaneously, forming the conventional hybrid powertrain. Nevertheless, the fuel cell hybrid powertrain cannot have any benefit on fuel economy. Since the power of fuel cell is large enough to drive the electric motor, the relay battery becomes unnecessary. This type of vehicle is called the fuel cell electric vehicle (FC-EV), or simply the fuel cell vehicle. Unlike FC-EV, the FC-REEV is cascaded with a battery. It utilizes a smaller power fuel cell to charge the battery while it is being driven. This scheme can ensure a higher SOC on battery packs and achieves the range extension in consequence. This idea is very suitable for urban-life electric vehicles.

Conventional REEVs use the switch regulation to control the fuel cell generator for charging. Basically, the generator initiates charging when the SOC drops to less than 20% (or in some studies, 30%) [6]. If the SOC is lower than the warning level, the generator is activated to charge the battery. This action is terminated when the SOC reaches 80%. This approach surely can recover some SOC during steering. However, there are still some disadvantages.

- If the SOC is at a low level, the vehicle will fall into a stop-and-go period. Otherwise, the vehicle will stop for a long time, and the driver will have to wait for the SOC to recover.
- The battery cannot perform charging and discharging at the same time. In highway driving, due to the continuous pedal command requests, it is difficult for the generator to charge the battery. Consequently, the SOC will drop quickly under this scenario.

In order to solve these problems, Chen et al. [7] present a dynamic programming strategy based on a multimode switch control. This paper presents a novel charging strategy based on fuzzy turning rules for fuel cell/battery electric vehicles. It also can achieve similar performances. Fuzzy control has revealed its superior performance on electric vehicle applications [8]. Compared to the conventional switch control, a fuzzy control approach is employed in this study to improve the battery SOC. This methodology can resolve the quick SOC loss problem in the conventional approach and has the potential to eliminate range anxiety. The battery's lifetime and fuel economy are of concern in the development of fuzzy

rules, which are mainly based on the energy management in the urban driving model.

This paper aims to make use of the advantages of electric vehicles driven by a fuel cell/battery to reveal a new concept on REEV. It is structured as follows. The system modeling is introduced in Section 2, followed by the fuzzy control strategy for the presented FC-REEV in Section 3. Section 4 gives illustrated examples by simulation for evaluating the investigated strategy. Finally, Section 5 offers some concluding remarks.

## 2. Modeling

**2.1. Fuel Cell Model.** The fuel cell system considered in the simulation study is based on the design manufactured by Asia Pacific Fuel Cell Technologies, Ltd. This system is powered by a proton exchange membrane fuel cell (PEMFC). The inputs of the system are hydrogen and air, while the outputs are cell voltage and current. The dynamics of the fuel cell system is nonlinear and time varying. It is influenced by many factors, including the diffusion dynamic, the Nernst equation, proton concentration dynamics, and cathode kinetics as illustrated in Figure 1 [9, 10]:

diffusion equation:

$$R_{ohm} = R_{ref} + \alpha_T (T - T_{ref}); \quad (1)$$

Nernst equation:

$$E_o = E_{ref} + \frac{dE_o}{dT} (T - T_{ref}) + k \frac{RT}{zF} \ln (P_{H_2} P_{O_2}^{0.5}); \quad (2)$$

proton concentration dynamics:

$$u \left( \frac{-\partial C_{H^+}}{\partial t} \right) \frac{\partial C_{H^+}}{\partial t} + \frac{C_{H^+}}{\tau_{H^+}} = \frac{1 + \alpha_{H^+} + j^3}{\tau_{H^+}}; \quad (3)$$

cathode kinetics:

$$\eta = b \ln \left\{ \frac{p_{10} [H^+]_0}{p_1 [H^+]} \left( 1 + \frac{j_r}{j_0 A_r} \right) \right\}. \quad (4)$$

From the system point of view, the physical model of Figure 1 can be represented as a multi-input and multioutput (MIMO)

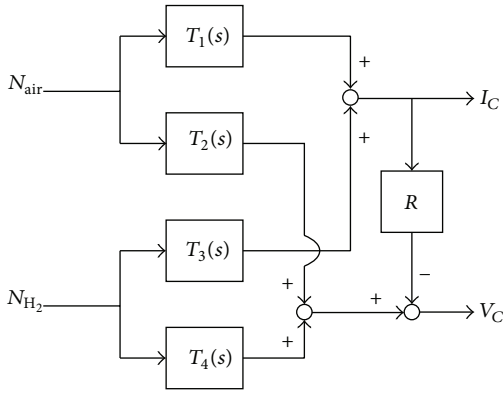


FIGURE 2: Block diagrams of fuel cell system.

system, as depicted in Figure 2, with the following relation [11]:

$$I_C = T_1(s) N_{Air} + T_3(s) N_{H_2}, \quad (5)$$

$$V_C = T_2(s) N_{Air} + T_4(s) N_{H_2} - RI_C.$$

$T_1(s) \sim T_4(s)$  represent the transfer functions of the subsystem. Note that the dynamics of linearized model (5) depends on the operating conditions.

**2.2. Battery Model.** The battery model in the simulation study is simplified as an equivalent circuit with a voltage source and a resistance [12–16], which is also called the  $R_{int}$  model and can be seen in Figure 3. The thermal effect on battery dynamics is ignored by assuming that the battery temperature will not experience major changes during the system testing. In Figure 3,  $V_{oc}$  is the open-circuit voltage of the battery,  $R_{in}$  stands for the internal resistance, and  $I_b$  represents the battery current. By considering the charging and discharging requirements, the SOC is obtained from the amount of capacity that remains after discharge from a top-of-charge condition as [17]

$$SOC(t) = Q_T - \int_{t_0}^t i(\tau) d\tau = Q_T - \Delta q. \quad (6)$$

Herein,  $Q_T$  is the theoretical capacity of a battery and  $i(\tau)$  is the current demand from electric motor. Note that  $\Delta q$  can also be recovered when the fuel cell generator is charging the battery. Additionally, practical capacity  $Q_P$  of a battery is always much lower compared to the theoretical capacity  $Q_T$  due to practical limitations and battery protections. Herein,

$$Q_P(t) = \int_{t_0}^{t_{cut}} i(\tau) d\tau. \quad (7)$$

Due to the fact that the behaviors of charging and discharging in chemical batteries are depending on the chemical reaction rate and safety control of battery protection, the current function  $i(\tau)$  always falls on a nonlinear function. This behavior can be affected by room temperature, material fatigue, and so on. In this paper, the dynamics of employed

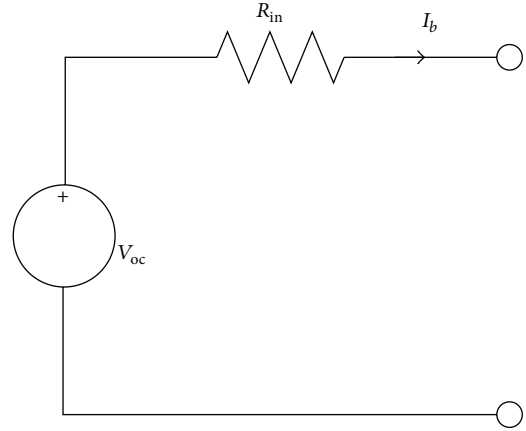


FIGURE 3: Equivalent circuit of simplified battery model.

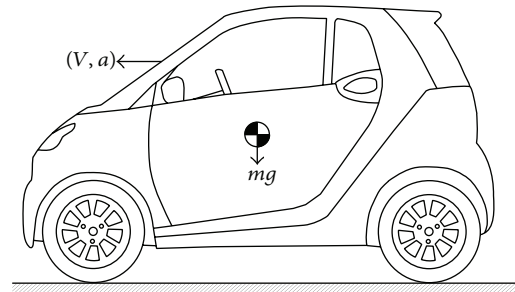


FIGURE 4: Vehicle model.

battery is directly adopted from the simulation tools and will be revealed in Section 4 as well.

According to the investigation results in [16], obviously, to improve the dynamic voltage prediction precision of the battery model, recursive approaches are better due to the nonlinear behaviors of a battery. For example, the data-driven based parameters identification approach in [16] reveals a potential to achieve high voltage estimation accuracy against different aging levels and operation environments. Note that the behaviors to dynamic reactions on a chemical battery are sophisticated. Consequently, there are many battery models proposed to probe the system performance. Based on the similar testing setup in [15], the employed model (i.e.,  $R_{int}$  model) reveals almost the same performance as the Thevenin Model, RC Model, PNGV Model, and DP Model. For some critical driving, the SOC prediction based on these approaches shows different errors. However, in urban driving cycles such as the NEDC, these approaches almost share the same reliability. In this paper, the driving scenarios are mainly based on the urban driving for range-extended fuel cell/battery electric vehicles. Consequently, the utilized battery model already has sufficient ability to carry out the analysis for the presented study.

**2.3. Vehicle Dynamics.** Consider a four-wheeled vehicle in a longitudinal motion, as depicted in Figure 4; the dynamic equations for the longitudinal motion of the vehicle can be found from Newton’s second law of motion [18].

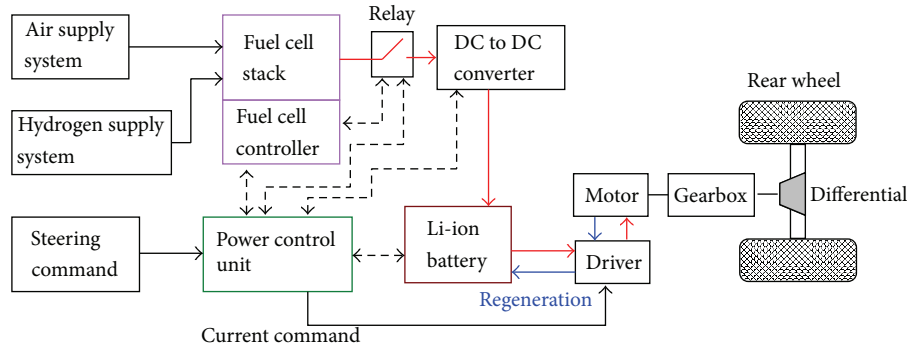


FIGURE 5: Schematics of presented FC-REEV system.

The forces of vehicle driving include air drag, rolling resistance, accelerating force, and climbing force. Hence, the power  $P_d$  needed in vehicle operation can be found as

$$P_d = \left( ma + C_R mg + mg \sin \theta + \frac{1}{2} \rho_a C_D A_F V^2 \right) V, \quad (8)$$

where  $m$  is the mass of the vehicle,  $a$  stands for the acceleration of the vehicle,  $C_R$  is the coefficient of rolling resistance,  $g$  is the gravity constant,  $\theta$  is the gradient angle,  $\rho_a$  is the density of air,  $C_D$  is the drag coefficient, and  $A_F$  is the frontal projected area of the vehicle. For regular steering, these mechanical power assumptions are the major sources of electric power supplied by a lithium-ion battery and fuel cell generator. Note that, in practice, the main battery also supplies electricity to consumptions such as air conditioning and headlights. In order to avoid missing the focus of analysis, these auxiliary power losses are omitted for simplification.

**2.4. System Construction.** Figure 5 shows the schematics of the presented FC-REEV system. In order to evaluate the proposed range extension strategy, the whole system model, as shown in Figure 5, is implemented in the simulation of MATLAB/Simulink. As can be seen in this figure, a traction motor is employed for delivering torques to the rear wheels. The individual motor is a 10 kW three-phase AC 72V motor. The maximum motor speed is 2000 rpm. The fuel cell power is 4 kW, and the lithium-ion battery has a capacity of 105 Ah. The vehicle weighs 900 kg. Note that the motor can also be operated as a generator during the braking cycle. Basically, from the current direction, one can determine the operation mode. As depicted in Figure 5, a power control unit (PCU) plays an important role in the system management. In some studies, PCU is also referred to as the electronic control unit (ECU) because it regulates all of the subsystems. For example, the relay switch is controlled by PCU, which decides the activation of the fuel cell generator for battery charging. Ostensibly, different power management strategy results in different fuel economy and driving experiences.

### 3. Proposed Range Extension Strategy

**3.1. Simulated Driving Cycle.** Driving cycle is a simulation pattern for evaluating the vehicle's fuel economy in different

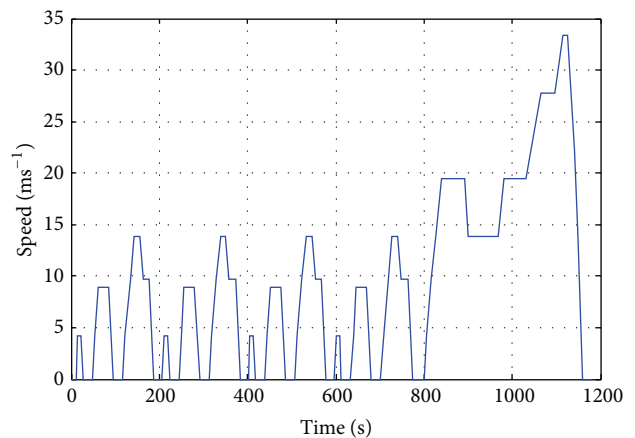


FIGURE 6: Driving pattern of NEDC.

scenarios. It is an important tool for design in driveline and control strategies. The main purpose in powertrain design is to minimize fuel consumption and component costs, while maximizing drivability. Since it is still cost-ineffective to build prototypes of FC-EV, the FC-REEV becomes an alternative in early stages of the development. The driving cycle is formed from numerous tests. Nowadays, it is a standard process in fuel economy evaluation. Basically, driving cycle is a speed profile where the most common scenarios of steering, such as rapid traction, braking, and coasting, are concerned. Its speed profile is defined as a function of time for a fair evaluation. Several driving cycles have been developed by governments around the world as tools for vehicle certification. The famous New European Drive Cycle (NEDC) in Europe and the Federal Test Procedure (FTP) in the USA are sufficient benchmarks. In this study, as shown in Figure 6, the driving pattern of NEDC is employed to evaluate the fuel economy and range extension. It is known that the NEDC is composed of four ECE-15 (urban driving cycle) segments as well as an EUDC (extraurban driving cycle) segment. Each ECE-15 cycle is 195 sec and 0.9941 km long, and its modeling covers the most typical urban driving scenarios in metropolitan areas. The EUDC is 400 sec and 6.9549 km long for high-speed urban driving. The combined fuel economy is calculated by a total consumption of urban and extraurban cycles over 10.9314 km.

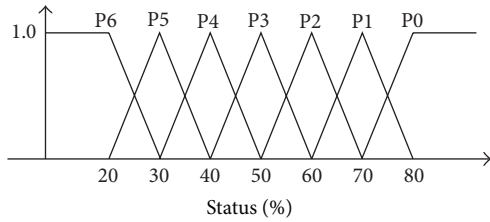


FIGURE 7: Triangular membership functions.

The entire test procedure requires 1180 sec with an average speed of  $33.35 \text{ kmh}^{-1}$ .

In other words, one cycle of the NEDC is just 10.9314 km. It is not sufficient to represent all urban driving situations. Therefore, in this study, the driving pattern of NEDC is repeated ten times (i.e., 109.314 km) for a more realistic steering scenario. Under this assumption, the fuel economy and reliability of the FC-REEV can further reveal its major contribution to range extension.

**3.2. Fuzzy Range Extension Strategy.** As mentioned in the Introduction, because the battery cannot be charged and/or discharged simultaneously, the extended range of REEV is mainly relevant to the charging style to the battery. The conventional switch control strategy, which is also named the thermostat control strategy (TCS) in [19, 20], has achieved some success on REEV range extension; however, the battery charging dynamics is not nimble. It shows a drawback on a stop-and-go duration when the SOC is under a low level. The results give a clue that the generator power management could be more effective. In order to improve this inconvenient driving experience, this paper proposes a new range extension strategy based on fuzzy control.

Generally, when controlling a process, human operators usually encounter complex patterns of qualitative conditions, which are not easy to quantify. For example, in many applications, the measurement data can be classified as fast, slow, high, low, and so on. Such linguistic variables are employed in describing inexact information. To represent such information, a new mathematical approach called fuzzy theory was proposed by Zadeh [21]. In essence, the fuzzy control is a mechanism that offers the designer to create solutions for control issues. It mimics and duplicates the techniques and knowledge based on human intelligence and decisions. In this paper, the fuzzy control is utilized for monitoring the battery's SOC. As illustrated in Figure 7, a fuzzy membership function (fuzzy sets) of the required status is defined with the following linguistic fuzzy set, where

- P0: status > 80%,
- P1: status = 70%,
- P2: status = 60%,
- P3: status = 50%,
- P4: status = 40%,
- P5: status = 30%,
- P6: status ≤ 20%.

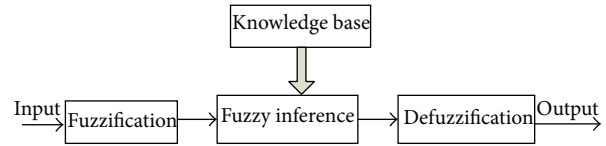


FIGURE 8: Fuzzy controller block diagram.

The shape of the membership functions is quite arbitrary and is dependent on the user's preference. For the sake of mathematical simplicity, the triangular shape is utilized due to practical considerations. Note that there are many membership functions that can be utilized. The triangular membership function is one of the candidates. Based on the research results from Pedrycz [22], the triangular membership function works well in most of the industrial applications. Additionally, based on its linear and easier computation features, this study adopts this type of membership function to carry out the fuzzification process.

Due to the guarantee of expert experience, most commercial fuzzy products are rule-based systems. They receive the current states in the feedback loop and check the rules for control and operation. A basic fuzzy logic system can be found in Figure 8. Crisp input states are converted into fuzzy values based on fuzzy sets with the fuzzification block. The fuzzy controller is mainly based on the knowledge database denoted in the fuzzy rules. The decision-making-logic determines how the fuzzy logic operations are performed and precedes the outputs of each fuzzy rule in an "IF-THEN" policy. Finally, these processes are then converted into crisp values with the defuzzification block. The output crisp values then achieve the regulation for specific tasks.

Table 1 shows the presented fuzzy rules. Basically, these rules are derived from the experts' experience. The major rules consist of the following strategies.

*Case 1.* The fuel cell generator supplies 100% for battery charging. The pedal uses 0% for the acceleration.

*Case 2.* The fuel cell generator supplies 67% for battery charging. The pedal takes 33% for the acceleration.

*Case 3.* The fuel cell generator supplies 33% for battery charging. The pedal utilizes 67% for the acceleration.

*Case 4.* The fuel cell generator supplies 44% for battery charging. The pedal uses 56% for the acceleration.

*Case 5.* The fuel cell generator supplies 22% for battery charging. The pedal receives 78% for the acceleration.

*Case 6.* The fuel cell generator supplies 11% for battery charging. The pedal is allocated 89% for the acceleration.

Note that the percentage of the charging/pedal sharing ratio is adjustable according to a specific index. Additionally, the distance is strictly indexed by ten cycles of NEDC (i.e., 109.314 km). The fuzzy controller receives statuses of the range

TABLE 1: Fuzzy rules.

	P6 of distance	P5 of distance	P4 of distance	P3 of distance	P2 of distance	P1 of distance	P0 of distance
P6 of SOC	Case 1	Case 1	Case 2	Case 2	Case 2	Case 3	Case 3
P5 of SOC	Case 1	Case 1	Case 2	Case 2	Case 2	Case 3	Case 3
P4 of SOC	Case 1	Case 1	Case 2	Case 2	Case 2	Case 3	Case 3
P3 of SOC	Case 2	Case 2	Case 4	Case 4	Case 4	Case 5	Case 5
P2 of SOC	Case 2	Case 2	Case 4	Case 4	Case 4	Case 5	Case 5
P1 of SOC	Case 3	Case 3	Case 5	Case 5	Case 5	Case 6	Case 6
P0 of SOC	Case 3	Case 3	Case 5	Case 5	Case 5	Case 6	Case 6

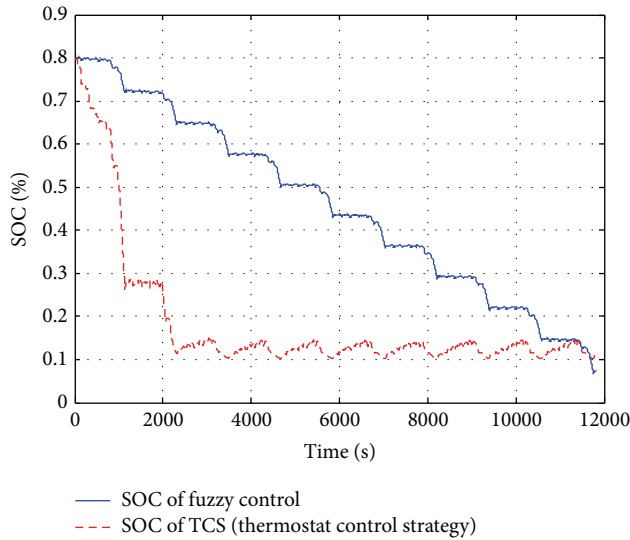


FIGURE 9: Comparative simulations of SOC.

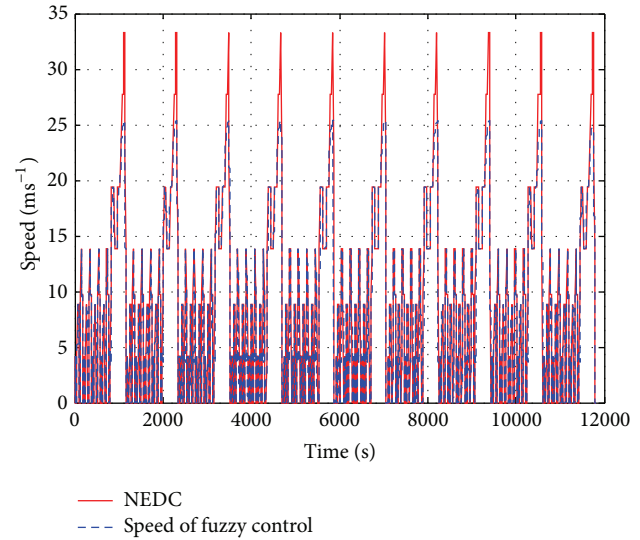


FIGURE 10: Speed profile of fuzzy control.

and SOC from feedback sensors and regulates the duty ratio between the SOC and pedal.

#### 4. Results and Discussions

In this section, the presented fuzzy control approach is tested in simulation for performance verification. The whole system of Figure 5 was employed as a platform for evaluation. Figure 9 reveals the comparative results on SOC. As can be seen in this figure, the TCS approach falls into a stop-and-go status quickly. Conversely, the presented approach can reach the goal without any extra stops. Although the vehicle completes the test of range extension, the whole driving experience is very different. For the conventional approach, range anxiety still exists. The comparative simulation results confirm that the charging strategy plays an important role in the driving experience. From the viewpoint of range extension, both approaches achieve the goal. However, the steering experience is quite different; the fuzzy charging policy can maintain the SOC at a relatively high level to avoid the vehicle falling into a stop-and-go stage. The vehicle can accomplish nearly a no parking situation for battery charging. Fewer stops mean the vehicle's motion can follow the driving cycle smoothly and the kinetic energy can be sufficiently

kept; hence, this finding represents a higher energy efficiency. In addition, the user does not feel significant change when driving with the proposed FC-REEV. Therefore, the driving experience of the proposed system will be almost the same as the conventional engine car.

Figure 10 illustrates the speed performance of the proposed fuzzy control system. As can be seen in this figure, due to the duty management of pedal command sharing, the speed incensement will become sluggish in the high-speed zone. Conventionally, since the pedal command consists of the energy demand from the battery, there is no time slot for the battery to capitalize on charging from the generator. Moreover, because the battery in this scenario is continuously discharging, the SOC drops quickly as a result. In order to overcome the lack of time for charging the REEV during high-speed steering, the proposed fuzzy rules use the pedal time sharing concept to improve the quick loss problem. This idea utilizes the duty-sharing concept to gain some charging time during operation. This methodology solves the quick SOC loss problem and can maintain a smooth driving experience while the vehicle is at a high speed. The tradeoff is that the vehicle's speed increases slowly when the acceleration demand is suddenly given. However, due to the inertial momentum of vehicle, the motion behavior can be continuous. Hence, the proposed approach can still

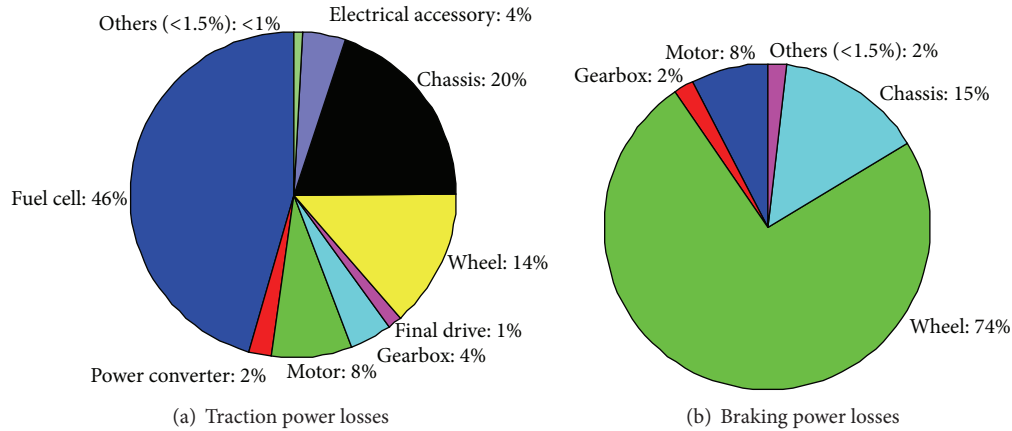


FIGURE 11: Vehicle traction/braking power losses.

maintain safe steering for the operator and passenger(s). This experience is a better option than its stop-and-go alternative. Regarding the protection issue of a chemical battery's lifetime, a small discharge cycle is preferred than a long one [22]. Clearly, the presented fuzzy control attempts to avoid continuous deep discharge of the battery. This policy also facilitates the lifetime protection of battery packs. On the other hand, the conventional approach charges the battery when it is at a low SOC level. Multiple deep discharge cycles at this level will result in a fast deterioration and material decay of battery packs.

Considering the fuel efficiency issue, Figure 11 shows the total power losses for the vehicle's traction and braking in the whole 109.314 km. The energy in fuel is consumed by various losses, such as the driving resistances, gear wearing, propelling kinetic energy, generator, and vehicular electronics. Basically, the fuel economy of a vehicle's propulsion is the fuel efficiency relationship between the traveled distance and the amount of energy consumed by the system. Additionally, different driving cycles and driver behaviors result in different outcomes. Maximizing the usages of chemical energy in fuel as much as possible on the propelling of the vehicle becomes a key task. As can be seen in Figure 11, the power loss during forward traction and braking is 15.1996 kW and 2.0481 kW, respectively. Obviously, the fuel cell generator dissipates the major power when the vehicle is in a traction state. Under the framework of system limitation, such as the structure of Figure 5, the only way to foster better fuel economy is to improve the energy efficiency of the generator. According to Demirdöven and Deutch [23], the PEMFC for transportation applications has higher energy efficiency than the conventional gasoline/diesel generator. Consequently, for REEV, the fuel cell generator is a suitable choice based on the inspection of fuel economy. Conversely, as the vehicle initiates braking, the major power is consumed by the wheel wearing. It is easy to realize that the energy losses from braking mainly come from the tires. The tires consume the majority of kinetic energy and hence stop the vehicle. If the motor driver can perform regeneration during braking, undoubtedly, the kinetic energy can be further recycled to achieve higher energy efficiency.

## 5. Conclusions

This paper has investigated the novel range extension strategy for fuel cell/battery electric vehicles. The analysis was carried out by the simulation results done by MATLAB/Simulink. The presented charging sharing idea, which is regulated by a fuzzy rule table, has revealed that the quick loss of SOC can be remedied for high-speed steering. The battery's lifetime and system's fuel economy have confirmed an improvement under the proposed energy management. These evaluations have demonstrated its effectiveness and potential feasibility. The main findings from the simulation results are described below.

- (1) Under the regulation of sufficient fuzzy control, the urban driving experience for FC-REEV can be the same as the internal combustion engine car. Hence, range anxiety can be fully managed in the proposed approach.
- (2) Fuzzy strategy also improves the battery's lifetime and fuel economy of a REEV system. A safe and continuous driving experience is guaranteed in the proposed FC-REEV. The operator can enjoy almost the same driving experience as the conventional engine car.
- (3) FC-REEV has revealed a better fuel economy than the conventional REEV. Additionally, the FC-REEV is a purely zero-CO<sub>2</sub> emission car.
- (4) The energy consumption from the gearbox can be further saved when the powertrain design is changed. For example, the power decentralized electric vehicles that utilize the in-wheel motor to propel the vehicle's motion can achieve less heat loss on gear wearing. Investigations of relevant issues are worth studying in future work.

## Conflict of Interests

This publication has been approved by all the authors and explicitly by the responsible authorities where the work was

carried out. The authors declare that there is no conflict of interests regarding the publication of this paper.

## Acknowledgments

This work was supported by the Ministry of Economic Affairs (MOEA) of Taiwan and Science Park Administration (SPA) of Taiwan under Projects of MOEA 102-D0621 and SPA 102A38, respectively.

## References

- [1] Y. Hori, "Future vehicle driven by electricity and control-research on four-wheel-motored "UOT Electric March II", *IEEE Transactions on Industrial Electronics*, vol. 51, no. 5, pp. 954–962, 2004.
- [2] J.-S. Hu, D. Yin, and Y. Hori, "Fault-tolerant traction control of electric vehicles," *Control Engineering Practice*, vol. 19, no. 2, pp. 204–213, 2011.
- [3] J.-S. Hu, D. Yin, Y. Hori, and F.-R. Hu, "Electric vehicle traction control: a new MTTE methodology," *IEEE Industry Applications Magazine*, vol. 18, no. 2, pp. 23–31, 2012.
- [4] J. J. Hwang and W. R. Chang, "Characteristic study on fuel cell/battery hybrid power system on a light electric vehicle," *Journal of Power Sources*, vol. 207, pp. 111–119, 2012.
- [5] J. Neubauer, A. Brooker, and E. Wood, "Sensitivity of plug-in hybrid electric vehicle economics to drive patterns, electric range, energy management, and charge strategies," *Journal of Power Sources*, vol. 236, pp. 357–364, 2013.
- [6] J.-J. Hwang, J.-K. Kuo, W. Wu, W.-R. Chang, C.-H. Lin, and S.-E. Wang, "Lifecycle performance assessment of fuel cell/battery electric vehicles," *International Journal of Hydrogen Energy*, vol. 38, no. 8, pp. 3433–3446, 2013.
- [7] B.-C. Chen, Y.-Y. Wu, and H.-C. Tsai, "Design and analysis of power management strategy for range extended electric vehicle using dynamic programming," *Applied Energy*, vol. 113, pp. 1764–1774, 2014.
- [8] C. Geng, L. Mostefai, M. Denai, and Y. Hori, "Direct yaw-moment control of an in-wheel-motored electric vehicle based on body slip angle fuzzy observer," *IEEE Transactions on Industrial Electronics*, vol. 56, no. 5, pp. 1411–1419, 2009.
- [9] F.-C. Wang, H.-T. Chen, Y.-P. Yang, and J.-Y. Yen, "Multivariable robust control of a proton exchange membrane fuel cell system," *Journal of Power Sources*, vol. 177, no. 2, pp. 393–403, 2008.
- [10] M. Ceraolo, C. Miulli, and A. Pozio, "Modelling static and dynamic behaviour of proton exchange membrane fuel cells on the basis of electro-chemical description," *Journal of Power Sources*, vol. 113, no. 1, pp. 131–144, 2003.
- [11] F.-C. Wang, Y.-P. Yang, C.-W. Huang, H.-P. Chang, and H.-T. Chen, "System identification and robust control of a portable proton exchange membrane full-cell system," *Journal of Power Sources*, vol. 164, no. 2, pp. 704–712, 2007.
- [12] S. J. Gerssen-Gondelach and A. P. C. Faaij, "Performance of batteries for electric vehicles on short and longer term," *Journal of Power Sources*, vol. 212, pp. 111–129, 2012.
- [13] M. Dubarry, N. Vuillaume, and B. Y. Liaw, "From single cell model to battery pack simulation for Li-ion batteries," *Journal of Power Sources*, vol. 186, no. 2, pp. 500–507, 2009.
- [14] L. Gao, S. Liu, and R. A. Dougal, "Dynamic lithium-ion battery model for system simulation," *IEEE Transactions on Components and Packaging Technologies*, vol. 25, no. 3, pp. 495–505, 2002.
- [15] H. He, R. Xiong, and J. Fan, "Evaluation of lithium-ion battery equivalent circuit models for state of charge estimation by an experimental approach," *Energies*, vol. 4, no. 4, pp. 582–598, 2011.
- [16] R. Xiong, F. Sun, X. Gong, and C. Gao, "A data-driven based adaptive state of charge estimator of lithium-ion polymer battery used in electric vehicles," *Applied Energy*, vol. 113, pp. 1421–1433, 2014.
- [17] I. Husain, *Electric and Hybrid Vehicles: Design Fundamentals*, CRC Press, New York, NY, USA, 2003.
- [18] S.-I. Sakai, H. Sado, and Y. Hori, "Motion control in an electric vehicle with four independently driven in-wheel motors," *IEEE/ASME Transactions on Mechatronics*, vol. 4, no. 1, pp. 9–16, 1999.
- [19] J.-P. Gao, G.-M. G. Zhu, E. G. Strangas, and F.-C. Sun, "Equivalent fuel consumption optimal control of a series hybrid electric vehicle," *Proceedings of the Institution of Mechanical Engineers, Part D: Journal of Automobile Engineering*, vol. 223, no. 8, pp. 1003–1018, 2009.
- [20] A. Mirabadi and M. Najafi, "Energy management system in hybrid trains using fuzzy control: a comparative study," *Proceedings of the Institution of Mechanical Engineers Part F: Journal of Rail and Rapid Transit*, vol. 225, no. 3, pp. 267–276, 2011.
- [21] L. A. Zadeh, "Fuzzy sets," *Information and Computation*, vol. 8, pp. 338–353, 1965.
- [22] W. Pedrycz, "Why triangular membership functions?" *Fuzzy Sets and Systems*, vol. 64, no. 1, pp. 21–30, 1994.
- [23] N. Demirdöven and J. Deutch, "Hybrid cars now, fuel cell cars later," *Science*, vol. 305, no. 5686, pp. 974–976, 2004.

## Research Article

# Conventional, Hybrid, or Electric Vehicles: Which Technology for an Urban Distribution Centre?

**Philippe Lebeau, Cedric De Cauwer, Joeri Van Mierlo, Cathy Macharis,  
Wouter Verbeke, and Thierry Coosemans**

*MOBI Research Group, Vrije Universiteit Brussel, Pleinlaan 2, 1050 Brussels, Belgium*

Correspondence should be addressed to Philippe Lebeau; [plebeau@vub.ac.be](mailto:plebeau@vub.ac.be)

Received 21 November 2014; Accepted 25 January 2015

Academic Editor: Caiping Zhang

Copyright © 2015 Philippe Lebeau et al. This is an open access article distributed under the Creative Commons Attribution License, which permits unrestricted use, distribution, and reproduction in any medium, provided the original work is properly cited.

Freight transport has an important impact on urban welfare. It is estimated to be responsible for 25% of CO<sub>2</sub> emissions and up to 50% of particles matters generated by the transport sector in cities. Facing that problem, the European Commission set the objective of reaching free CO<sub>2</sub> city logistics by 2030 in major urban areas. In order to achieve this goal, electric vehicles could be an important part of the solution. However, this technology still faces a number of barriers, in particular high purchase costs and limited driving range. This paper explores the possible integration of electric vehicles in urban logistics operations. In order to answer this research question, the authors have developed a fleet size and mix vehicle routing problem with time windows for electric vehicles. In particular, an energy consumption model is integrated in order to consider variable range of electric vehicles. Based on generated instances, the authors analyse different sets of vehicles in terms of vehicle class (quadricycles, small vans, large vans, and trucks) and vehicle technology (petrol, hybrid, diesel, and electric vehicles). Results show that a fleet with different technologies has the opportunity of reducing costs of the last mile.

## 1. Introduction

A number of trends can be observed in urban freight transport. The current urbanization process generates more freight volumes in cities, transport is increasingly fragmented due to the success of light commercial vehicles, and distances are stretching out due to the delocalisation of logistics platforms to the periphery [1]. Because of these combined effects, vehicle-kilometres of freight vehicles are expected to increase in the future. However, urban freight transport is responsible for negative impacts on the sustainability of cities. These negative impacts can be attributed partly to the intense use of road. Vans and trucks have indeed a worse impact compared to other motor vehicles such as cars and motorcycles [2]. Even though road freight transport represents 10 to 15% of vehicle-kilometres in cities [3, 4], freight vehicles are responsible for around 25% of CO<sub>2</sub> emissions, 30% of NO<sub>x</sub> emissions, 40% of energy consumption, and 50% of particles matter [5, 6]. Also, noise nuisance caused by freight transport generates around five times more decibels than the circulation noise of private cars during morning rush hour [4]. Recognizing the need for solutions, the European Commission has set the objective of

reaching free CO<sub>2</sub> city logistics in major urban areas by 2030 [7].

Research has developed a wide range of logistics concepts, regulations, and technologies to fulfil the city logistics carbon-free target [8]. Among them, battery electric vehicles (BEVs) are considered to be an answer to the negative impacts listed above [9]. They have a particularly low environmental impact compared to conventional vehicles [10]. Several big companies such as DHL, UPS, DPD, and Japan Post have already integrated BEVs in their fleet for last mile deliveries [11]. Still, purchase costs and limited battery capacity remain the two most important barriers for BEV adoption [12]. They both contribute to the paradox of the BEV as depicted in Figure 1. On the one hand, they have to drive a high number of kilometres to be competitive with conventional vehicles. On the other hand, range is limited due to the battery capacity. As a result, BEVs fit in a specific niche. The objective of this paper is to address these constraints by comparing the use of battery electric vehicles with conventional vehicles in a delivery fleet.



FIGURE 1: The paradox of the battery electric vehicle. Source: own setup.

Based on a vehicle routing problem (VRP) that we formulated, we study the case of an urban distribution centre. It will use the (real) case of a distributor which has a depot located in Brussels. The constraint related to the limited range defines the area of possible solutions. The optimal solution is then identified by the composition of the fleet that shows the lowest total cost.

## 2. Literature Review

The organisation of delivery tours has generally been investigated through the vehicle routing problem (VRP). It is defined as “the determination of the optimal set of routes to be performed by a fleet of vehicles to serve a given set of customers” [13]. The optimisation can have different objectives such as the minimisation of traveling time or delivery costs. The VRP can be described as a travelling salesman problem (TSP) where more than one vehicle is used to serve each customer. The original VRP was introduced by Dantzig and Ramser [14] and then developed in a large variety of more complex versions.

Constraints on limited driving range were introduced with the works of Christofides et al. [15]. The VRP was designed such that a maximum cost could not be exceeded by the solution. The maximum costs parameter could be either replaced by time constraints or by distance constraints. This idea was also used by Laporte et al. [16] where distance travelled by any vehicle could not exceed a defined upper bound. They named it the distance constrained vehicle routing problem (DCVRP) and kept improving it in later works such as in Laporte et al. [17, 18].

The first attempt to investigate the specific characteristics of BEVs in a VRP was achieved by Gonçalves et al. [19]. They considered a VRP with pickup and delivery (VRPPD) and a mix fleet made of BEVs and conventional vehicles. The limited battery capacity was represented by a time constraint on charging BEVs. The approach enriched the previous work on DCVRP as the distance constraints can be extended against a loss in time due to charging the battery. However, the locations of charging spots were not considered in the model, meaning that BEVs could virtually recharge anywhere on the delivery round once the battery was empty. Erdoğan and Miller-Hooks [20] brought a solution to the weaknesses of Gonçalves et al. [19] by developing the green VRP (G-VRP). They consider a network of refuelling stations that alternative fuelled vehicles can use during their delivery tour. They based their mixed integer linear program formulation on the VRP with satellite facilities (VRPSF) from Bard et al. [21]. They translated the concept of satellites facilities where the cargo of vehicles can be reloaded or unloaded during the route into charging spots where vehicles can be refuelled during the route at specific points in the network.

Erdoğan and Miller-Hooks [20] showed therefore how to consider the location of refuelling in a VRP, though the charging time considered by Gonçalves et al. [19] is missing in the G-VRP as it was not designed specifically for BEVs but for alternative fuel vehicles (i.e., biodiesel, liquid natural gas, or CNG vehicles). The contributions of Gonçalves et al. [19] and Erdoğan and Miller-Hooks [20] were integrated by Schneider et al. [11] in their electric vehicle routing problem with time windows (E-VRPTW). Charging locations and charging times are both considered in their model which approaches well the problem of BEVs. In particular, they modelled charging time of BEVs as being a function of the state of charge of the battery. Moreover, time windows and vehicle capacity restrictions are also included in the constraints of the E-VRPTW in order to adapt the model to the context of urban freight distribution.

At the same time, Conrad and Figliozzi [22] developed a solution close to that of Schneider et al. [11]. Based on a capacitated vehicle routing problem with time windows constraints (CRVRP-TW), they introduced the limited range and charging times in order to get the recharging vehicle routing problem (RVRP). Their main difference is regarding charging locations: Conrad and Figliozzi [22] consider that charging is possible at some customer locations while the formulation of Schneider et al. [11] is more flexible as other possible charging locations are possible in the network.

So far, these different papers considered VRP with a single type of vehicle. However, electric vehicles are likely to be used in delivery fleets with other kinds of vehicles. A well-studied branch of the VRP literature is precisely addressing the problem of heterogeneous fleets in delivery fleets [23]. Merging the VRP research on electric vehicles with the fleet size and mix vehicle routing problem (FSMVRPTW) is therefore relevant to come with recommendations for logistics decision makers. van Duin et al. [24] have been the first to develop this idea with their electrical vehicle fleet size and mix vehicle routing problem with time windows (EVFSMVRPTW). However, they approached the problem from the FSMVRPTW branch without considering the previous work on battery electric vehicles in VRP. As a result, the model was entailed with similar weaknesses than in Gonçalves et al. [19]: they do not consider the locations of charging points. A BEV with a battery swapping system is modelled so that the range of this BEV can be doubled. But the swapping system is not reflected in the constraints. It is in fact reflected in the range parameter of the vehicle which is simply doubled, meaning that the battery of the BEV can be swapped virtually anywhere on the road. Still, the main benefit of van Duin et al.’s work [24] is bringing the fleet size and mix approach in the discussion of electric vehicle routing problem. Hiermann et al. [25] developed that idea further to propose an E-FSMVRPTW that considers the decisions regarding the fleet composition and the choice of recharging times and locations. This work can be considered as the state of the art of delivery optimisation with BEVs.

Table 1 summarises the contributions of the different relevant papers. However, one aspect is forgotten in every paper. All BEV specific papers assume the range to decrease linearly in function of the distance driven. However, the literature

TABLE 1: Overview of the literature review.

	Fleet size and mix	Time windows	Range constraints	Charging	Energy consumption model
[15]	×	×	✓	×	×
[17]	×	×	✓	×	×
[19]	✓	×	✓	± (location is not considered)	×
[22]	×	✓	✓	✓	×
[20]	×	×	✓	✓ (charging does not depend on the state of charge)	×
[24]	✓	✓	✓	± (location is not considered)	×
[11]	×	✓	✓	✓	×
[25]	✓	✓	✓	✓	×

Source: own setup.

from engineering research recognises that range of BEVs is strongly influenced by other parameters than distance. Hayes et al. [26] show, for example, in their paper that the driving range for a specific BEV (Nissan Leaf) can change from 221 km in ideal driving conditions to 99 km in bad conditions. In order to facilitate for consumers the comparison between BEVs' performances, manufacturers have to show the range based on official drive cycles. In the United States, the EPA is used and shows a range of 121 km for the Nissan Leaf [27]. In Europe, the NEDC is used and shows a range of 200 km for the Nissan Leaf [28]. Hence, range can change to a large extent depending on the usage of the vehicle. Two current works are integrating vehicle dynamics in a VRP to estimate variable ranges [29, 30]. However, more technical knowledge is required to develop an energy model. Auxiliaries, for example, were not considered even though they represent an important part of the energy consumption.

Since Lin et al. [23] identify precisely the lack of interdisciplinary approach for solving VRP problems, the objective of this paper is to bring together the developments of the EVFSMVRPTW with real observations conducted on electric vehicles. The model we propose considers therefore the different aspects shown in Table 1. The fleet size and mix vehicle routing problem considers different vehicle sizes with either electric propulsion or internal combustion engine. They mainly differ by their payload, fixed costs, running costs, energy available in the vehicle, and their energy consumption. Charging operations are considered for battery electric vehicle at the depot with fast chargers. Finally, time windows are also considered as they are important to be considered in the context of city distribution. As a result, we call our formulation of the problem a fleet size and mix vehicle routing problem with time windows for electric vehicles (FSMVRPTW-EV).

### 3. Methodology

**3.1. The Parameters Influencing the Range of BEV.** The range of an electric vehicle is determined by the amount of energy at disposal in the battery and the energy consumption of

the vehicle. The available total energy in the batteries for vehicles is called the battery capacity and the remaining amount of energy during use is called the state of charge (SoC) and is expressed in percentage "charge" remaining.

The energy required at the wheels to drive a vehicle is determined by the vehicle dynamics. Based on El Baghdadi et al. [31], we can express a theoretic energy consumption  $E_{ij}$  at the wheels for a distance  $d_{ij}$  using the vehicle dynamics described in

$$E_{ij} = \frac{1}{3600} \left[ m_{ij} \cdot g \cdot (\omega \cdot \cos \varphi + \sin \varphi) + 0.0386 \cdot (\rho \cdot \sigma \cdot \mu \cdot b_{ij}^2) + (m_{ij} + m_f) \cdot \frac{db}{dt} \right] d_{ij}, \quad (1)$$

where  $E_{ij}$  is mechanical energy required at the wheels to drive on a distance  $d_{ij}$  (kWh),  $m_{ij}$  is vehicle mass (kg),  $m_f$  is fictive mass of rolling inertia (kg),  $g$  is gravitational acceleration (9.81 m/s<sup>2</sup>),  $\omega$  is vehicle coefficient of rolling resistance (-),  $\varphi$  is road gradient angle (°),  $\rho$  is air density (1.226 kg/m<sup>3</sup>),  $\sigma$  is drag coefficient of the vehicle (-),  $\mu$  is max. vehicle cross-section (m<sup>2</sup>),  $b_{ij}$  is vehicle speed between the point  $i$  and the point  $j$  (km/h), and  $d_{ij}$  is distance driven from point  $i$  to point  $j$  (km).

The first term of the formula assesses the rolling resistance due to the work of deformation on wheel from the contact with the road. It also considers the required potential energy for hill climbing. The second term assesses the aerodynamic drag (losses), which are heavily dependent on the shape of the vehicle and the driving speed. Finally, the third term considers the energy required for acceleration. By combining these three factors, we can estimate the theoretical force to move the vehicle. If we consider the distance on which this force is applied, we compute the energy required to move the vehicle.

Driving the vehicle is however not the only source of energy consumption. Auxiliaries (AC, heating, etc.) represent another important part of energy consumption. Additionally,

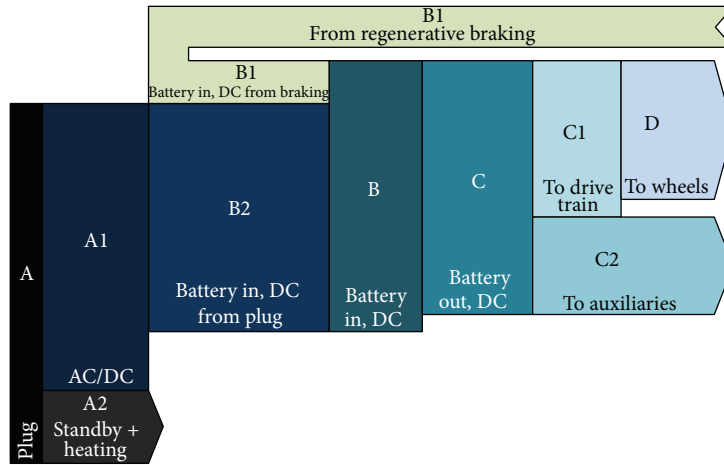


FIGURE 2: Energy losses from plug to the wheels of battery electric vehicles. Source: [32].

to deliver energy from the battery to the wheels and auxiliaries, the energy is submitted to a number of conversion stages, each comprising energy losses, as estimated by De Vroey et al. [32]. On the other hand, the amount of available energy is increased by the ability of the electric vehicle to recover (regenerated) part of the kinetic (braking) or potential (hill descend) energy. Figure 2 shows how energy is transmitted from the grid to the wheels and how it is distributed between the drive train and auxiliaries in the final stage.

An accurate range model is therefore the combination of an accurate SoC estimation and an accurate energy consumption estimation. As energy consumption varies considerably with changing circumstances, a large impact on the vehicle’s range is expected. Therefore, a first energy consumption model using real-life BEV consumption measurements and the vehicle dynamics can result in a more realistic range estimation of BEVs in the VRP.

**3.2. Data Collection and Assumptions.** In order to model the energy consumption of BEVs in the FSMVRPTW-EV, we used real observations of the energy consumption of a Nissan Leaf collected from December 2012 until December 2013. For each trip, duration, distance, and date were monitored. Most importantly, the energy consumed and recovered during the trip was registered. Since the car was shared between different drivers, a variety of driving behaviours could also be observed in our data. After filtering the sample, eliminating very short trips (less than 1km) and corrupted data, we kept 838 observations for analysis.

Based on these data, we modelled the energy consumed through an ordinary least squares analysis. We considered the theoretical relationships described in the previous section to explain the energy consumption. Hence, before the ordinary least square analysis is conducted, the theoretical energy required by the electric drivetrain was estimated for each trip based on vehicle dynamics. But some information was missing in the description of the trips such as acceleration and road gradient. Also, energy losses when converting electrical

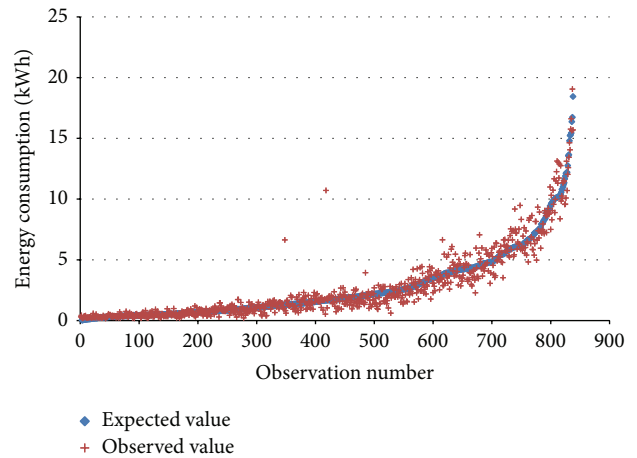


FIGURE 3: Observed and expected energy consumption of electric vehicle trips. Source: own setup.

energy to mechanical is missing. This information should be however considered in the model through the error term or the coefficient  $\beta$  of the ordinary least square analysis. We also assumed auxiliary consumption to be a function of time. Finally, since temperature affects the consumption of both auxiliary and drivetrain efficiencies, an additional parameter is included for correctional purposes. As a result, we explain the energy of a trip according to the function described in

$$\text{EnergyConsumption}_{\text{trip}} = \alpha * \text{Duration}_{\text{trip}} + \beta * E_{ij} + \gamma * \text{Temperature}_{\text{trip}} + \epsilon. \tag{2}$$

The nonlinear least square analysis showed that the variables chosen were very significant with a  $P$  value of  $2.39e - 113$ ,  $9.42e - 235$ ,  $5.44e - 6$ , and  $7.42e - 5$  for, respectively,  $\alpha$ ,  $\beta$ ,  $\gamma$ , and  $\epsilon$ . The model is also assessed to be excellent with a  $R^2$  of 0.93. In Figure 3, we can see the distribution of the expected and the observed values.

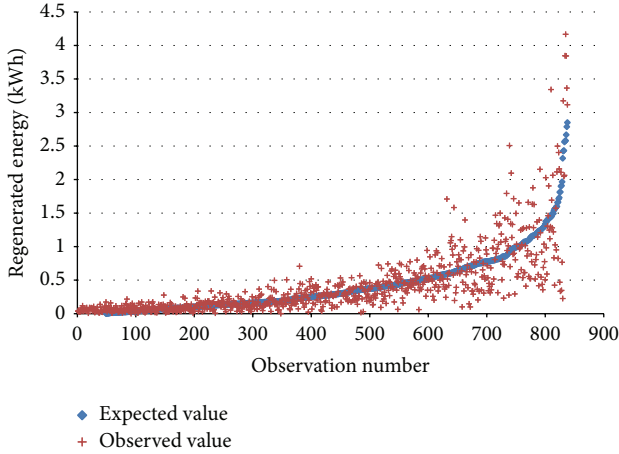


FIGURE 4: Observed and expected regenerated energy of electric vehicle trips. Source: own setup.

As the section above described, there is also a positive flow of energy with regenerative braking. In order to model the contribution of the regenerated energy, we developed also a model through an ordinary least squares analysis. We used the function described in (3) to explain the regenerative energy in function of duration of the trip, distance, and the temperature:

$$\begin{aligned} \text{RegeneratvEnergy}_{\text{trip}} &= \delta * \text{Distance}_{\text{trip}} + \theta * \text{Temperature}_{\text{trip}} \\ &+ \pi * \text{Duration}_{\text{trip}} + \tau. \end{aligned} \quad (3)$$

Each variable was assessed to be very significant with a respective  $P$  value of  $2.73e-33$ ,  $3.59e-8$ , and  $3.97e-45$ . The constant error term had also a very low  $P$  value with  $2e-8$ . Figure 4 shows the distribution of observed and expected values of the regenerated energy. The  $R^2$  is 0.77.

By combining both models in the FSMVRPTW-EV, we can estimate the depletion of the battery in function of the route taken by the BEV. The energy capacity of the battery vehicle is reduced by its specific consumption on each route. Let us note that this specific consumption considers the average driving behaviour from our observations.

**3.3. The FSMVRPTW-EV.** The formulation of the fleet size and mix vehicle routing problem with time windows for electric vehicles (FSMVRPTW-EV) is based on the FSMVRPTW of Belfiore and Yoshizaki [33] and the G-VRP of Erdoğan and Miller-Hooks [20]. It is defined on a complete and directed graph  $G = (V, A)$ .  $V$  denotes a set of vertices with  $V = C \cup \{v_0\}$ .  $C$  is a set of  $n$  customers with  $C = \{v_1, v_2, \dots, v_n\}$  and  $\{v_0\}$  stands for the depot. Then, set  $A$  represents the set of arcs connecting the vertices of  $V$ , with  $A = \{(v_i, v_j) \mid v_i, v_j \in V, i \neq j\}$ . Each arc  $(v_i, v_j)$  is associated with a distance  $d_{ij}$ , a speed  $b_{ij}$ , and a traveling time  $t_{ij}$ .

$P$  represents a set of  $k$  vehicles with  $P = \{p_1, p_2, \dots, p_k\}$ . They are either BEVs or conventional vehicles. Hence, they have different properties. They differ according to their fixed

costs  $f_k$ , their running costs  $g_k$ , their payload  $m_k$ , and their volume capacity  $a_k$ . They differ also according to their energy capacity  $z_k$  and the energy consumption  $h_{ij}^k$  they spend to travel from  $v_i$  to  $v_j$ . The energy capacity is reduced by 10% of the announced battery capacity to take into account the maximum depth of discharge. The energy consumption is based on the range model presented in the previous section. On the other hand, the vehicles share common characteristics. The driver cost  $c$  (€/hour) remains the same across vehicles. Vehicles start and end at the depot  $v_0$ . They travel in the directed graph  $G$  so that the demand of every customer is fulfilled. Demand is described both in terms of volume with  $q_n$  and in terms of weight with  $o_n$ . Each vertex of  $C$  is associated with a time window  $[l_i, u_i]$  and a service time  $s_i$ . Deliveries cannot start before  $l_i$  and after  $u_i$  but can end after  $u_i$  given the service time  $s_i$ . Once the vehicle  $k$  has come back to the depot, the used vehicle can do additional routes and become vehicle  $k'$ . Hence,  $P'$  denotes the set of used vehicles. Vehicles in  $P'$  have a fixed cost of zero since it has already been considered in their first route, but they are available later. Let us note that recharging is possible for BEV at the depot only. BEV can fast charge with a power  $r$  during their loading/unloading operations that we consider set at 50 kW. In order to optimise the lifetime performance of the batteries, they can reach a maximum state of charge of 80% of their initial capacity. We assume in our model that a fast charger is always available at the depot.

The objective of the FSMVRPTW-EV is to minimise the total costs of fulfilling the demand of customers within their time windows. The binary decision variables  $x_{ij}^k \mid k \in P, i, j \in V, i \neq j$  represent the resulting route followed by the vehicles such that  $x_{ij}^k$  equals 1 if the arc  $(i, j)$  has travelled and 0 otherwise. Besides, vertices are associated with additional decision variables:  $e_i^k$  shows the available energy of vehicle  $k$  at customer  $i$ ,  $a_i^k$  gives the available volume capacity of vehicle  $k$  at customer  $i$ ,  $m_i^k$  denotes the available payload of vehicle  $k$  at customer  $i$ , and  $w_i^k$  gives the time of arrival of vehicle  $k$  at customer  $i$ .

*Indices and Sets*

- $i, j$ : Vertex indices
- $V$ : Set of all vertices with  $V = I \cup \{v_0\}$
- $C$ : Set of  $n$  customers with  $C = \{v_1, v_2, \dots, v_n\}$
- $A$ : Set of arcs with  $A = \{(v_i, v_j) \mid v_i, v_j \in V, i \neq j\}$
- $P$ : Set of  $k$  vehicles with  $P = \{p_1, p_2, \dots, p_k\}$ .

*Parameters*

- $v_n$ : The customer  $n$  with  $v_n \in I$
- $v_0$ : Depot with  $v_0 \in V$
- $q_n$ : Volume of goods to be delivered at customer  $n$  ( $m^3$ )
- $o_n$ : Weight of goods to be delivered at customer  $n$  (kg)
- $l_n$ : Lower bound of the time windows for customer  $n$  (h-time)

- $u_n$ : Upper bound of the time windows for customer  $n$  (h-time)
- $s_n$ : Service time to deliver customer  $n$  or to load the vehicle if  $n = 0$  (h-duration)
- $d_{ij}$ : Distance from node  $i$  to node  $j$  (km)
- $b_{ij}$ : Speed limit between node  $i$  and node  $j$  (km/h)
- $t_{ij}$ : Time of travel between node  $i$  and node  $j$  (h-duration)
- $p_k$ : The vehicle  $k$  with  $p_k \in P$
- $a_k$ : Volume capacity of the vehicle  $k$  ( $m^3$ )
- $m_k$ : Payload of the vehicle  $k$  (kg)
- $e_k$ : Maximum available energy capacity of the vehicle (kWh)
- $g_k$ : Running costs of vehicle  $k$  (€/km)
- $f_k$ : Fixed cost of vehicle  $k$  (€)
- $c$ : Cost for the driver (€/h)
- $r$ : Charging power at the depot (kW).

#### Variables

- $w_i^k$ : Arrival time of vehicle  $k$  at node  $i$  (h-time)
- $e_i^k$ : State of charge of vehicle  $k$  at node  $i$  (kWh)
- $h_{ij}^k$ : Energy consumed by vehicle  $k$  from node  $i$  to node  $j$  (kWh)
- $a_i^k$ : Goods' volume being transported by vehicle  $k$  at node  $i$  ( $m^3$ )
- $m_i^k$ : Goods' weight being transported by vehicle  $k$  at node  $i$  (kg)
- $x_{ij}$ : Binary variable to 1 if the arc  $(i, j)$  is travelled, 0 otherwise.

The formulation of the FSMVRPTW-EV can be expressed as the following mixed-integer program:

$$\begin{aligned} \text{Minimize } & \sum_{k \in P} \sum_{j \in C} f_k x_{0j}^k + \sum_{i \in V, i \neq j} \sum_{j \in V, i \neq j} \sum_{k \in P} d_{ij}^k x_{ij}^k g_k \\ & + \sum_{i \in V, i \neq j} \sum_{j \in V, i \neq j} \sum_{k \in P} t_{ij} x_{ij}^k c \end{aligned} \quad (4)$$

$$\text{Subject to } \sum_{j \in C} x_{0j}^k = 1, \quad \forall k \in P, \quad (5)$$

$$\sum_{i \in V, i \neq j} x_{ij}^k - \sum_{i \in V, i \neq j} x_{ji}^k = 0, \quad \forall j \in V, \forall k \in P, \quad (6)$$

$$\begin{aligned} a_k & \geq a_j^k - q_j + M_{ij} (1 - x_{ij}^k) \geq a_i^k \geq 0, \\ & \forall k \in P, \quad \forall i, j \in V, \quad i \neq j, \end{aligned} \quad (7)$$

$$\begin{aligned} m_k & \geq m_j^k - o_j + M_{ij} (1 - x_{ij}^k) \geq m_i^k \geq 0, \\ & \forall k \in P, \quad \forall i, j \in V, \quad i \neq j, \end{aligned} \quad (8)$$

$$\begin{aligned} e_k & \geq e_i^k - h_{ij}^k + M_{ij} (1 - x_{ij}^k) \geq e_j^k \geq 0, \\ & \forall k \in P, \quad \forall i, j \in V, \quad i \neq j, \end{aligned} \quad (9)$$

$$\begin{aligned} w_i^k + s_i + t_{ij} - M_{ij} (1 - x_{ij}^k) & \leq w_j^k, \\ & \forall k \in P, \quad \forall i, j \in V, \quad i \neq j, \end{aligned} \quad (10)$$

$$l_i \leq w_i^k \leq u_i, \quad \forall i \in V, \forall k \in P, \quad (11)$$

$$e_0^k \leq (1 - 0.10) * e_k, \quad \forall k \in P, \quad \forall i \in V, \quad (12)$$

$$\begin{aligned} e_0^k & \leq s_0 * r \leq (0.80 - 0.10) * e_k, \\ & \forall k \in P', \quad \forall i \in V, \end{aligned} \quad (13)$$

$$x_{ij}^k \in \{0, 1\}, \quad \forall k \in P, \quad \forall i, j \in V, \quad i \neq j. \quad (14)$$

Equation (4) represents the objective function. It expresses the total costs associated with a solution of the FSMVRPTW-EV. The first term considers the fixed costs of vehicles leaving the depot. The second term computes the running costs of the vehicles. Finally the last term considers the staff costs to operate the vehicle.

Constraints are given by (5) to (14). Constraints (5) and (6) guarantee that vehicles start from the depot, visit the customers, and come back to the depot. Constraint (6) in particular ensures the conservation of flow by forcing the equality between the number of arrivals and the number of departures at each vertex. Constraints (7) and (8) guarantee that the vehicle capacity is not exceeded in terms of volume and weight. They also track their reduction through the deliveries.  $M_{ij}$  is a sufficiently large number. Constraint (9) guarantees that the available energy is always positive and tracks the battery depletion through the route. Constraint (10) sets a minimum arrival time for vehicle  $k$  arriving at customer  $j$ . Constraint (11) ensures that customers are visited during their time windows and that vehicles are operated during the opening hours of the depot. Constraints (12) and (13) consider the maximum depletion of the battery. In particular, constraint (13) considers fast charging possibilities at the depot. Finally, constraint (14) ensures the binary integrality.

**3.4. The Algorithm.** The algorithm we developed to solve the FSMVRPTW-EV is based on the savings heuristic [34]. First, an initial solution is built with each shop being delivered by one route. Subsequently the solution is iteratively improved by searching for potential savings by merging two or more routes.

In order to address the constraints of the FSMVRPTW-EV some adjustments have been made to the original savings heuristic algorithm. When searching for potential savings, the adjusted algorithm limits the computation of potential savings to the five closest shops to the last shop inserted in the route. When comparing with an algorithm searching for savings for all shops, results are barely changed whereas computation times are reduced drastically. Moreover, as proposed by Bräysy et al. [35], the idea of the insertion-based heuristic is used. When merging an initial route (thus delivering to only one shop) with the route being improved, each possible position of the shop in the route is considered. The position showing the largest savings is selected and another initial route is investigated for merging. As a result, the shop to be inserted is the one showing the largest savings when located at the best position in that route.

Bräysy et al. [35] also recommend using an insertion sequence for customers. The algorithm is more effective when the most critical shops are investigated first (i.e., shops with short time windows). The algorithm starts to build routes around the most difficult shops to insert. If these would be inserted later, once most shops are already included in the constructed routes, there might be no possible insertion left for that shop. The algorithm would then create a single route delivering only to that critical shop which is not cost effective. The insertion sequence is therefore based on a criticality index that considers for each shop the start of the time window, the time window duration, and the distance from the depot. Shops that are inserted first are shops with a limited time window, starting early and located closer to the depot.

In order to consider the different combinations of vehicles, the algorithm uses a tree. In each branch, one of the vehicles is selected. According to the heuristic described above, a maximum of shops are inserted in the route, given the selected vehicle. The resulting node of that branch shows the number of shops that still need to be delivered. The branch is then developed further until all the shops are delivered. We have then a possible solution. Still, if the total cost of a branch becomes higher than the total cost of a completed branch, then the branch is not further explored. Finally, once the tree is fully built, the branch with the lowest cost is considered as the optimal solution.

**3.5. Instances.** Benchmark instances are common practice to compare performance of different algorithms. However, they use mainly Euclidian distances to assess distances between shops. Since speed becomes a factor influencing the range of BEVs, O-D matrices between shops in terms of distance and time are required to feed the energy model.

We generated a set of instances based on a real case in urban freight transport. Distribution occurs from an urban depot and delivers 681 shops located in the city and in the periphery early in the morning. The loading of the vehicles starts from 3 a.m. and is assumed to take 45 minutes. The operations face often tight time windows as shops prefer to receive goods before first customers arrive. The shops are therefore described in terms of time windows and demand (expressed both in volume and weight). The O-D matrices

between each shop are also given in terms of time and distance. They were generated based on the location of the shops with the Network analyst of ArcGIS. Finally, we assumed a delivery time of 3 minutes at each shop. Out of these 681 shops, we selected randomly a set of 25, 10, and 5 shops in order to keep reasonable computation times in our analyses.

The generation of instances considered also different set of vehicles. They are based on 10 different vehicles that represent the different vehicle types used in urban freight transport. We consider the segments of the quadricycles (type A), small vans (type B), large vans (type C), and trucks (type D). For each segment, different technologies are represented. The segment of quadricycles considers the diesel Aixam Mega Multitruck (A-d) and the electric Goupil G3 (A-ev). The small van segment uses the electric, petrol, and diesel versions of the Renault Kangoo Express (B-ev, B-p, and B-d). The large van segment is represented by the diesel Mercedes Sprinter (C-d) and the electric Smith Edison (C-ev). Finally, the truck segment uses a diesel and hybrid versions of the Fuso Canter 7.5 tonnes (D-d, D-h). The electric Smith Newton is also considered in that segment (D-ev). The generation of instances considered therefore 7 different sets of vehicles: type A (2 vehicles), type B (3 vehicles), type C (2 vehicles), type D (3 vehicles), BEV only (4 vehicles), Diesel only (4 vehicles), and all vehicles (10 vehicles).

By combining the different sets of vehicles with the different sets of shops, we get a sample of 21 instances to test our algorithm. They are available at the following url: <http://mamca.be/plebeau/FSMVRPTW-EV>.

## 4. Results

The FSMVRPTW-EV was applied on the 21 instances described above. We used for that a desktop computer with a processor Intel Core i7-2640M and an installed memory of 8 GB. The results of the instances give the total cost and the total distance of the routes. They give also the vehicles that were identified by the FSMVRPTW-EV to achieve the deliveries at a minimal cost. Finally, the computing times to solve the instances are also measured. Results are summarised in Table 2 considering a constant temperature of 15 degrees Celsius.

**4.1. Algorithm Performance.** In terms of computation time, results show that the performance of the algorithm is sensitive to the number of vehicles considered and the number of shops to be delivered. They both increase the number of route combinations that need to be explored in the tree: as the number of shops increases, more vehicles are needed to achieve the distribution and more vehicle combinations are possible.

To a lower extent, complexity of the problems increases also with the capacity of the vehicles considered: the search of the optimal route requires more computation resources to order shops in the route.

**4.2. Vehicle Classes.** When analysing the vehicles classes, Table 2 shows first that the fleet of vehicles cannot be

TABLE 2: Results of the FSMVRPTW-EV.

Number of shops	Vehicle set	Computing time (sec)	Total cost (€)	Total distance (km)	Vehicles selected
5	Quadricycles (A-ev, A-d)	—	—	—	—
	Small vans (B-ev, B-d, and B-p)	76	133.24	104.67	B-ev1, B-ev1'
	Large van (C-ev, C-d)	32	103.51	77.88	C-d1
	Truck (D-ev, D-d, and D-h)	48	112.77	77.88	D-h1
	Diesel only (A-d, B-d, C-d, and D-d)	56	103.51	77.88	C-d1
	Electric only (A-ev, B-ev, C-ev, and D-ev)	54	116.45	77.88	C-ev1
	All vehicles (A-ev, A-d, B-ev, B-d, B-p, C-ev, C-d, D-ev, D-d, and D-h)	204	103.51	77.88	C-d1
10	Quadricycles (A-ev, A-d)	—	—	—	—
	Small vans (B-ev, B-d, and B-p)	291	224.2	164.68	B-ev1, B-ev2, and B-ev1'
	Large van (C-ev, C-d)	195	210.17	150.28	C-d1, C-d2
	Truck (D-ev, D-d, and D-h)	483	159.04	123.66	D-h1
	Diesel only (A-d, B-d, C-d, and D-d)	515	168.43	123.66	D-d1
	Electric only (A-ev, B-ev, C-ev, and D-ev)	476	174.47	123.66	D-ev1
	All vehicles (A-ev, A-d, B-ev, B-d, B-p, C-ev, C-d, D-ev, D-d, and D-h)	1630	159.04	123.66	D-h1
25	Quadricycles (A-ev, A-d)	—	—	—	—
	Small vans (B-ev, B-d, and B-p)	3964	389.28	251.31	B-ev1, B-ev2, B-ev3, B-ev4, and B-ev1'
	Large van (C-ev, C-d)	2160	333.97	209.12	C-d1, C-d2, and C-d3
	Truck (D-ev, D-d, and D-h)	5476	309.67	217.28	D-h1, D-h2
	Diesel only (A-d, B-d, C-d, and D-d)	13066	307.22	226.36	D-d1, B-d1
	Electric only (A-ev, B-ev, C-ev, and D-ev)	11235	291.59	204.63	D-ev1, A-ev1
	All vehicles (A-ev, A-d, B-ev, B-d, B-p, C-ev, C-d, D-ev, D-d, and D-h)	140380	285.99	217.28	D-h1, B-ev1

Source: own setup.

limited to quadricycles as no solutions are found for that class of vehicles. The model does not consider indeed split deliveries: a customer receives one and only one delivery. As a result, some customers have a freight demand that cannot be transported by quadricycles. According to our FSMVRPTW-EV, the potential of quadricycles lies therefore as a complementary vehicle in the mix fleet.

The same conclusion could be drawn for the segment of small vans. When fleet is limited to that class of vehicles, more routes need to be operated because of the limited payload or volume capacity. As a result, distances and costs are more important than in the other vehicle segments. The difference with the quadricycles is that using quadricycles only is not feasible on the instances considered. Using small vans only is feasible but not optimal on the instances considered. Small vans are therefore interesting as a complementary vehicle in the mix fleet (i.e., to deliver specific shops with shorter time windows). The instance with twenty-five shops illustrates this as a small van is selected among all vehicles in the optimal solution: the truck is delivering a maximum of shops and a small van has a capacity large enough to deliver the customers that could not be delivered by the truck. This organisation is reflected on the same instance when we consider only electric

vehicles: in that case, a quadricycles is used to deliver the last shops.

The segment of trucks registers most of the time the delivery route with the total minimum distance driven. Their higher capacity requires indeed less vehicles to serve all the customers. However, they are not always selected in the optimal solutions as they have higher costs. In the instances with five shops, the demand is low enough to deliver all customers with a smaller vehicle and a large van. When considering a fleet with only trucks, we can see that they operate the same routing plan than the van. Since the important capacity of the truck is not required, the optimal solution selects the large van. On the other hand, in the instances with ten shops, the truck is selected in the optimal solution. Since demand has increased, the payload of the large van is too limited now to deliver all the customers in one route. Instead, two large vans are used to satisfy the demand while only one truck is required to deliver all the goods. As time windows are large enough to deliver all the shops in one route, the truck is identified to be the best vehicle to use.

4.3. *Vehicle Technology.* As Table 2 shows, the optimal technology varies across instances. In the small instance with

five shops, we can see that diesel is preferred. When routing requires a large van to deliver the shops, diesel will be more likely selected over the electric vehicles. Indeed, Lebeau et al. [36] showed that electric vehicles could less compete with diesels in the segment of large vans. Still, the delivery is feasible with a large electric van. The routing plan requires about 25 kWh while the energy capacity of the vehicle is 40 kWh. But it was not selected in the optimal solution as delivering with the large electric van would have entailed distribution with an added cost of 12.5% compared to the optimal solution.

In the larger instance with ten shops, diesel is not selected anymore as the optimal technology. We saw that trucks are more suited for the deliveries given the higher demand. However, in that segment, the hybrid truck is always preferred over the diesel truck by the FSMVRPTW-EV since fixed costs and running costs are lower. Indeed, lower maintenance costs and higher savings from deductibility on taxable profits contribute to lowering fixed costs of the hybrid truck compared to the diesel truck. As a result, hybrid truck is selected most of the time to be the vehicle operating the deliveries at a minimal cost. Let us note that the delivery is also feasible with the electric truck as the energy required to operate that route is estimated to be around 56 kWh while battery capacity is 80 kWh. Hence, limited battery is not a constraint on the operations of the electric truck. But delivering with an electric truck has higher costs and is therefore not selected as the optimal solution. Still, the added cost of delivering with an electric vehicle appears to be lower than in the van segment. The cost of delivering with an electric truck is around 10% higher than delivering with the hybrid truck.

In the largest instance with twenty-five shops, we can see that battery electric vehicles are now part of the optimal solution. Shops are delivered by a hybrid truck and an electric small van. Since the electric small van needs to cover a lower distance than in other vehicle segments to be competitive with diesel van, it is most often preferred over the diesel. For the comparison, delivering the twenty-five shops with a diesel only fleet would require an added cost of 7.5%. On the other hand, delivering the twenty shops with a fleet made of only BEV would require an added cost of less than 2%.

## 5. Conclusions

This paper presents a fleet size and mix vehicle routing problem with time windows for electric vehicles (FSMVRPTW-EV). The main contribution of the authors is considering the variability of range of electric vehicles. Based on real observations, an energy consumption model was developed and integrated in the FSMVRPTW-EV. It is then applied on 21 instances generated from a case in urban freight transport.

The results show that a fleet with different technologies reduces costs of distribution. Indeed, in the segments of quadricycles and small vans, electric vehicles are often the most competitive technology. However, in the segment of large vans, diesel remains the most interesting solution from a financial point of view as electric vehicles would need to cover a very important distance to be cost competitive.

Finally, hybrid vehicle is mostly chosen in the segment of trucks as its running costs and fixed costs are lower than the diesel truck. It benefits indeed of higher savings from deductibility on taxable profits and lower maintenance costs. As a result, technology depends especially on the vehicles class required by distribution. When considering the small instance of five shops, one van offers a sufficient capacity to deliver all the shops. Hence, diesel is preferred. When considering the medium instance with ten shops, hybrid vehicle is preferred since one truck is required to deliver the shops with a minimum of vehicles. Finally, in the case of the large instance with twenty-five shops, hybrid and electric vehicles are selected in the optimal set of vehicles as one truck and one small van offer the sufficient capacity to deliver all the shops.

Given the paradox of the electric vehicles, we have seen in our results that electric vehicles are mostly affected by the lower distance bound. Operating a fleet with only electric vehicles fleet implies often higher costs. However, they are barely affected by the upper distance bound since a feasible solution has always been found for instances with only electric vehicles. According to our results, the limited range of electric vehicles is therefore compatible with urban distribution.

Hence, this paper demonstrates the feasibility and the economic relevance of introducing electric vehicles in urban distribution. The vehicle routing problem allows identifying the vehicles that are most adapted to meet customers' requirements. Still, further research should be conducted on the efficiency of the algorithm in order to solve larger problems and meet the needs of daily practice. Also, the energy model could be refined by considering observations on a larger set of electric vehicles.

## Conflict of Interests

The authors declare that there is no conflict of interests regarding the publication of this paper.

## Acknowledgments

The authors would like to thank Innoviris (the institution in the Brussels-Capital Region encouraging scientific research and innovation) for their financial support. This research was performed in the framework of a Prospective Research for Brussels entitled "A strategy for the implementation of a sustainable logistics concept for the city distribution of the Brussels-Capital Region."

## References

- [1] L. Dablanc and D. Rakotonarivo, "The impacts of logistics sprawl: how does the location of parcel transport terminals affect the energy efficiency of goods movements in Paris and what can we do about it?" *Procedia—Social and Behavioral Sciences*, vol. 2, pp. 6087–6096, 2010.
- [2] S. Anderson, J. Allen, and M. Browne, "Urban logistics—how can it meet policy makers' sustainability objectives?" *Journal of Transport Geography*, vol. 13, no. 1, pp. 71–81, 2005.

- [3] F. Russo and A. Comi, "City characteristics and urban goods movements: a way to environmental transportation system in a sustainable city," *Procedia—Social and Behavioral Sciences*, vol. 39, pp. 61–73, 2012.
- [4] E. Ségalou, J. Routhier, C. de Rham, and A. Albergel, *Mise en place d'une méthodologie pour un bilan environnemental physique du transport de marchandises en ville*, ADEME, Paris, France, 2006.
- [5] L. Dablanc, "City distribution, a key element of the urban economy: guidelines for practitioners," in *City Distribution and Urban Freight Transport: Multiple Perspectives*, C. Macharis and S. Melo, Eds., pp. 13–36, Edward Elgar, Cheltenham, UK, 2011.
- [6] J. Schoemaker, J. Allen, M. Huschebeck, and J. Monigl, *Quantification of Urban Freight Transport Effects I*, 2006.
- [7] European Commission, *White paper: Roadmap to a Single European Transport Area*, European Commission, Brussels, Belgium, 2011.
- [8] H. Quak, "Urban freight transport: the challenge of sustainability," in *City Distribution and Urban Freight Transport: Multiple Perspectives*, C. Macharis and S. Melo, Eds., pp. 37–55, Edward Elgar, Cheltenham, UK, 2011.
- [9] T. G. Crainic, N. Ricciardi, and G. Storchi, "Advanced freight transportation systems for congested urban areas," *Transportation Research Part C: Emerging Technologies*, vol. 12, no. 2, pp. 119–137, 2004.
- [10] M. Messagie, F. Boureima, J. Matheys et al., "Environmental performance of a battery electric vehicle: a descriptive Life Cycle Assessment approach," *World Electric Vehicle Journal*, vol. 4, no. 1, pp. 782–786, 2010.
- [11] M. Schneider, A. Stenger, and D. Goetze, "The electric vehicle-routing problem with time windows and recharging stations," *Transportation Science*, vol. 48, no. 4, pp. 500–520, 2014.
- [12] B. Van Amburg and W. Pitkanen, "Best fleet uses, key challenges and the early business case for E-Trucks: findings and recommendations of the E-Truck Task Force," in *World Electric Vehicle Symposium and Exhibition (EVS '12)*, pp. 1–12, Los Angeles, Calif, USA, May 2012.
- [13] P. Toth and D. Vigo, "Models, relaxations and exact approaches for the capacitated vehicle routing problem," *Discrete Applied Mathematics*, vol. 123, no. 1–3, pp. 487–512, 2002.
- [14] G. B. Dantzig and J. H. Ramser, "The truck dispatching problem," *Management Science*, vol. 6, no. 1, pp. 80–91, 1959.
- [15] N. Christofides, A. Mingozzi, and P. Toth, "Exact algorithms for the vehicle routing problem, based on spanning tree and shortest path relaxations," *Mathematical Programming*, vol. 20, no. 3, pp. 255–282, 1981.
- [16] G. Laporte, Y. Nobert, and M. Desrochers, "Two exact algorithms for the distance constrained vehicle routing problem," Cah. du GERAD G-82-05, 1982.
- [17] G. Laporte, Y. Nobert, and M. Desrochers, "Optimal routing under capacity and distance restrictions," *Operations Research*, vol. 33, no. 5, pp. 1050–1073, 1985.
- [18] G. Laporte, Y. Nobert, and S. Taillefer, "A branch-and-bound algorithm for the asymmetrical distance-constrained vehicle routing problem," *Mathematical Modelling*, vol. 9, no. 12, pp. 857–868, 1987.
- [19] F. Gonçalves, S. R. Cardoso, S. Relevas, and A. P. F. D. Barbosa-Póvoa, "Optimization of a distribution network using electric vehicles: a VRP problem," in *15 Congresso da associação Portuguesa de Investigação Operacional*, Lisboa, Portugal, 2011.
- [20] S. Erdoğan and E. Miller-Hooks, "A green vehicle routing problem," *Transportation Research E: Logistics and Transportation Review*, vol. 48, no. 1, pp. 100–114, 2012.
- [21] J. F. Bard, L. Huang, M. Dror, and P. Jaillet, "A branch and cut algorithm for the VRP with satellite facilities," *IIE Transactions (Institute of Industrial Engineers)*, vol. 30, no. 9, pp. 821–834, 1998.
- [22] R. G. Conrad and M. A. Figliozzi, "The recharging vehicle routing problem," in *Proceedings of the 61st Annual Conference and Expo of the Institute of Industrial Engineers*, T. Doolen and E. van Aken, Eds., May 2011.
- [23] C. Lin, K. L. Choy, G. T. S. Ho, S. H. Chung, and H. Y. Lam, "Survey of green vehicle routing problem: past and future trends," *Expert Systems with Applications*, vol. 3, no. 4, part 1, pp. 1118–1138, 2014.
- [24] J. H. R. van Duin, L. A. Tavasszy, and H. J. Quak, "Towards E (lectric)—urban freight: first promising steps in the electric vehicle revolution," *European Transport*, vol. 54, pp. 1–19, 2013.
- [25] G. Hiermann, J. Puchinger, and R. F. Hartl, "The electric fleet size and mix vehicle routing problem with time windows and recharging stations," *Transportation Science*. In press.
- [26] J. G. Hayes, R. P. R. de Oliveira, S. Vaughan, and M. G. Egan, "Simplified electric vehicle power train models and range estimation," in *Proceedings of the 7th IEEE Vehicle Power and Propulsion Conference (VPPC '11)*, pp. 1–5, Chicago, Ill, USA, September 2011.
- [27] S. Blanco, "2013 Nissan Leaf gets 75-mile range (actually 84) in new EPA test [WWW Document]," *Autobloggreen*, 2013, <http://green.autoblog.com/2013/02/21/2013-nissan-leaf-revealed-gets-75-mile-range-actually-84-in-n>.
- [28] P. Crowe, *European-Specific Nissan Leaf to Be Unveiled in Geneva*, Hybrid Cars, 2013, <http://www.hybridcars.com/european-specific-nissan-leaf-to-be-unveiled-in-geneva/>.
- [29] A. Afroditi, M. Boile, S. Theofanis, E. Sdoukopoulos, and D. Margaritis, "Electric vehicle routing problem with industry constraints: trends and insights for future research," *Transportation Research Procedia*, vol. 3, pp. 452–459, 2014.
- [30] D. Goetze and M. Schneider, *Routing a Mixed Fleet of Electric and Conventional Vehicles*, 2014.
- [31] M. El Baghdadi, L. De Vroey, T. Coosemans, J. Van Mierlo, W. Foubert, and R. Jahn, "Electric vehicle performance and consumption evaluation," in *World Electric Vehicle Symposium and Exhibition (EVS '13)*, pp. 1–8, Barcelona, Spain, November 2013.
- [32] L. De Vroey, R. Jahn, M. El Baghdadi, and J. Van Mierlo, "Plug-to-wheel energy balance-results of a two years experience behind the wheel of electric vehicles," in *World Electric Vehicle Symposium and Exhibition (EVS '13)*, pp. 1–5, Barcelona, Spain, November 2013.
- [33] P. Belfiore and H. T. Y. Yoshizaki, "Heuristic methods for the fleet size and mix vehicle routing problem with time windows and split deliveries," *Computers & Industrial Engineering*, vol. 64, no. 2, pp. 589–601, 2013.
- [34] G. Clarke and J. W. Wright, "Scheduling of vehicles from a central depot to a number of delivery points," *Operations Research*, vol. 12, no. 4, pp. 568–581, 1964.

- [35] O. Bräysy, W. Dullaert, G. Hasle, D. Mester, and M. Gendreau, "An effective multirestart deterministic annealing metaheuristic for the fleet size and mix vehicle-routing problem with time windows," *Transportation Science*, vol. 42, no. 3, pp. 371–386, 2008.
- [36] P. Lebeau, C. Macharis, J. Van Mierlo, and K. Lebeau, "Electric vehicles for logistics: a total cost of ownership analysis," in *Proceedings of the BIVEC-GIBET Transport Research Days*, M. Hesse, G. Caruso, P. Gerber, and F. Viti, Eds., pp. 307–318, Walferdange, Luxembourg, 2013.

## Research Article

# Charging Guidance of Electric Taxis Based on Adaptive Particle Swarm Optimization

Liyong Niu and Di Zhang

National Active Distribution Network Technology Research Center, Beijing Jiaotong University, Beijing 100044, China

Correspondence should be addressed to Liyong Niu; lyniu@bjtu.edu.cn

Received 16 September 2014; Revised 6 December 2014; Accepted 2 January 2015

Academic Editor: Suleiman M. Sharkh

Copyright © 2015 L. Niu and D. Zhang. This is an open access article distributed under the Creative Commons Attribution License, which permits unrestricted use, distribution, and reproduction in any medium, provided the original work is properly cited.

Electric taxis are playing an important role in the application of electric vehicles. The actual operational data of electric taxis in Shenzhen, China, is analyzed, and, in allusion to the unbalanced time availability of the charging station equipment, the electric taxis charging guidance system is proposed basing on the charging station information and vehicle information. An electric taxis charging guidance model is established and guides the charging based on the positions of taxis and charging stations with adaptive mutation particle swarm optimization. The simulation is based on the actual data of Shenzhen charging stations, and the results show that electric taxis can be evenly distributed to the appropriate charging stations according to the charging pile numbers in charging stations after the charging guidance. The even distribution among the charging stations in the area will be achieved and the utilization of charging equipment will be improved, so the proposed charging guidance method is verified to be feasible. The improved utilization of charging equipment can save public charging infrastructure resources greatly.

## 1. Introduction

In the past forty years, global electric vehicle (EV) technology has gained advancement tremendously [1, 2]. In the last five years, commercial operations of pure electric taxis (E-taxis) have successively begun in Chinese cities such as Beijing, Hangzhou, and Shenzhen, and more than 2,500 E-taxis in total are now in operation. From 2011 to June 2014, a total of 830 E-taxis have been put into operation in Shenzhen. There are now 50 charging stations that can provide charging services to E-taxis, and 648 charging machines/piles are in operation. The operators of these charging stations have established a citywide data monitoring system, which monitors and records operation data of all E-taxis and charging devices in real time.

The usage conditions of charging devices at 15 charging stations in Shenzhen have been surveyed, and charging data of these charging stations in a month were analyzed. To compare the usage rates of the charging devices, the time

usage rate (TUR) of the charging devices in a charging station can be defined as follows:

$$\eta = \frac{1}{m} \sum_{j=1}^m \left( \frac{1}{Z} \sum_{i=1}^n (E_i - S_i) \right), \quad (1)$$

where  $\eta$  = TUR of the charging devices in a charging station;  $m$  = number of charging devices;  $n$  = daily charging frequency of the  $j$ th device;  $E_i$  = end time of the  $i$ th charging in minute,  $E_i \in [0, 1440)$ ;  $S_i$  = starting time of the  $i$ th charging in minute,  $S_i \in [0, 1440)$ ;  $Z$  = total time of a day in minute; that is,  $Z = 1,440$  min.

The TURs of the 15 surveyed charging stations were distributed extremely unevenly (Figure 1). The TURs of several charging stations were relatively high, such that E-taxis had to wait in a queue during a certain period. However, the TURs of other charging stations were relatively low, such that the charging devices were idle for a relatively long time.

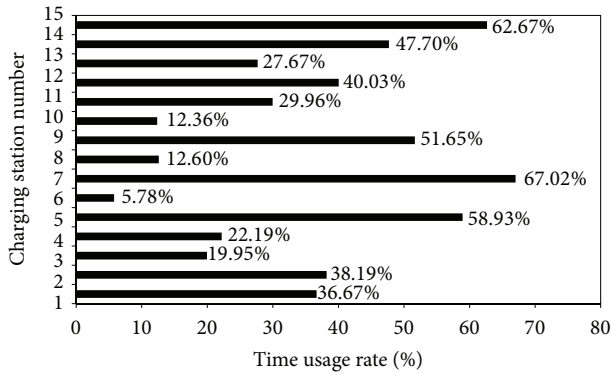


FIGURE 1: TURs of charging stations in Shenzhen, China.

Therefore, it is necessary to establish an effective system to assist in charging E-taxis more efficiently.

This paper presents the basic framework of a charging guidance system (CGS) for E-taxis, which is based on the data monitoring platform of the charging service network of Shenzhen. And a charging guidance model (CGM) with the adaptive particle swarm optimization (APSO) algorithm is proposed. The correctness of the model and the algorithm is verified through simulation.

## 2. Related Works

In recent years, the multispect impacts from connecting a large number of EVs to power grids have become a sustained research focus [2] and coordinated EV charging is the emphasis of the current research [3–10].

In [3], the effect of multiple plug-in hybrid electric vehicles (PHEVs) in a coordinated charging mode on the power distribution network of a residential area was discussed, and a stochastic programming algorithm was proposed. In [4], an admission control mechanism for PHEV charging demand was proposed based on a substation monitoring system. In [5], it was proposed that the EV charging load could be adjusted both temporally and spatially, and it was hypothesized that load scheduling could be performed on a temporal-spatial double scale such that EV charging load could have a positive effect on power grid operation. However, the full load power curve was adjusted only by changing the beginning charging time; spatial charging load scheduling was not realized. In [6], a k-nearest neighbor (KNN) classification algorithm that could predict future charging rates was proposed to select time intervals with low charging rates for PHEVs. In [7], a particle swarm algorithm was used to optimize the charge and discharge control strategy for participating individual EVs in load response. In [8], a multiobjective optimization method was used to improve the mathematical model of a charging scheduling strategy, which solved the problem of poor performance of the charging scheduling strategy in filling the “lowest valley” in a single-objective optimization. In [9], a real-time electricity price-based CGS for EVs was proposed, which could be used to regulate the distribution of EVs at each charging station to improve the voltage quality of the power

distribution network. In [10], cost-benefit analysis models for EV discharging users and electric power enterprises were established to calculate the costs and benefits of realizing peak load shifting during peak discharging after the EVs of all parties were integrated into the power grid, which was extremely vital in guiding the EV charging.

The aforementioned studies and other studies have focused on private EVs, their effect on power grids, and coordinated charging guidance strategies. In fact, the effect of public EVs (e.g., buses and taxis) on power grids is more important because these vehicles continuously provide public services and consume more electricity. The charging characteristics of public EVs (E-taxis in particular) are far more complicated than those of private EVs due to their complicated mobility characteristics and a greater number of charging options [11]. There have been few studies that have investigated the charging scheduling of E-taxis. In [11, 12], according to the charging characteristics of PHEV taxis, a backward induction optimization algorithm to select charging time slots was proposed based on the time-of-use (TOU) electricity price and additional charging fees. In [13], a scheduling strategy for a taxi fleet, which included charging plans, was proposed based on clients’ demands of taxi reservations to reduce the effect of the charging time and battery swapping on the operational time and revenue.

This paper presents a new viewpoint to enhance the usage rates of large-scale charging devices constructed specially for E-taxis within a city range. The presented research work is based on the collected actual operation data and the presented CGS, CGM, and algorithm are based on the quasi real-time operation data, which makes the presented work different from former research work, having much more practical value.

## 3. CGS Framework

Figure 2 shows the CGS framework for E-taxis charging. By collecting processed information regarding the charging stations (e.g., number and locations of the remaining charging piles) and information regarding E-taxis (e.g., residual capacities of battery packs (SOC) and locations), the control system helps drivers make charging decisions using a smart optimization algorithm when the constraint conditions are met, that is, guides E-taxis to appropriate charging stations.

The CGS sends charging guidance information to each E-taxi in real time at a certain time interval, and E-taxi drivers decide whether or not to respond to such information based on the actual situation. In this way, E-taxis can receive optimized charging guidance when charging is required.

## 4. Charging Guidance Optimization Model

**4.1. Model Assumptions.** When E-taxi drivers select a charging station, they primarily consider factors such as time (including travel time to the charging station, waiting time at the station, and charging time), travel distance, traffic conditions, and charging fees. However, it is expected that the number of E-taxis at each charging station is correlated with the capacity of the charging station to increase the

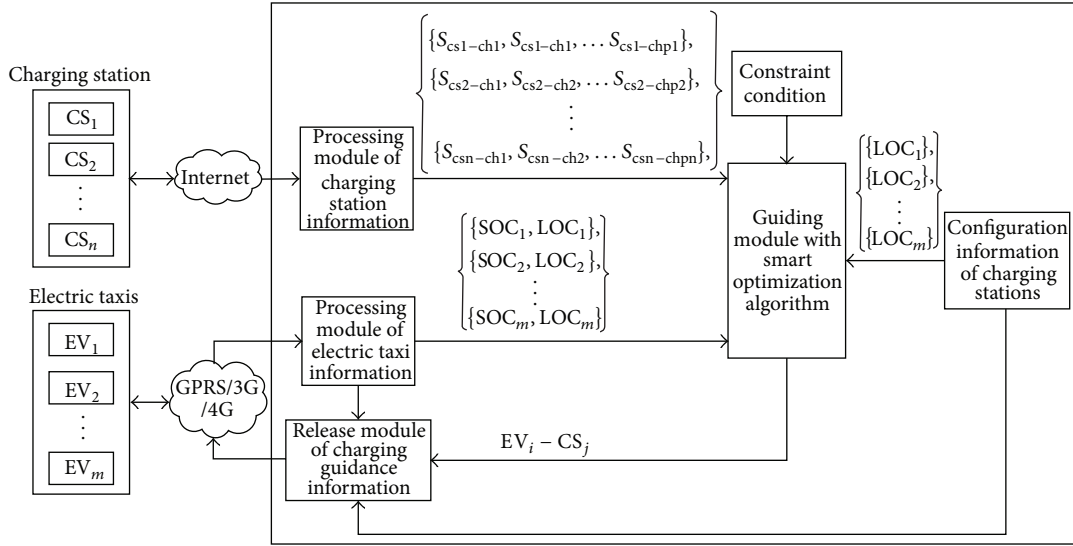


FIGURE 2: Framework of CGS.

comprehensive usage rate of charging facilities and avoid queuing and resource waste, such as idling charging devices. So, E-taxis' charging is guided optimally as described below.

Under the premise that the calculation of the objective function will not be affected, the following assumptions are made.

- (1) Within a given region, the number of charging stations ( $N$ ) and the number of E-taxis ( $M$ ) are known.
- (2) Within an infinitesimal amount of time ( $\Delta t$ ), E-taxi drivers can only select one charging station. The flag variable for E-taxi charging is set as  $x_{ij}$ , and the value of which is either 0 or 1. When  $x_{ij} = 0$ , the  $i$ th E-taxi is not charged at the  $j$ th charging station and when  $x_{ij} = 1$ , the  $i$ th E-taxi is charged at the  $j$ th charging station.
- (3) The impact of traffic conditions is not considered. E-taxis are driven at a uniform speed ( $v_i$ ).
- (4) When the number of E-taxis waiting to be charged is greater than the number of charging piles at the charging station, some E-taxis have to wait. Therefore, the time required for the  $i$ th E-taxi to reach the  $j$ th charging station and complete charging is  $t_{ij}$ , which is the sum of travel time to the  $j$ th charging station  $t_j^S$ , waiting time at the  $j$ th charging station  $t_j^W$ , and charging time  $t_j^C$ .
- (5) Waiting time at a charging station is negative linearly correlated with its scale. As the charging station scale increases, the waiting time decreases. Waiting coefficient  $\delta_j$  is introduced and set as  $\delta_j = 1 - 0.2G_j$ , where  $G_j \in \{1, 2, 3, 4\}$  stands for the charging station scale.

4.2. Objective Functions of the Model. The objective function of the model is established by two primary aspects: E-taxi drivers and charging stations within the region.

4.2.1. Aspect of E-Taxi Drivers. For an E-taxi driver, selecting a charging station depends primarily on three aspects: the shortest time, the shortest travel distance, and the lowest charging fees. At the current stage, charging price is fixed. Therefore, time cost and travel distance cost are the primary factors that are considered.

For the time cost, the time required for the  $i$ th E-taxi to reach the  $j$ th charging station and complete charging is defined as  $t_{ij}$ :

$$t_{ij} = \delta_j \sum_{i=1}^M x_{ij} + \frac{l_{ij}}{v_i} + t_j^C, \quad (2)$$

where  $l_{ij}$  represents the distance that the  $i$ th E-taxi traveled to reach the  $j$ th charging station in km.

When an E-taxi driver uses charging time  $t_{ij}$  as the basic objective to select a charging station, there is a precedence relationship  $\omega_{ij}$  between a specific  $t_{ij}$  value and the minimum value  $t_{ij}^{\min}$  in set  $T$ , which includes all the possible charging times:

$$\omega_{ij} = \frac{t_{ij}}{t_{ij}^{\min}}. \quad (3)$$

The smaller the value of  $\omega_{ij}$ , the greater the possibility for a driver to select this charging station.

For travel distance cost, the distance that an E-taxi travels to reach charging station  $l_{ij}$  is used as the basic objective to select a charging station. There is a precedence relationship  $\sigma_{ij}$  between a specific  $l_{ij}$  value and the minimum value  $l_{ij}^{\min}$  in set  $L$ , which includes all the possible distances:

$$\sigma_{ij} = \frac{l_{ij}}{l_{ij}^{\min}}. \quad (4)$$

The smaller the value of  $\sigma_{ij}$ , the greater the possibility for a driver to select this charging station.

The objective function is established from the aforementioned two aspects:

$$F_1 = \min \sum_{j=1}^N \sum_{i=1}^M [x_{ij} (\omega_{ij} + \sigma_{ij})]. \quad (5)$$

**4.2.2. Aspect of Charging Station Operators.** As can be concluded from the analysis of TUR of charging stations, comprehensive efficiencies of the charging devices are not evenly distributed in the overall service network of charging stations. This uneven distribution means that drivers who are waiting to be charged select the same charging station as the other drivers, which not only reduces the TURs of the charging devices but also negatively impacts the overall development of the charging stations. From the perspective of charging station operators, when E-taxis are distributed based on the scale of the charging stations using the TURs of charging facilities as the objective function is the best. More E-taxis are distributed to large-scale charging stations, and fewer E-taxis are distributed to small-scale charging stations. This demand-based distribution method lowers the fluctuation of the charging load of each charging station and balances the usage rates of the charging piles at the charging stations. Its objective function is the following:

$$F_2 = \min \sum_{j=1}^N \left( \sum_{i=1}^M x_{ij} P_i - \frac{C_j}{\sum_{j=1}^N C_j} \sum_{i=1}^M P_i \right)^2, \quad (6)$$

where  $P_i$  represents the charging power of the  $i$ th E-taxi in kW and  $C_j$  represents the number of charging piles at the  $j$ th charging station.

**4.2.3. Normalization of the Objective Functions.** Two objective functions are obtained from the analyses of the two different aspects. Therefore, it is necessary to normalize these objective functions and convert the multiobjective optimization problem into a single-objective optimization problem. The linear weighted sum method is used to convert the objective functions.

Due to the different dimensions of these two objectives, a normalized treatment is necessary for each objective function, as shown in the following equation:

$$F = \min \left( \lambda_1 \frac{F_1}{F_{1\max}} + \lambda_2 \frac{F_2}{F_{2\max}} \right), \quad (7)$$

where  $F_{1\max}$  and  $F_{2\max}$  represent the original objective function values before adjustment;  $\lambda_1$  and  $\lambda_2$  represent the corresponding weight coefficients of objective functions  $F_1$  and  $F_2$ , and  $\lambda_1 + \lambda_2 = 1$ .

**4.3. Constraint Conditions of the Model.** The constraint condition of the method is that the E-taxis that are waiting to be charged within the region can only select one charging station, as described in the following equation:

$$\sum_{j=1}^N x_{ij} = 1. \quad (8)$$

To ensure that E-taxis have enough electric power to reach the designated charging station for charging, the maximum distance  $l_{ij}^{\max}$  ( $x_{ij} = 1$ ) that the  $i$ th E-taxi travels to the  $j$ th charging station should be less than or equal to the maximum distance  $l_i^{\max}$  that the  $i$ th E-taxi can travel, as described in the following equation:

$$l_{ij}^{\max} \leq l_i^{\max}. \quad (9)$$

In (9),  $l_i^{\max} = L_d(\text{SOC}_i - \text{SOC}_{\text{lim}})$ , where  $\text{SOC}_{\text{lim}}$  is the lowest limitation generally set by the automaker and  $L_d$  is the average maximum driving distance after E-taxis are fully charged according to statistical analysis. Generally speaking, the energy consumption of EVs depends mainly on energy consumption factor, which is related to not only vehicle speed but also road type [14] and makes the relationship between SOC and estimated travel distance a complicated function. So, a linear function is used to simplify the estimation. Because the  $\text{SOC}_i$  is updated in time, the estimation accuracy is enough for the charging guidance. This paper sets  $\text{SOC}_{\text{lim}}$  as 20% and  $L_d$  as 300 km, respectively.

**4.4. Optimization Algorithm for the Model.** The charging guidance for an E-taxi is constrained by various conditions, such as the charging power of the charging station, usage conditions of the charging pile, and charging users' needs. Therefore, the problem is a nonlinear optimization problem with large dimensions, multivariables, and complicated constraints that cannot be solved by classical optimization algorithms, such as linear programming [15]. Here, an adaptive particle swarm optimization algorithm [16] is used.

A particle swarm optimization (PSO) algorithm obtains the optimal value of the swarm by simulating the predatory behavior of bird flocks, that is, by simulating the collective cooperation of bird flocks. The algorithm updates the locations and speeds of the particles using the following equation:

$$\begin{aligned} V_{id}^{k+1} &= \omega V_{id}^k + c_1 r_1 (P_{id}^k - X_{id}^k) + c_2 r_2 (P_{gd}^k - X_{id}^k), \\ X_{id}^{(k+1)} &= X_{id}^k + V_{id}^{(k+1)}, \end{aligned} \quad (10)$$

where  $\omega$  represents the inertia weight, which ranges between 0.1 and 0.9;  $d = 1, 2, \dots, D$  represents the dimensions;  $i = 1, 2, \dots, n$  represents the particles;  $k$  represents the current iteration number;  $V_{id}$  represents the speed of the particle  $i$  in the dimension  $d$ ;  $c_1$  and  $c_2$  are nonnegative constants, which are called acceleration factors; and  $r_1$  and  $r_2$  are random numbers between 0 and 1.

Similar to all the other global optimization algorithms (e.g., genetic algorithms), the premature convergence phenomenon is also present in the PSO algorithm [8], particularly in relatively complicated, multipeak searching problems. Regarding the inertia weight  $\omega$ , if the value of  $\omega$  is a random number between 0.5 and 1, experiments have indicated that the accuracy is greater than that of the linear decreasing strategy, and the convergence speed is also faster than that of the linear decreasing strategy [16]. Here, the value of  $\omega$  is as follows:

$$\omega = 0.5 - 0.5 \times \text{rand}. \quad (11)$$

In this paper, learning factors  $c_1$  and  $c_2$  are accelerated using the nonlinear inverse cosine;  $c_1$  is first large and then becomes small, whereas  $c_2$  is first small and then becomes large. The basic idea is that the self-history information of  $c_1$  is used as the primary reference to search the initial particle flight; the focus shifts to the information of the swarm, that is,  $c_2$  at the later stage [16]:

$$c_1 = c_{1e} + (c_{1s} - c_{1e}) \cdot \left[ 1 - \frac{\arccos(- (2k/Maxgen) + 1)}{\pi} \right],$$

$$c_2 = c_{2e} + (c_{2s} - c_{2e}) \cdot \left[ 1 - \frac{\arccos(- (2k/Maxgen) + 1)}{\pi} \right],$$
(12)

where  $c_{1s}$  and  $c_{2s}$  represent the initial values of the iteration;  $c_{1e}$  and  $c_{2e}$  represent the terminal values of iteration; and  $Maxgen$  represents the total number of iterations of the algorithm.

When we define  $f_i$  as the fitness of the  $i$ th particle (the value of the objective function), the mean fitness of the colony can be obtained using the following equation:

$$f_{avg} = \frac{1}{P_{size}} \sum_{i=1}^{P_{size}} f_i,$$
(13)

where  $P_{size}$  represents the total number of particles.

Then, the normalized scaling factor  $f$  of the particle swarm is determined using the following equation:

$$f = \begin{cases} \max\{|f_i - f_{avg}|\}, & \max\{|f_i - f_{avg}|\} > 1 \\ 1, & \text{other.} \end{cases}$$
(14)

Furthermore, the variance of the fitness of the entire swarm  $\sigma^2$  can be obtained as follows:

$$\sigma^2 = \sum_{i=1}^{sizepop} \left( \frac{f_i - f_{avg}}{f} \right)^2.$$
(15)

The extreme value of the swarm,  $g_{best}$ , which meets certain mutation conditions, is mutated according to a certain probability  $p_m$ . The calculation equation of  $p_m$  is as follows:

$$p_m = \begin{cases} \mu, & \sigma_2 < \sigma_d^2, f(g_{best}) > f_d \\ 0, & \text{other,} \end{cases}$$
(16)

where  $\mu$  is an arbitrary random number between 0.1 and 0.3; the value of  $\sigma_d^2$  is generally far less than the maximum value of  $\sigma^2$ ; and  $f_d$  represents the theoretical optimal value. The method of applying random perturbation was used for the mutation operation of  $g_{best}$ . The parameter  $g_{besti}$  is the  $i$ th dimensional value of  $g_{best}$ ;  $\beta$  is a random variable within a Gaussian (0, 1) distribution; then, the mutation of  $g_{best}$  is as follows:

$$g_{besti} = g_{besti} (1 + 0.5\beta).$$
(17)

Based on the aforementioned analyses, the corresponding solution process of the optimization algorithm can be obtained.

- (1) Initialize the locations and speeds of the particles in the particle swarm and correct the locations of the particles based on the constraint conditions.
- (2) Calculate the fitness of every particle (the value of the objective function).
- (3) Set the extreme value of each particle as the current location and set  $g_{best}$  as the location of the optimal particle in the initial swarm.
- (4) Update the speeds and corresponding locations of the particles according to (10).
- (5) Calculate the fitness of each particle in the particle swarm and update and record the optimal location of each particle and the optimal location of the swarm.
- (6) Calculate the variation of the fitness of the swarm  $\sigma^2$  according to (13), (14), and (15).
- (7) Calculate the mutation probability  $p_m$  according to (16).
- (8) Obtain a random number between 0 and 1. If this number is less than the mutation probability  $p_m$ , then execute the mutation operation described in (17) and correct the value of  $g_{best}$ .
- (9) Determine whether or not termination conditions are met. If true, terminate the calculation. If false, return to step (4).

## 5. Practical Example Simulations

**5.1. Example Settings.** In the present study, eight charging stations and the corresponding mean number of serviced E-taxis in Shenzhen were used as an example; that is,  $N = 8$ . Figure 3 shows the distribution of the charging stations. Table 1 lists the parameters of the charging stations.

The analysis results of the actual operation data show that the initial SOC values of E-taxis when they reached charging stations were normally distributed and the charging time accorded with a 1 h normal distribution. Therefore, the SOC of each E-taxi is randomly selected within a normal distribution  $N(0.5, 0.1)$  and the charging time of each E-taxi is calculated accordingly. The average charging power is 30 kW; that is,  $P_i = 30$  kW. The number of serviced E-taxis is 100; that is,  $M = 100$ , and the mean speed on urban roads is 40 km/h; that is,  $v_i = 40$  km/h. The value of the distance that an E-taxi travels to the charging station is randomly selected around the charging station.

**5.2. Solution Procedure and Simulation Parameters.** According to the charging guidance model and the solution method established in Section 4, the solution procedure of the example is given in Figure 4.

The simulation parameters of the algorithm are as follows:  $P_{size} = 20$ ,  $Maxgen = 300$ ,  $c_{1s} = 2.5$ ,  $c_{2s} = 0.5$ ,  $c_{1e} = 0.5$ , and  $c_{2e} = 2.5$ ,  $\lambda_1 = \lambda_2 = 0.5$ .

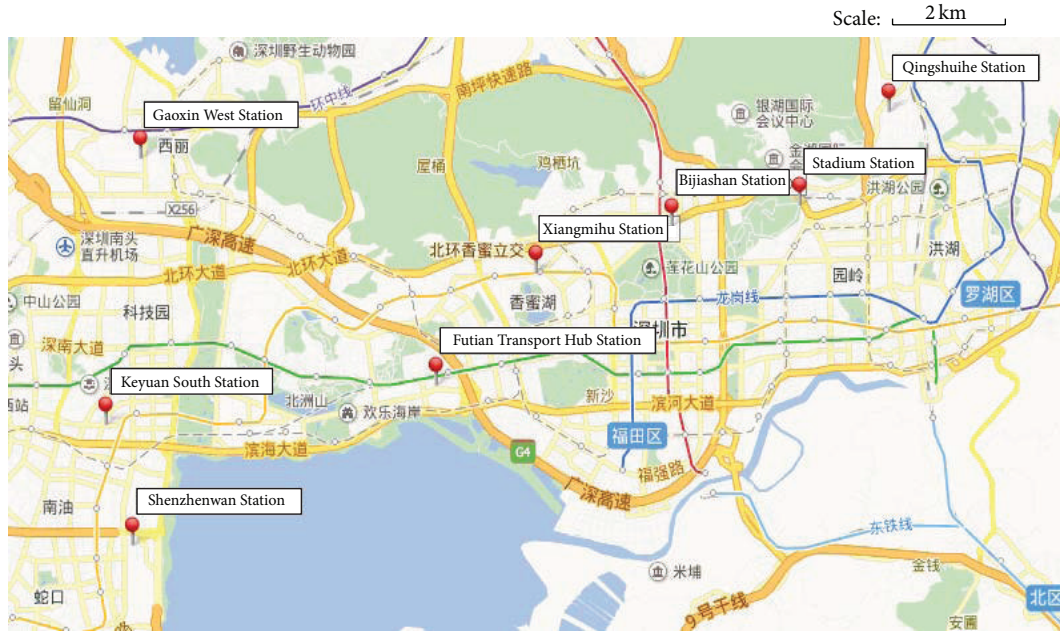


FIGURE 3: Distribution of example charging stations.

TABLE 1: Parameters of example charging stations.

Serial number	1	2	3	4	5	6	7	8
Charging stations	Xiangmihu Station	Bijjashan Station	Gaoxin West Station	Futian Transport Hub Station	Keyuan South Station	Stadium Station	Shenzhenwan Station	Qingshuihe Station
Number of charging piles	6	8	4	10	4	8	10	6
Waiting coefficient	0.6	0.4	0.8	0.2	0.8	0.4	0.2	0.6

5.3. *Simulation Results and Discussions.* The simulation outputs the flag variable matrix,  $X$ , of E-taxis. Figure 5 shows the convergence curve of the objective function. Based on the value of matrix  $X$ , the number of E-taxis that reach each charging station can be statistically analyzed as shown in Table 2. In Table 2, because Futian Transport Hub, Shenzhenwan, and Qingshuihe Stations provide service to two types of EVs actually, and the number of charging piles at these stations in the simulation is adjusted, respectively. Table 2 shows that E-taxis can be guided to appropriate charging stations by the CGS, which is based on the number of charging piles at each charging station. The optimal result solves the problem caused by E-taxi drivers' blind selection of charging stations.

In addition, according to the ratio of E-taxis charging time to the total charging time, the TURs of charging devices at Futian Transport Hub, Shenzhenwan, and Qingshuihe Stations are adjusted to 10.73%, 0.63%, and 39.98%, respectively. The comparison between the TURs before and after optimization is shown in Figure 6, which shows that an even distribution of TURs of charging devices among charging stations can be obtained by using the charging guidance method proposed in the present study.

However, E-taxis driver's benefits would be sometimes sacrificed for even distribution of TURs of charging stations. Different scenarios with varied weight coefficients are simulated to analyze the drivers' loss extent and the standard deviation of the TURs is compared correspondingly. The curve of the objective function 1 and standard deviation of TURs along with the change of weight coefficient are shown in Figure 7.

Figure 7 shows that the function value of E-taxi drivers gradually reduces with the increase of  $\lambda_1$ , while the standard deviation of TURs increases conversely. That means E-taxi drivers benefits could be really sacrificed in order to obtain an even distribution of TURs of charging devices among charging stations. However, the standard deviation of TURs falls much more slowly and tends to be stable when  $\lambda_1$  is less than 0.7, so weight coefficients can be set as  $\lambda_1 = 0.7$  and  $\lambda_2 = 0.3$  to restrict E-taxi drivers' benefits loss less than 18%. The histogram of the comparison between the TURs before and after optimization with  $\lambda_1 = 0.7$  is shown in Figure 8.

Although the even distribution of TURs of charging devices among charging stations can further sacrifice for E-taxi drivers' benefits, there will be a significant increase in the comprehensive costs of the charging service network after

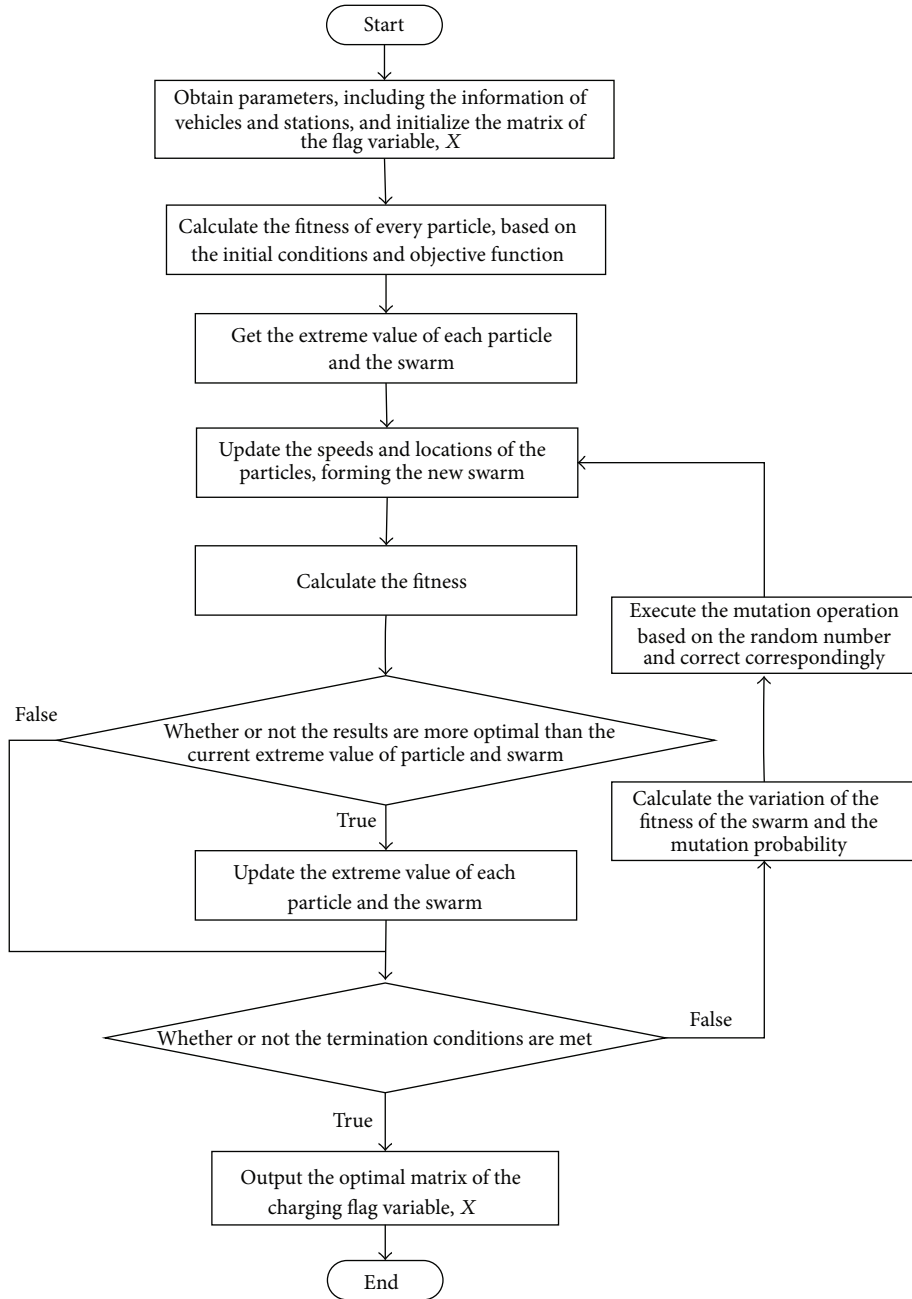


FIGURE 4: Solution procedure of the example simulation.

TABLE 2: Comparison of simulation results and actual data.

Serial number	1	2	3	4	5	6	7	8
Charging stations	Xiangmihu Station	Bijiashan Station	Gaoxin West Station	Futian Transport Hub Station	Keyuan South Station	Stadium Station	Shenzhenwan Station	Qingshuihe Station
Number of charging piles in the simulation	6	8	4	10	4	8	10	6
Number of E-taxis being charged in the simulation	10	14	6	18	7	14	19	12
Actual number of charging piles	6	8	4	19	4	8	20	8
Actual number of E-taxis being charged	24	30	4	10	9	3	2	18

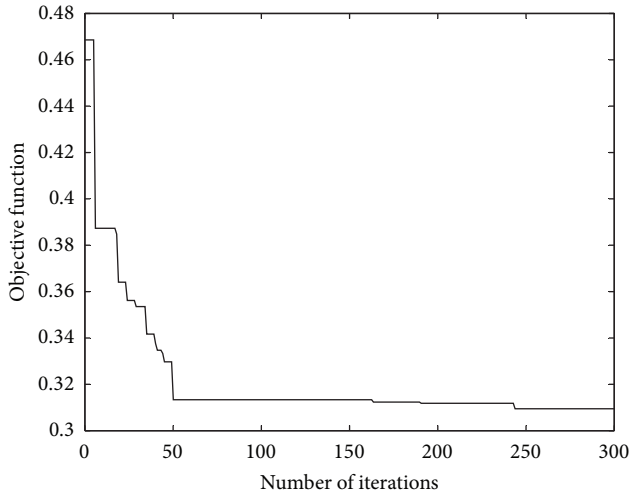


FIGURE 5: Convergence curve of the objective function.

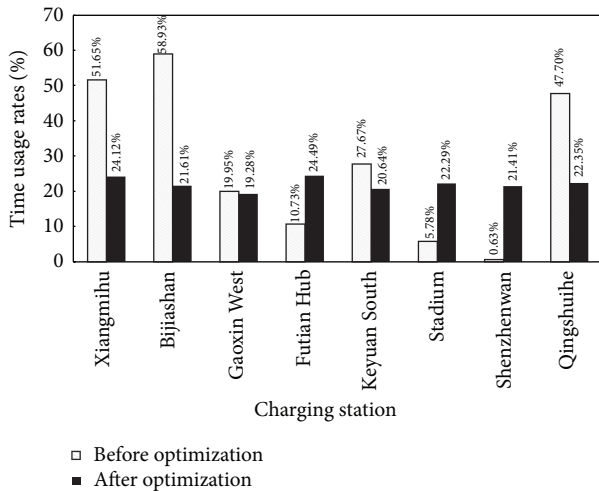


FIGURE 6: Comparison of the TURs before and after optimization.

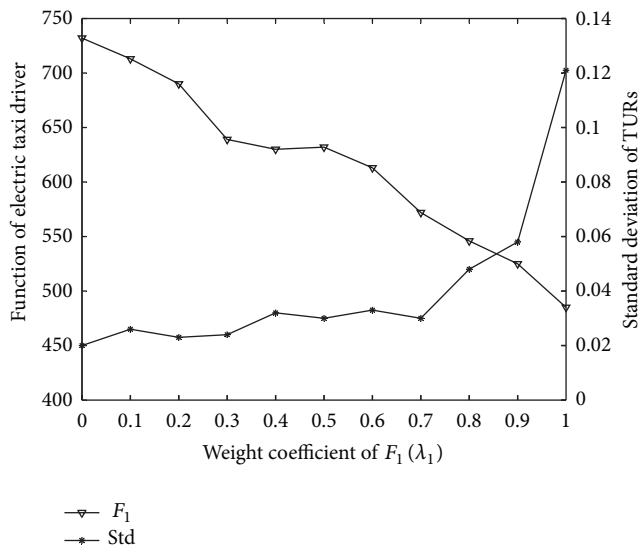


FIGURE 7: Curves of the results of objective function 1 and standard deviation of TURs.

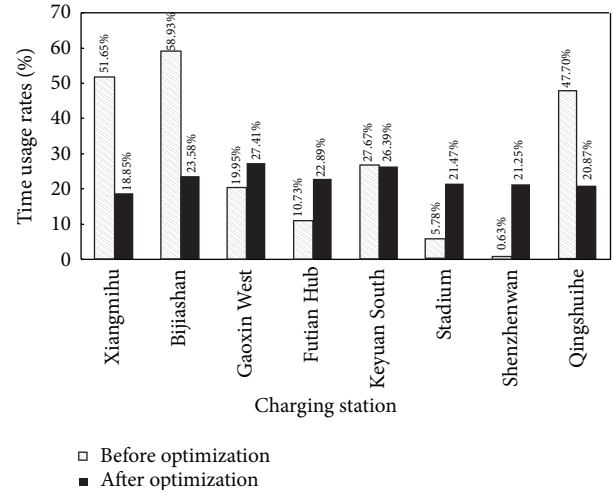


FIGURE 8: Comparison of the TURs before and after optimization with  $\lambda_1 = 0.7$ .

the E-taxi increase and both benefits will be injured. So, the benefit balance of E-taxi drivers and charging station operators can be assured in the specific range.

### 6. Conclusions

This paper proposes a method to calculate TURs of charging devices for E-taxi and conducts a statistical analysis that reveals an extremely uneven distribution of TURs among 15 charging stations in Shenzhen. Therefore, a CGS for E-taxi is proposed, which is based on the information regarding charging stations and E-taxi to solve the uneven distribution problem and improve the comprehensive benefit of charging stations. An optimization model to guide E-taxi charging is established and an APSO algorithm is used to solve the problem. Some simulations are performed based on the actual data of eight charging stations in Shenzhen.

The simulation results show that a more even distribution of TURs of charging devices among charging stations is attained by guiding E-taxi to appropriate charging stations, which verified the feasibility of the charging guidance method proposed in the present study. The benefits of E-taxi drivers and charging station operators can be balanced in the specific range. So, along with the large-scale development of E-taxi, the advantages of the proposed model will become more apparent, particularly regarding public infrastructure resource conservation.

### Conflict of Interests

The authors declare that there is no conflict of interests regarding the publication of this paper.

### Acknowledgment

This work was supported by Beijing Higher Education Young Elite Teacher Project (YETP0570). The authors contributed equally to this work and should be considered cofirst authors.

## References

- [1] C. C. Chan, "The state of the art of electric, hybrid, and fuel cell vehicles," *Proceedings of the IEEE*, vol. 95, no. 4, pp. 704–718, 2007.
- [2] C. Gao and L. Zhang, "A survey of influence of electric vehicle charging on power grid," *Power System Technology*, vol. 35, no. 2, pp. 127–131, 2011.
- [3] K. Clement, E. Haesen, and J. Driesen, "Coordinated charging of multiple plug-in hybrid electric vehicles in residential distribution grids," in *IEEE/PES Power Systems Conference and Exposition (PSCE '09)*, pp. 1–7, Seattle, Wash, USA, March 2009.
- [4] M. Erol-Kantarci, J. H. Sarker, and H. T. Mouftah, "Analysis of plug-in hybrid electrical vehicle admission control in the smart grid," in *Proceedings of the IEEE 16th International Workshop on Computer Aided Modeling and Design of Communication Links and Networks (CAMAD '11)*, pp. 56–60, IEEE, Kyoto, Japan, June 2011.
- [5] Q. Li, X. Xiao, J. Guo, and L. Liu, "Research on scheme for ordered charging of electric vehicles," *Power System Technology*, vol. 36, no. 12, pp. 32–38, 2012.
- [6] M. Erol-Kantarci and H. T. Mouftah, "Prediction-based charging of PHEVs from the smart grid with dynamic pricing," in *Proceedings of the 35th IEEE Conference on Local Computer Networks (LCN '10)*, pp. 1032–1039, Denver, Colo, USA, October 2010.
- [7] H. Haiying, H. Jinghan, W. Xiaojun et al., "Strategy research of V2G participating load responses based on improved particle swarm optimization," *Power System Technology*, vol. 35, no. 10, pp. 165–169, 2011.
- [8] W. Tian, J. He, J. Jiang, L. Niu, and X. Wang, "Multi-objective optimization of charging dispatching for electric vehicle battery swapping station based on adaptive mutation particle swarm optimization," *Power System Technology*, vol. 36, no. 11, pp. 25–29, 2012.
- [9] S. Su, J. Sun, X. Lin, and X. Li, "Electric vehicle smart charging navigation," *Proceedings of the CSEE*, vol. 33, supplement, pp. 59–67, 2013.
- [10] B. Sun, Q. Liao, P. Xie, G. Zhou, Q. Shi, and H. Ge, "A cost-benefit analysis model of vehicle-to-grid for peak shaving," *Power System Technology*, vol. 36, no. 10, pp. 30–34, 2012.
- [11] L. Sun and Z. Yang, "Optimal charging schedule of PHEV taxi with time-varying price," in *Proceedings of the 31st Chinese Control Conference (CCC '12)*, pp. 2537–2542, July 2012.
- [12] Z. Yang, L. Sun, J. Chen, Q. Yang, X. Chen, and K. Xing, "Profit maximization for plug-in electric taxi with uncertain future electricity prices," *IEEE Transactions on Power Systems*, vol. 29, no. 6, pp. 3058–3068, 2014.
- [13] J.-L. Lu, M.-Y. Yeh, Y.-C. Hsu, S.-N. Yang, C.-H. Gan, and M.-S. Chen, "Operating electric taxi fleets: a new dispatching strategy with charging plans," in *Proceedings of the IEEE International Electric Vehicle Conference (IEVC '12)*, pp. 1–8, March 2012.
- [14] E. Yao, Z. Yang, Y. Song, and T. Zuo, "Comparison of electric vehicle's energy consumption factors for different road types," *Discrete Dynamics in Nature and Society*, vol. 2013, Article ID 328757, 7 pages, 2013.
- [15] D. Zhang, J. Jiang, W. Zhang, Y. Zhang, and Y. Huang, "Economic operation of electric vehicle battery swapping station based on genetic algorithms," *Power System Technology*, vol. 37, no. 8, pp. 2101–2107, 2013.
- [16] H. Xiong, T. Xiang, Y. Zhu, X. Song, and H. Chen, "Electric vehicle public charging stations location optimal planning,"

*Automation of Electric Power Systems*, vol. 36, no. 23, pp. 65–70, 2012.

## Research Article

# A Traction Control Strategy with an Efficiency Model in a Distributed Driving Electric Vehicle

Cheng Lin<sup>1,2</sup> and Xingqun Cheng<sup>1,2</sup>

<sup>1</sup> Beijing Co-Innovation Center for Electric Vehicles, Beijing Institute of Technology, Beijing 100081, China

<sup>2</sup> National Engineering Laboratory for Electric Vehicles, Beijing Institute of Technology, Beijing 100081, China

Correspondence should be addressed to Xingqun Cheng; [xingqun Cheng@bit.edu.cn](mailto:xingqun Cheng@bit.edu.cn)

Received 29 June 2014; Accepted 13 July 2014; Published 12 August 2014

Academic Editor: Xuan Zhou

Copyright © 2014 C. Lin and X. Cheng. This is an open access article distributed under the Creative Commons Attribution License, which permits unrestricted use, distribution, and reproduction in any medium, provided the original work is properly cited.

Both active safety and fuel economy are important issues for vehicles. This paper focuses on a traction control strategy with an efficiency model in a distributed driving electric vehicle. In emergency situation, a sliding mode control algorithm was employed to achieve antislip control through keeping the wheels' slip ratios below 20%. For general longitudinal driving cases, an efficiency model aiming at improving the fuel economy was built through an offline optimization stream within the two-dimensional design space composed of the acceleration pedal signal and the vehicle speed. The sliding mode control strategy for the joint roads and the efficiency model for the typical drive cycles were simulated. Simulation results show that the proposed driving control approach has the potential to apply to different road surfaces. It keeps the wheels' slip ratios within the stable zone and improves the fuel economy on the premise of tracking the driver's intention.

## 1. Introduction

To address the two urgent issues nowadays of protecting the environment and achieving energy sustainability, it is of strategic importance on a global scale to replace oil-dependent vehicles with electric vehicles (EVs) [1–3]. Compared with internal combustion engine vehicles, electric vehicles with motors have many fascinating advantages, such as the quicker and more accurate torque generation, the easier measurement of motor torque [4], which provide a broad prospect for the vehicle dynamics control. Many types of drive system have been developed for electric vehicles by researchers in the last few years. Kim et al. studied the mode transition control for an internal combustion engine together with a motor driving type [5]. Liu et al. made a further research on driving control for electric vehicles with independently driven front and rear wheels [6]. Motors of the distributed driving electric vehicle are mounted directly in wheels or nearby wheels, which lead to a short and efficient transmission chain and compact structure, so it has been becoming an important research direction of electric vehicles [7].

The vehicle dynamics control of the distributed driving electric vehicle is one of the research focuses currently, which attracts lots of scholars' attention [8–10]. Ibrahim et al. provided a new load torque estimator to improve the stability of the traction drive system [11]. Gasbaoui et al. proposed a direct torque control strategy to ensure safety and stability, which are verified through all types of roads [12]. Athari et al. proposed a novel torque vectoring control strategy for an electric-drive vehicle with four in-wheel motors to assist a driver in handling a vehicle in unexpected conditions [13]. Chen et al. studied a fuzzy adhesion control method for four-wheel driven electric vehicle and the method was confirmed by the road experiment [14]. Kim et al. put forward a driving control algorithm for a 6WD/6WS vehicle equipped with 6 in-wheel motors to improve vehicle stability and maneuverability [15]. Several researchers also investigated the control strategies for improving vehicle energy economy [16, 17]. To improve the energy economy and the driving stability, the control strategy for the distributed driving electric vehicles is necessary and very important.

Focusing on a 4WD (4 wheels drive) distributed driving electric vehicle, this paper presented a driving control

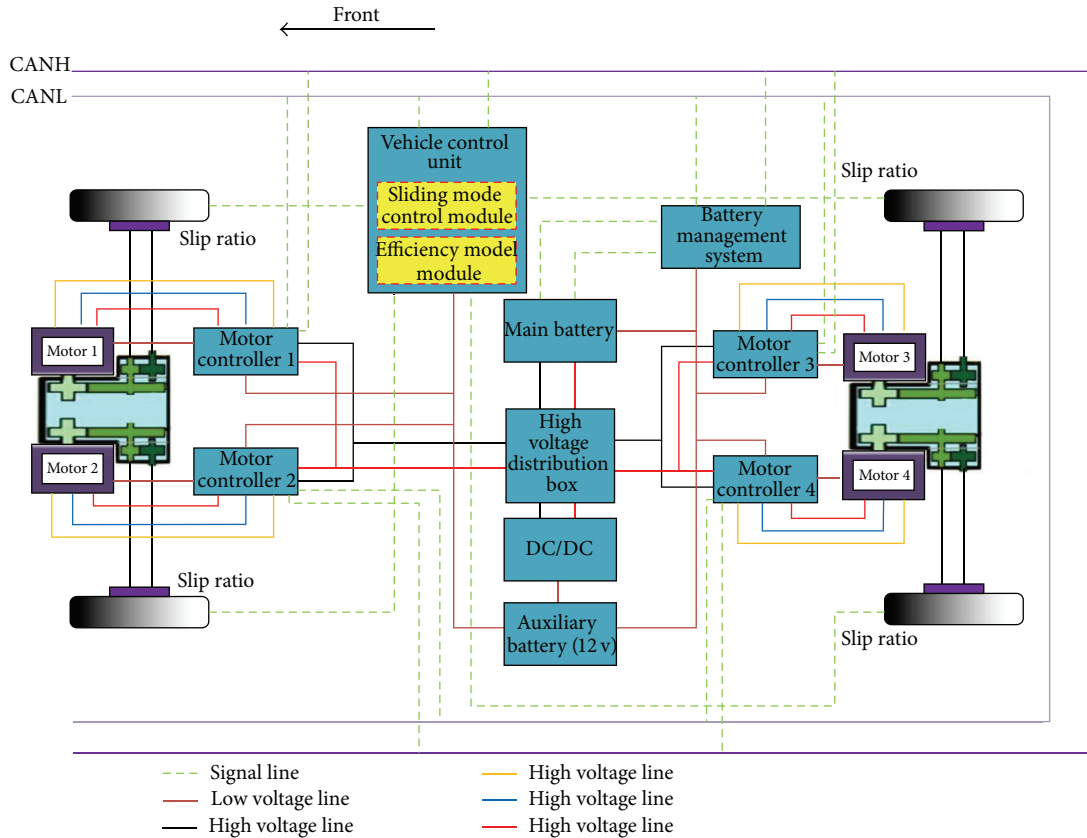


FIGURE 1: The vehicle structure.

strategy to improve the driving safety and fuel economy. In order to ensure the driving safety during the emergency case, we used the sliding mode control strategy to guarantee the wheel slip rate within the stable zone. Apart from this case, an efficiency model is implemented to reduce the energy consumption. The efficiency model is built by an optimization method within a two-dimensional design space and the space contains the acceleration pedal signal and the vehicle speed. When building the efficiency model, to avoid the problem that online optimization methods have the limitations of heavy computation, we use the response surface techniques to develop a predictive model which can realize a real-time control through an offline optimization stream. The driving control strategy for different cases was verified through the simulation.

This paper is organized as follows. The vehicle dynamics model is built in Section 2, where the basic parameters of the vehicle are given. In Section 3, the driving control strategy with an efficiency model is designed. The simulation studies and analysis experiment are reported in Section 4 before conclusions are drawn in Section 5.

## 2. Vehicle Dynamics Model

**2.1. System Configuration.** The power system configuration of a distributed driving electric vehicle is shown in Figure 1.

It is a 4WD electric vehicle with four motors. Through high-voltage distribution box, the main battery, which was

monitored by a battery management system directly, provides electric energy to each motor controller. The motor controller will invert the direct current to three-phase alternating current for motor according to the torque requirement command. In order to give the controllers and other low-voltage apparatus power supply, an auxiliary battery is equipped and it is charged by the main battery through DC/DC transformer. In addition, the vehicle communication is based on CAN (controller area net) bus. In longitudinal driving, the vehicle control unit will analyze and calculate each motor's torque demand of the electric vehicle in real time according to the control strategy. Then, the drive torque requirement of each motor will be transmitted to the CAN bus. After accepting the torque requirement signal from the CAN bus, the motor controller will change them into the three-phase alternating current to make the corresponding motor generate the actual drive torque. In the end, the motors drive the vehicle and the motor controllers give feedback to the CAN bus. In order to acquire the vehicle speed, the electric vehicle is equipped with a GPS.

The distributed driving electric vehicle specification is shown in Table 1.

### 2.2. Vehicle Longitudinal Dynamic Model

**2.2.1. Single-Wheel Model.** In considering that each wheel can be controlled independently in the distributed driving electric vehicles, a single-wheel model is adopted. The model

TABLE 1: Basic parameters of the vehicle.

Parameters	Symbols	Units	Values
Gross mass	$m$	kg	1350
Wheelbase (front, rear)	$(l_f, l_r)$	m	(1.085, 1.386)
Track width (front, rear)	$(d_f, d_r)$	m	(1.429, 1.422)
Centroid height	$h_g$	m	0.48
Windward area	$A$	m <sup>2</sup>	1.895
Air drag coefficient	$C_D$	—	0.34
Wheel rolling radius	$r$	m	0.281
Rolling resistance coefficient	$f_r$	—	0.018
Wheel rotational inertia	$I$	kg·m <sup>2</sup>	0.87
Reducer ratio	$i_0$	—	7.013
Motor peak/rated power	$P_{max}/P_N$	kW	12.5/7.5
Motor maximum/rated speed	$n_{max}/n_N$	rpm	9500/4000
Motor peak/rated torque	$T_{max}/T_N$	N·m	45/18

is shown in Figure 2. According to the vehicle dynamic, if the rolling resistance is ignored, the wheel motion equation can be defined as

$$I\dot{\omega} = T_t - F_t r, \quad (1)$$

where  $I$  is the wheel rotational inertia,  $F_t$  means the road traction force of the wheel,  $\omega$  denotes the wheel speed,  $T_t$  represents the traction torque of the wheel, and  $r$  is the radius of the wheel.

Furthermore, the slip ratio of the wheel can be described as

$$\lambda = \frac{\omega r - v}{\omega r}, \quad (2)$$

where  $\lambda$  is the slip ratio of the wheel and  $v$  is the vehicle speed.

**2.2.2. Tire Model.** The “Magic Formula” developed by Pacejka et al. is widely used as a modelling way in the dynamic simulation [18]. For the longitudinal dynamic motion, tire longitudinal force  $F_t$  can be simplified as

$$F_t = D \sin \{C \arctan [B\lambda - E(B\lambda - \arctan B\lambda)]\}, \quad (3)$$

where  $D$ ,  $C$ ,  $B$ , and  $E$  denote the peak, shape, stiffness, and curvature factor, respectively. The above parameters can be obtained as follows:

$$\begin{aligned} C &= 1.65, \\ B &= \frac{(a_3 F_N + a_4)}{((a_1 F_N + a_2) C \times \exp(a_5 F_N))}, \\ D &= (a_1 F_N + a_2) F_N, \\ E &= a_6 F_N^2 + a_7 F_N + a_8, \end{aligned} \quad (4)$$

where  $F_N$  denotes the vertical load of the tire and  $a_i$  ( $i = 1, 2, \dots, 8$ ) is the fitting coefficient which can be obtained by Table 2.

TABLE 2: The fitting coefficients of the “Magic Formula”\*.

$a_1$	$a_2$	$a_3$	$a_4$	$a_5$	$a_6$	$a_7$	$a_8$
-21.3	1144	49.6	226	0.069	-0.006	0.056	0.486

\*  $a_i$  ( $i = 1, 2, \dots, 8$ ) is the fitting coefficient required to solve the longitudinal tire force, respectively, in the “Magic Formula” developed by Pacejka et al. [18].

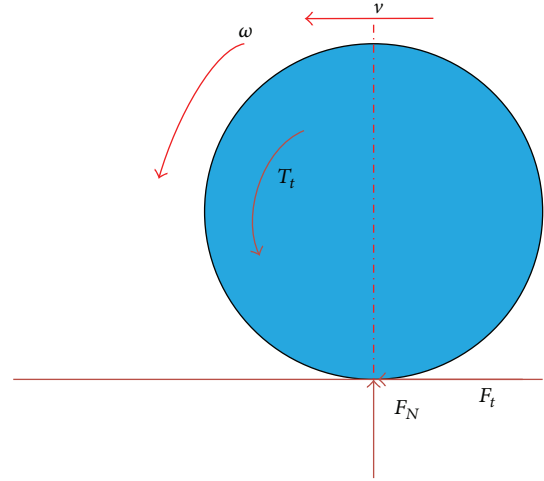


FIGURE 2: The single-wheel model.

**2.2.3. Driving Torque Model.** Based on the peak torque of motors under a given motor speed, the required traction torque for the general driving case can be obtained as

$$T = 4T_{motor\_max} \times A_{ps}, \quad (5)$$

where  $T_{motor\_max}$  is the peak torque of the motor under a given motor speed and it can be obtained by Figure 3;  $A_{ps}$  means the accelerator pedal signal.

**2.2.4. Motor Efficiency Model.** The motor efficiency  $\eta_{motor}$  comprising the motor controller efficiency shown in Figure 4 was measured by a dedicated dynamometer.

According to Figure 4, as long as the motor rotation speed  $n$  and the motor torque  $T$  have been calculated out, the corresponding efficiency values  $\eta_{motor}$  can be obtained from the test data table. The data which are not in the table can be calculated by using binary Lagrange interpolation method, as shown in Figure 5. The motor efficiency at any point can be calculated with the following formula:

$$\begin{aligned} \eta_1 &= \frac{n - n_1}{n_2 - n_1} \eta(n_2, T_1) + \frac{n_2 - n}{n_2 - n_1} \eta(n_1, T_1), \\ \eta_2 &= \frac{n - n_1}{n_2 - n_1} \eta(n_2, T_2) + \frac{n_2 - n}{n_2 - n_1} \eta(n_1, T_2), \\ \eta(n, T) &= \frac{T - T_1}{T_2 - T_1} \eta_2 + \frac{T_2 - T}{T_2 - T_1} \eta_1. \end{aligned} \quad (6)$$

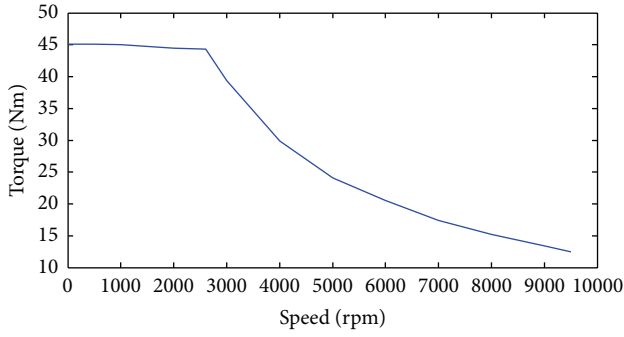


FIGURE 3: The peak torque versus motor speed curve.

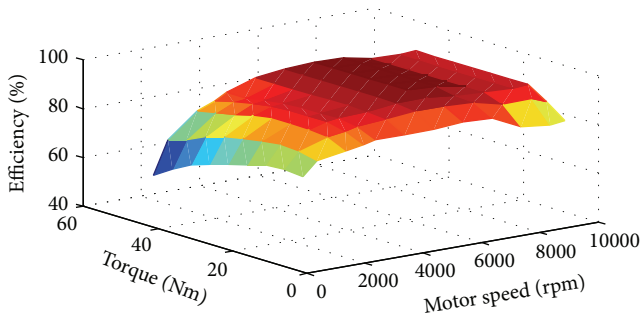
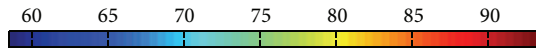


FIGURE 4: The efficiency map of the motor.

### 3. Driving Control Strategy and Algorithm

3.1. *The Flow Chart of the Control Strategy.* This paper mainly investigated the control strategies on longitudinal driving scenario, which has two layers. Figure 6 shows the hierarchical control strategy. The top layer is designed to obtain the reasonable motor torque's preallocation and the lower layer aims at guaranteeing the longitudinal stability and the required torque demand of the driver. According to the vehicle speed and the acceleration pedal signal, the top layer can obtain a motor torque preallocation scheme based on the efficiency model. Then the distributed driving torque will be delivered to the low layer. The low layer will calculate the slip ratio based on the torque preallocation value first and then judge whether it needs to adopt the sliding mode control algorithm. In the end it will give a torque requirement command to each motor obeying the principle of the equal torque between two wheels of the same axis.

#### 3.2. The Top Layer

3.2.1. *The Efficiency Model.* When the vehicle drives in the general case, the drive torque will be distributed by an efficiency model in this paper.

To maximize the driving efficiencies, the optimization method is usually applied to develop an efficiency model. However, it may involve the real-time problem during vehicle driving. So a response surface model technology was used

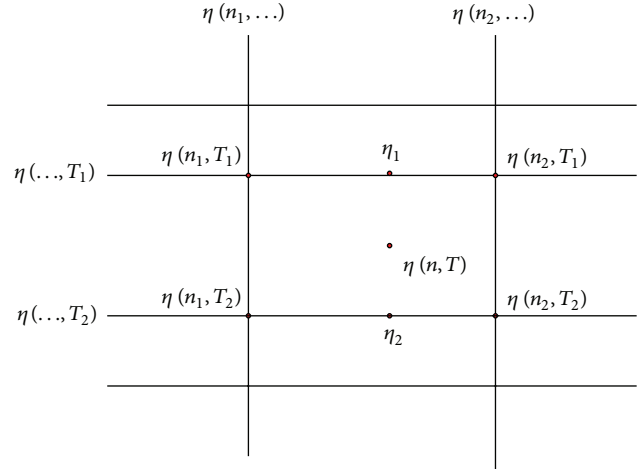


FIGURE 5: The binary Lagrange interpolation principle.

in the efficiency model to realize the real-time control. The efficiency model was built in the two-dimensional design spaces that consist of the acceleration pedal signal and the vehicle speed based on offline optimization data.

(1) *The Optimization Mathematic Model.* To carry out the offline optimization stream, an optimization mathematic model was established to get the maximum of total driving efficiency.

The distributed driving electric vehicle (see Figure 1), which is the focus of this paper, has four motors. The overall output torque of the motors  $T$  is given by the following:

$$T = T_1 + T_2 + T_3 + T_4, \tag{7}$$

where  $T_1, T_2, T_3,$  and  $T_4$  are the torques of motor 1, motor 2, motor 3, and motor 4, respectively.

Normally the two motor torques of each axis should be equal under the longitudinal dynamics model:

$$T_1 = T_2, \quad T_3 = T_4. \tag{8}$$

As a consequence of the torque balance in (7) and (8), the operation points of the powertrain are fully determined by choosing the division of the motor torque between the front axis and the rear axis. So the traction force's allocation coefficient is defined as the torque split factor:

$$\alpha = \frac{T_1 + T_2}{T}. \tag{9}$$

When  $\alpha$  equals 1, it means that the vehicle is in the front axis drive manner alone. Considering that the front axis driving manner alone is similar to the rear in its result, the allocation coefficient  $\alpha$  can be limited from 0.5 to 1.

The overall efficiency of the powertrain system is obtained by the efficiency model of each motor from the experiment as follows:

$$\eta_{\text{total}} = \frac{\sum_{i=1}^4 T_i n_i}{\sum_{i=1}^4 (T_i n_i / \eta_{\text{motor},i})}, \tag{10}$$

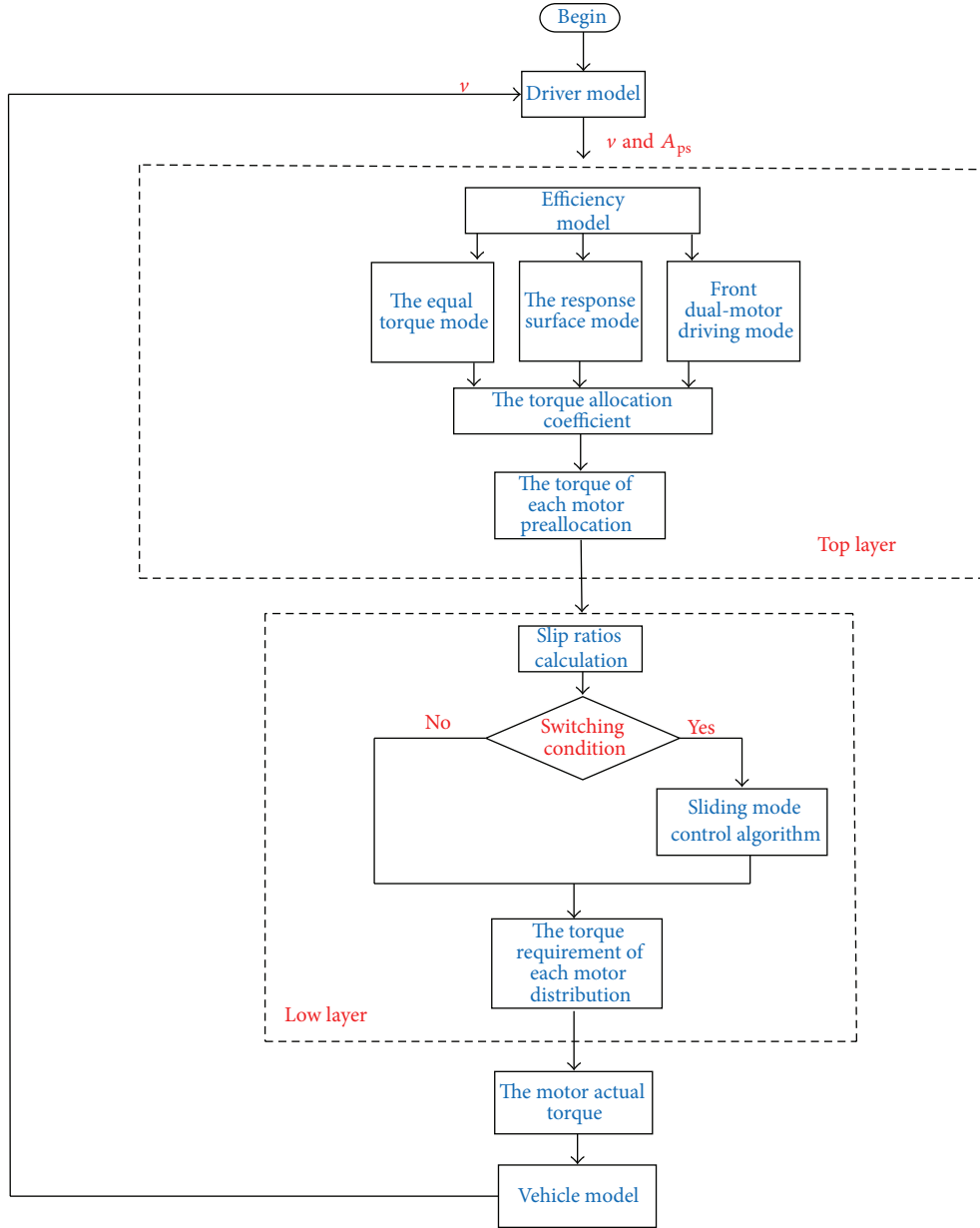


FIGURE 6: The traction control strategy.

where  $T_i$  and  $n_i$  ( $i = 1, 2, 3, 4$ ) denote each motor speed and torque, respectively.  $\eta_{motor,i}$  denotes the efficient of each motor under the corresponding motor speed.  $\eta_{total}$  denotes the total efficient of the power motors system.

In considering that constraint, the optimization mathematic model can be expressed as follows:

$$\begin{aligned} \max_{\alpha(A_{ps}, v)} \eta &= \eta_{total}(A_{ps}, v, \alpha), \\ T_i &\leq T_{i,max} \quad (i = 1, 2, 3, 4), \\ 0 &\leq A_{ps} \leq 1, \\ 0.5 &\leq \alpha \leq 1, \\ 0 &\leq v \leq 120, \end{aligned} \tag{11}$$

where  $T_{i,max}$  ( $i = 1, 2, 3, 4$ ) denote the maximum output torques of every motor under a given motor speed, respectively.

(2) *The Offline Optimization Stream.* In accordance with the optimization mathematic model, an offline optimization was designed as shown in Figure 7. It can be mainly divided into three steps.

*Step 1.* Taking the acceleration pedal signal  $A_{ps}$  and the speed  $v$  as the continuous design space, a discrete sampling point set can be obtained in the DOE sampling module.

*Step 2.* Taking the sampling points as the input parameters,  $\alpha$  as the optimization design variable, and the maximum

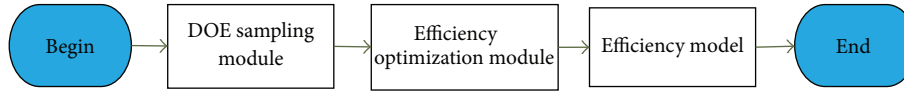


FIGURE 7: The offline efficiency optimization stream.

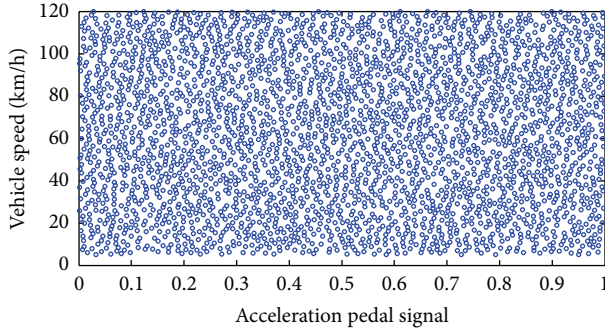


FIGURE 8: The sampling points in the design space.

driving efficiency  $\eta_{total}$  as the optimization target, the optimum value of  $\alpha$  under each sampling point will be obtained by the efficiency optimization module.

*Step 3.* Based on the optimization data, which is obtained in the efficiency optimization module, create an efficiency model in which the response surface method is used. With regard to the efficiency model,  $A_{ps}$  and  $v$  are viewed as inputs, and the optimum value of  $\alpha$  is viewed as output.

**3.2.2. DOE Sampling for the Continuous Input Design Space.** As we can see from Figure 4, when the speed and torque of the motor are given, we can calculate the efficiency of this point by the efficiency map of the motor. Hence we take the vehicle speed and the acceleration pedal signal as the input design space, which can be deduced by the speed and torque of the motor. Considering the vehicle speed limit of the expressway, the maximum vehicle speed of the efficiency model is limited to 120 km/h and the acceleration pedal signal ranges from 0 to 1. Then the continuous input design space can be discrete as shown in Figure 8.

To improve the predictive precision of the efficiency model and evaluate the expected allocation coefficient, in this paper 3000 points were sampled in the design space (see Figure 8) using the optimization Latin hypercube design (Opt LHD) method. The Opt LHD can make the sampling point distribution more uniform and has a better space-filling performance than other experimental design methods [19].

**3.2.3. The Optimization and Analysis of the Traction Force Allocation Coefficient.** From (9) we can see that the distributed coefficient has a linear relation with each motor torque. And as shown from Figure 4, the efficiency calculation is mainly a single peak problem. Therefore the Hooke-Jeeves technique is adopted during the optimization computation process, which is well suitable for both linear design spaces and nonlinear design spaces. Furthermore the

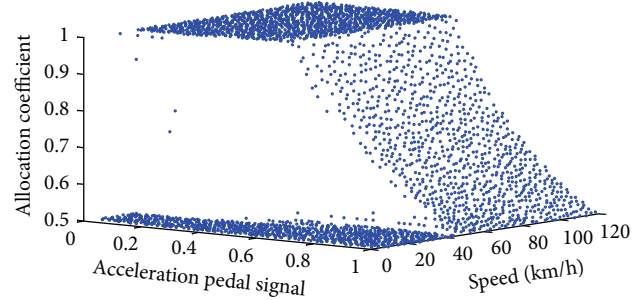


FIGURE 9: Allocation coefficients optimization results.

approach is a direct search method and has a high rate of convergence [20].

Given a point in the design space, an optimal traction force distributed coefficient can be obtained by maximizing overall efficiency of the powertrain system shown in (11). Figure 9 shows the optimization results of the allocation coefficient. To furthermore analyze the optimization results, we divide the design space into three areas using three colors according to the overall characteristics in Figure 9, as shown in Figure 10.

According to the design space area division results, we redraw the optimization results of the allocation coefficient using three colors, as shown in Figures 11 and 12. From the results above, we can set up an efficiency model with three zones. The first area is the blue one where the allocation coefficient equals 1; that is, only the motors of the front axis work. The second area is the red one where the allocation coefficient is 0.5 that means that each motor outputs equal torque. The third area is the green one where we should present a response surface model to predict the allocation coefficient based on the acceleration pedal signal and the vehicle speed.

**3.2.4. The Efficiency Model Design.** As discussed above, a predictive model was proposed by using the RSM (response surface model) approach. RSM approximation is based on a polynomial fit via the least squares regression of the output parameters to the input parameters. Here the input parameters are the acceleration pedal signal and the vehicle speed and the output parameter is the allocation coefficient. The RSM obtained from the optimization data can be expressed as follows:

$$\begin{aligned} \alpha = & -9.88783A_{ps} + 1.369829 \times 10^{-6}v \\ & + 1.36306 \times 10^1 A_{ps}^2 - 1.28573 \times 10^{-8}v^2 \\ & - 7.96798 \times 10^{-7}A_{ps}v - 9.27380A_{ps}^3 \end{aligned}$$

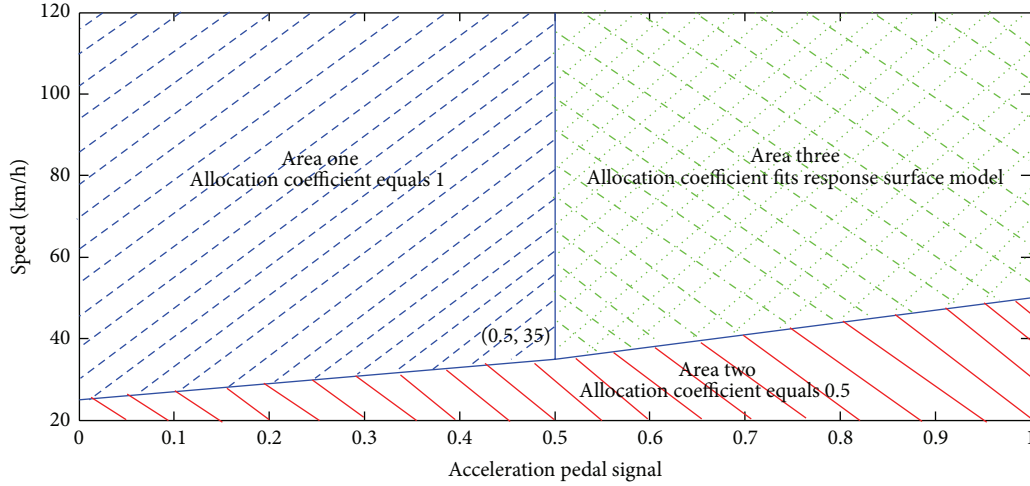


FIGURE 10: Design space area division.

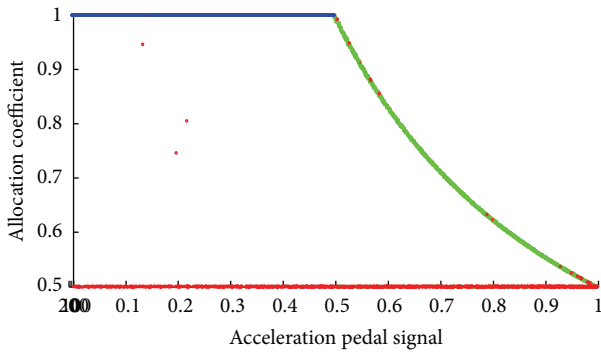


FIGURE 11: Optimization results side view.

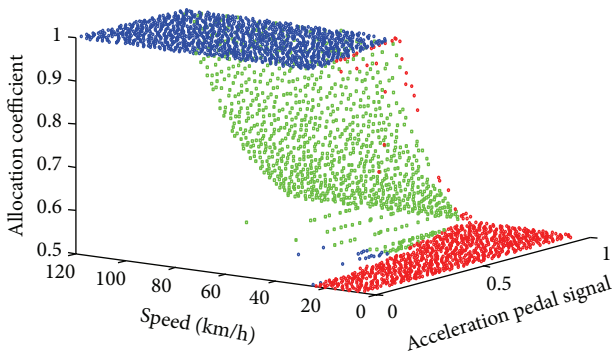


FIGURE 12: Optimization results right front view.

$$\begin{aligned}
 &+ 7.64492 \times 10^{-11} v^3 + 2.49224 A_{ps}^4 \\
 &- 1.59573 \times 10^{-13} v^4 + 3.53917.
 \end{aligned}
 \tag{12}$$

3.3. The Lower Layer. The main target of the lower layer is to ensure the vehicle longitudinal stability and obtain the reasonable torque requirement of each motor distribution.

3.3.1. The Switch Condition. The lower layer needs to judge the driving condition to realize the strategy switch. As we all know, according to the adhesion ratio versus slip ratio curves of the tires, if the slip ratio is lower than 15–20%, the vehicle will be at the general driving case. On the contrary, the vehicle will be at antislip control scenario. So, the switching condition is defined as the slip ratio exceeding 15%; that is, if the slip ratio is lower than 15%, it is at general driving case and efficiency model works; otherwise the sliding mode control algorithm will be activated to ensure the driving safety.

3.3.2. The Sliding Mode Control Algorithm. When the vehicle driving in the emergency case, that is, the slip ratio being not lower than 15–20%, if the output traction torque still follows the required traction torque, the wheel will spin excessively. To ensure the driving safety, the traction torque should be limited and the sliding mode control strategy is used under such circumstance.

The sliding mode control strategy strives to control the slip ratio of the wheel to 16%, by which the maximum adhesion performance will be obtained. The switching function can be expressed as follows:

$$s = \lambda - \lambda_0 + c \int_0^t (\lambda - \lambda_0) dt, \tag{13}$$

where  $\lambda_0$  is the target value of the slip ratio, which is equal to 16%;  $c$  is the weighting parameter which denotes the slope value of the sliding curve.

The reaching law is defined as

$$\dot{s} = -\varepsilon \operatorname{sgn}(s), \tag{14}$$

where  $\varepsilon$  denotes the reaching speed.

Taking a derivative of (13), we can give

$$\dot{s} = \dot{\lambda} + c(\lambda - \lambda_0). \tag{15}$$

Taking a derivative of (2) gives

$$\dot{\lambda} = \frac{(v\dot{\omega} - \dot{v}\omega)}{\omega^2 r}. \tag{16}$$

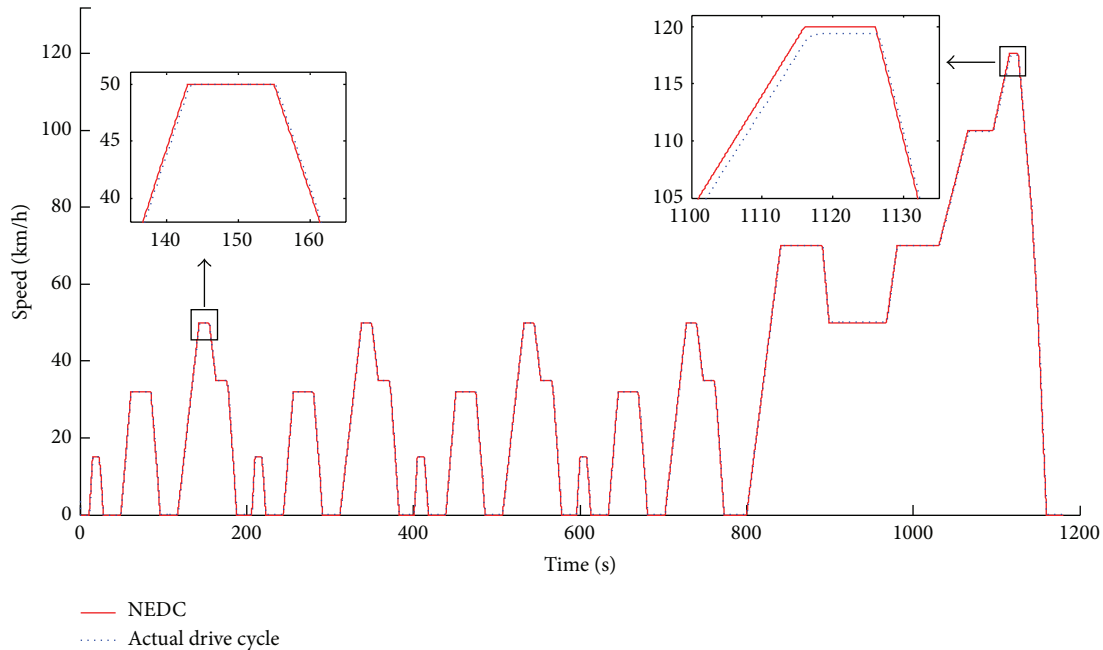


FIGURE 13: The NEDC and actual following DC.

Substituting (16), (1), and (14) to (15) gives

$$T_t = -(\varepsilon \operatorname{sgn}(s) + c(\lambda - \lambda_0)) \frac{I\omega^2 r}{v} + \omega \dot{v} \frac{I}{v} + F_t(\lambda, \dot{v}) r. \quad (17)$$

**3.3.3. The Torque Requirement of Each Motor Distribution.** If the slip ratio value is higher than 15% based on the motor torques preallocated in the efficiency model, the switch condition is satisfied and the sliding mode control strategy will be activated. In this case the torque preallocation value will be regulated based on the sliding mode controller and the equal torque principle of the wheels on the same axis. Then the torque distribution command of each motor will be transmitted to the motors accordingly.

## 4. Simulation Result and Analysis

Simulation studies have been carried out to verify the proposed control strategy under the assumption that the vehicle drives along straight road without road gradient.

**4.1. The Simulation Analysis for the Efficiency Model.** Figures 13, 14, and 15 show the simulation results of the efficiency model compared with even distribution strategy (allocation coefficient equals 0.5) for the general road scenario over the NEDC (New European Driving Cycle) condition. Figure 13 illustrates that the actual following DC (Driving Cycle) in the simulation is well consistent with the NEDC, except that there is a little bit of tracking error in the high-speed section, but this does not affect the analysis of the simulation results.

Figure 14 illustrates the instant total power and the overall energy consumption improvement results. The simulation results in Figure 14 show that the proposed efficiency model

can reduce the total power and overall energy consumption over the NEDC, especially in the high-speed zone.

Figure 15 shows the total efficiency contrast and the acceleration pedal signal over the NEDC. The simulation results indicate that the total efficiency has been improved under the efficiency model control strategy. The effect in the high-velocity zone of the driving cycle is obvious since the allocation coefficient is different from 0.5 mainly in those areas. Furthermore as shown in Figure 15, the acceleration pedal signal is mostly below 0.5, which conforms to the actual drive situation.

To verify the response surface model, in which the acceleration pedal signal is larger than 0.5, the simulation of 30 seconds acceleration to 120 km/h has been conducted. As shown in Figures 16, 17, and 18, the simulation results are similar to the results over the NEDC. The instant power and energy consumption under the efficiency model control strategy are lower than under even distribution strategy, and the total efficiency is also higher. Furthermore, the acceleration pedal signal is between the interval of 0.5 and 0.7 in which the response surface model of the efficiency model works after 5 seconds or so.

Table 3 lists the simulation results of energy economy improvement. Compared with even distribution strategy, the proposed efficiency model control strategy can decrease energy consumption by 2.3% in the NEDC situation and by 1.1% in the 0~120 km/h acceleration case. The total average efficiency is 81.12% under the even distribution strategy and 81.89% under the efficiency model over the NEDC. And the total average efficiency under the efficiency model over the acceleration case is also higher than under the even distribution strategy as shown in Table 3. Therefore, the efficiency model control strategy can improve energy economy compared with the even distribution strategy.

TABLE 3: Energy consumption result.

Strategy	Even distribution strategy		The efficiency model		
Situation	Energy consumption	Total average efficiency	Energy consumption	Total average efficiency	Improvement
NEDC	0.9916 (kW·h)	81.12%	0.9689 (kW·h)	81.89	2.3%
Acceleration DC	0.2876 (kW·h)	87%	0.2845 (kW·h)	87.86%	1.1%

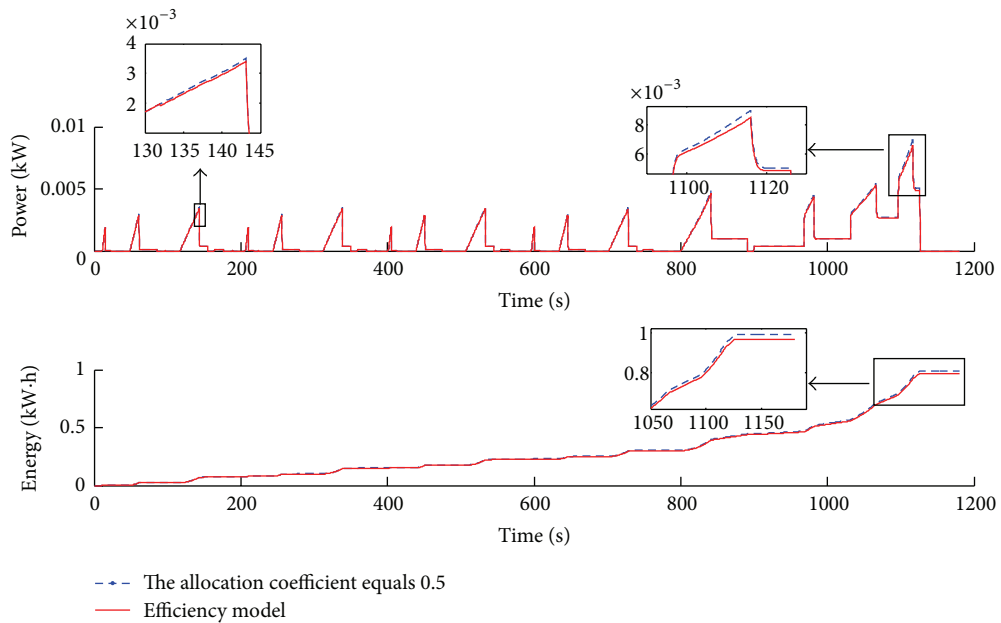


FIGURE 14: The time history of power and energy consumption over the NEDC.

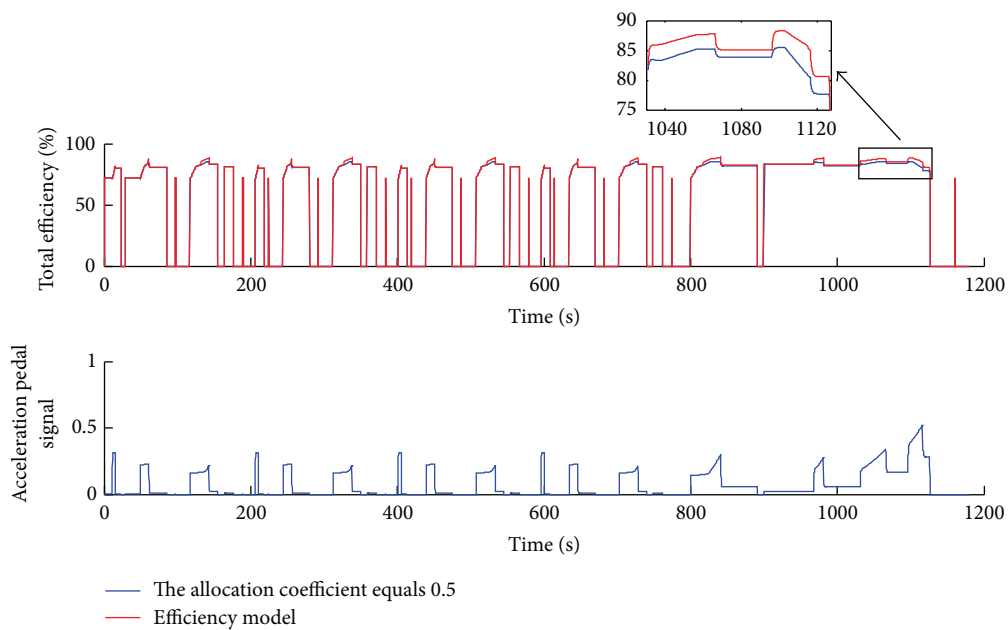


FIGURE 15: The time history of the total efficiency and acceleration pedal signal over the NEDC.

#### 4.2. The Simulation Analysis for the Sliding Mode Control Algorithm

4.2.1. The Road Simulation Parameters. The peak adhesion coefficient at each wheel represents the road adhesion

conditions. This paper sets the surface parameters at each wheel of different road surfaces as shown in Figure 19. The adhesion coefficients of high adhesion road, low adhesion, and uniform surface are constant and the coefficients of joint road represent an adhesion step change surface.

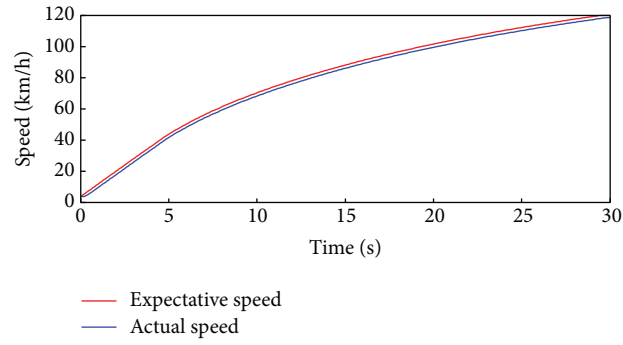


FIGURE 16: The acceleration driving cycle and actual following DC.

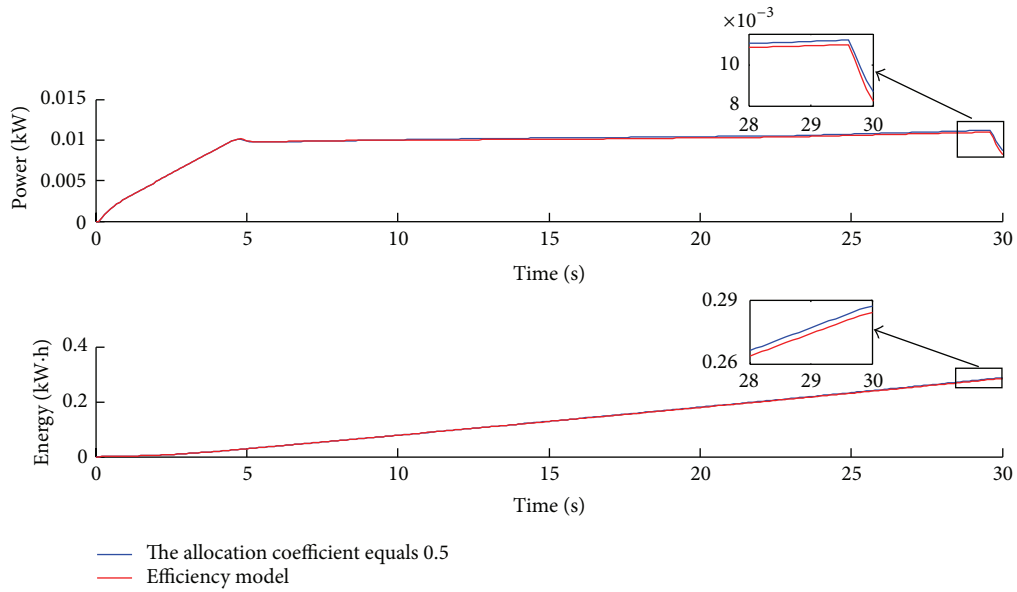


FIGURE 17: The time history of power and energy consumption over the acceleration DC.

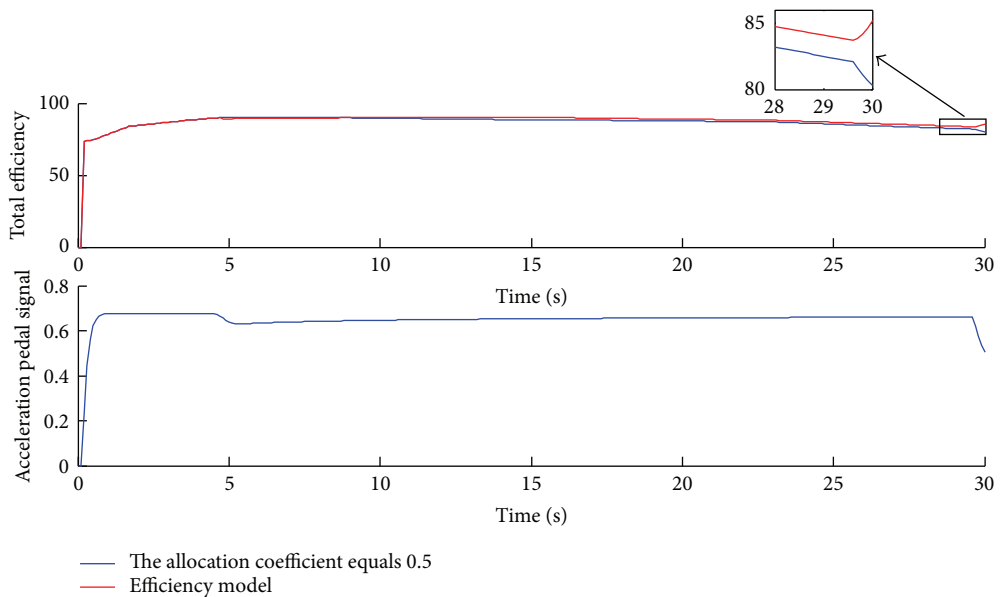


FIGURE 18: The time history of the total efficiency and  $A_{ps}$  over the acceleration DC.

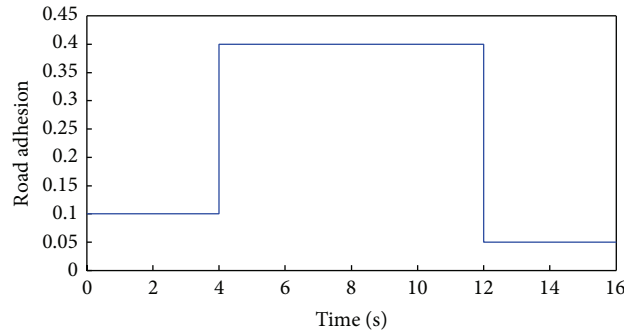


FIGURE 19: Adhesion coefficients of road surfaces.

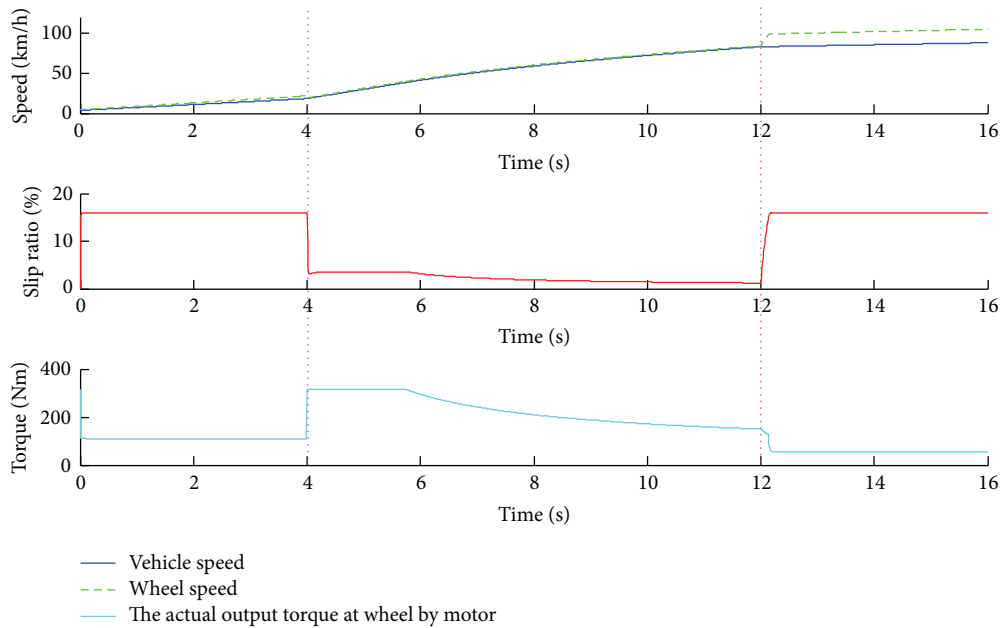


FIGURE 20: The simulation results of joint road surface.

4.2.2. *The Simulation Results and Analysis.* Figure 20 shows the simulation results of sliding mode control strategy on the joint road surface which has three sections. As shown in Figure 19, the adhesion coefficients of the road sections are 0.1, 0.4 and 0.05 in sequence. First the distributed driving electric vehicle runs on the road whose adhesion is 0.1. When the slip ratio is higher than 15%, the sliding mode control strategy works and the slip ratio converges to 16%. While the vehicle comes from the first road section to the second road section whose adhesion is 0.4 at the fourth second, the slip ratio is lower than 15%. Then the sliding mode control strategy quits and the motor torque distribution complies with the efficiency mode control strategy. Since the vehicle reenters the low adhesion road surface at the twelfth second and the slip ratio is greater than 15%, the sliding mode control strategy resumes and the slip ratio also converges to 16% according to the setting value.

**5. Conclusions**

- (1) A traction control strategy, including an efficiency model control strategy for the general road surface

scenario and the sliding mode control strategy for the emergency antislip control scenario, has been studied.

- (2) Several simulation experiments have been carried out to verify the efficiency model control strategy on the general road surface scenario. The simulation results demonstrated that the efficiency model control strategy could improve the vehicle fuel economy comparing with the even torque distribution strategy. It can decrease energy consumption by 2.3% in the NEDC situation and by 1.1% in the 0~120 km/h acceleration DC case under the proposed efficiency model controls strategy.
- (3) Aiming at the emergency driving scenario, the sliding mode control strategy has been analyzed on the joint road surface. The simulation results indicate that the slip ratios were preferably controlled to 16% for different adhesion road surface change cases.

## Conflict of Interests

The authors declare that there is no conflict of interests regarding the publication of this paper.

## Acknowledgment

This work was supported by the National Natural Science Foundation of China (51175043).

## References

- [1] T. R. Hawkins, O. M. Gausen, and A. H. Strømman, "Environmental impacts of hybrid and electric vehicles-a review," *International Journal of Life Cycle Assessment*, vol. 17, no. 8, pp. 997–1014, 2012.
- [2] R. Xiong, F. Sun, Z. Chen, and H. He, "A data-driven multi-scale extended Kalman filtering based parameter and state estimation approach of lithium-ion polymer battery in electric vehicles," *Applied Energy*, vol. 113, pp. 463–476, 2014.
- [3] R. Xiong, F. C. Sun, H. W. He, and T. Duy Nguyen, "A data-driven adaptive state of charge and power capability joint estimator of lithium-ion polymer battery used in electric vehicles," *Energy*, vol. 63, pp. 295–308, 2013.
- [4] Y. Hori, "Future vehicle driven by electricity and control: research on four-wheel-motored 'UOT Electric March II,'" *IEEE Transactions on Industrial Electronics*, vol. 51, no. 5, pp. 954–962, 2004.
- [5] H. Kim, J. Kim, and H. Lee, "Mode transition control using disturbance compensation for a parallel hybrid electric vehicle," *Proceedings of the Institution of Mechanical Engineers D: Journal of Automobile Engineering*, vol. 225, no. 2, pp. 150–166, 2011.
- [6] W. Liu, H. W. He, and J. K. Peng, "Driving control research for longitudinal dynamics of electric vehicles with independently driven front and rear wheels," *Mathematical Problems in Engineering*, vol. 2013, Article ID 408965, 17 pages, 2013.
- [7] Z. Yu, Y. Feng, and L. Xiong, "Review on vehicle dynamics control of distributed drive electric vehicle," *Journal of Mechanical Engineering*, vol. 49, no. 8, pp. 105–114, 2013.
- [8] Z. Yan-e, Z. Jianwu, and H. Xu, "Development of a high performance electric vehicle with four-independent-wheel drives," *Development*, vol. 2013, pp. 4–8, 2008.
- [9] K. Jalali, T. Uchida, J. McPhee, and S. Lambert, "Development of a fuzzy slip control system for electric vehicles with in-wheel motors," *SAE International Journal of Alternative Powertrains*, vol. 1, no. 1, pp. 46–64, 2012.
- [10] G. Yin, S. Wang, and X. Jin, "Optimal slip ratio based fuzzy control of acceleration slip regulation for four-wheel independent driving electric vehicles," *Mathematical Problems in Engineering*, vol. 2013, Article ID 410864, 7 pages, 2013.
- [11] Z. Ibrahim, N. M. Yaakop, F. Ahmad et al., "Improved direct torque control load torque estimator with the influence of steering angle for dual induction motors electric vehicle traction drive system," *World Applied Sciences Journal*, vol. 21, no. 2, pp. 11–22, 2013.
- [12] B. Gasbaoui, A. Chaker, A. Laoufi, B. Allaoua, and A. Nasri, "The efficiency of direct torque control for electric vehicle behavior improvement," *Serbian Journal of Electrical Engineering*, vol. 8, no. 2, pp. 127–146, 2011.
- [13] A. Athari, S. Fallah, B. Li, A. Khajepour, S. Chen, and B. Litkouhi, "Optimal torque control for an electric-drive vehicle with in-wheel motors: implementation and experiments," *SAE International Journal of Commercial Vehicles*, vol. 6, no. 1, pp. 82–92, 2013.
- [14] H. Chen, J. Yang, Z. Du, and W. Wang, "Adhesion control method based on fuzzy logic control for four-wheel driven electric vehicle," *SAE International Journal of Passenger Cars-Mechanical Systems*, vol. 3, no. 1, pp. 217–225, 2010.
- [15] W. Kim, K. Yi, and J. Lee, "Development of a driving control algorithm and performance verification using real-time simulator for a 6WD/6WS vehicle," *Training*, vol. 2005, pp. 12–15, 2011.
- [16] S. Yun, K. Yi, S. Cheon, and Y. Yoon, "Development of a motor Torque distribution strategy of six-wheel-driven electric vehicles for optimized energy consumption," *Training*, vol. 2014, pp. 7–21, 2013.
- [17] L. de Novellis, A. Sorniotti, and P. Gruber, "Optimal wheel torque distribution for a four-wheel-drive fully electric vehicle," *SAE International Journal of Passenger Cars: Mechanical Systems*, vol. 6, no. 1, pp. 128–136, 2013.
- [18] H. B. Pacejka, E. Bakker, and L. Nyborg, "Tyre modelling for use in vehicle dynamics studies," *SAE Paper 870421*, SAE, 1987.
- [19] F. A. C. Viana, G. Venter, and V. Balabanov, "An algorithm for fast optimal Latin hypercube design of experiments," *International Journal for Numerical Methods in Engineering*, vol. 82, no. 2, pp. 135–156, 2010.
- [20] R. Hooke and T. A. Jeeves, "Direct search 'solution of numerical and statistical problems,'" *Journal of the ACM*, vol. 8, pp. 212–229, 1961.

## Research Article

# Optimal Control Strategy Design Based on Dynamic Programming for a Dual-Motor Coupling-Propulsion System

Shuo Zhang, Chengning Zhang, Guangwei Han, and Qinghui Wang

*National Engineering Laboratory for Electric Vehicles, School of Mechanical Engineering, Beijing Institute of Technology, Beijing 100081, China*

Correspondence should be addressed to Shuo Zhang; 2120110462@bit.edu.cn

Received 7 June 2014; Accepted 10 July 2014; Published 23 July 2014

Academic Editor: Rui Xiong

Copyright © 2014 Shuo Zhang et al. This is an open access article distributed under the Creative Commons Attribution License, which permits unrestricted use, distribution, and reproduction in any medium, provided the original work is properly cited.

A dual-motor coupling-propulsion electric bus (DMCPEB) is modeled, and its optimal control strategy is studied in this paper. The necessary dynamic features of energy loss for subsystems is modeled. Dynamic programming (DP) technique is applied to find the optimal control strategy including upshift threshold, downshift threshold, and power split ratio between the main motor and auxiliary motor. Improved control rules are extracted from the DP-based control solution, forming near-optimal control strategies. Simulation results demonstrate that a significant improvement in reducing energy loss due to the dual-motor coupling-propulsion system (DMCPS) running is realized without increasing the frequency of the mode switch.

## 1. Introduction

The application of battery electric vehicle in public transport field is a good way to improve the increasing air pollution and shortage of oil resources problems. Developing the electric bus has significant meanings for energy saving, emission reduction, and the electric vehicle (EV) industry development. The control of high-power drive system is one of the key technologies for electric bus. Dual-motor drive coupled by planetary gear is an effective way to realize the high-power drive system. Owing to the dual-power source nature, the control strategy of DMCPEB is typically more complicated than that of traditional engine based vehicle. Therefore, system-level vehicle simulation methodology is often applied to implement accurate sizing and matching studies and to develop effective energy control method, before the final design and physical prototyping.

The power control strategy for electric vehicle can be roughly classified into three categories (see [1, 2]). The first type employs heuristic control techniques such as control rules/fuzzy logic/neural networks for estimation and control algorithm development (see [3, 4]). The second approach is based on static optimization methods (see [5, 6]). The third type of EV control algorithms considers the dynamic

nature of the system when performing the optimization (see [7–9]). In addition, the optimization is with respect to a time horizon, rather than for an instant in time. In general, power split algorithms resulting from dynamic optimization approaches are more accurate under transient conditions but are computationally more intensive.

In this paper, dynamic programming (DP) technique is applied to solve the optimal control strategy problem of a DMCPEB. The optimal control strategy solution over a driving cycle is obtained by minimizing a defined cost function. Two cases are solved: an energy-loss-only case and an energy-loss/shifting-frequency case. The comparison of these two cases provides insight into the change needed when the additional objective of riding comfort is included. However, the DP control actions are not implementable due to their preview nature and heavy computational requirement. They are, on the other hand, a good design tool to analyze, assess, and adjust other control strategies. After studying the behavior of the dynamic programming solution carefully, we extract implementable rules. These rules are used to improve a simple, intuition-based algorithm. It was found that the performance of the rule-based algorithm can be improved significantly.

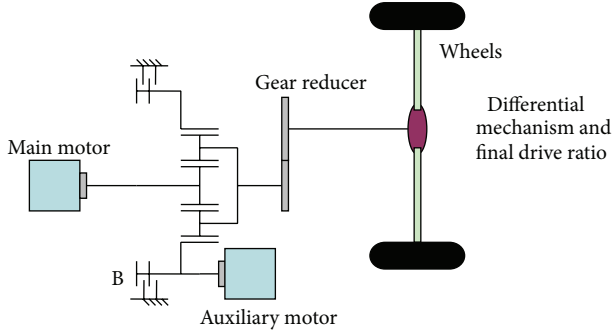


FIGURE 1: The dual-motors coupling-propulsion electric bus model configuration.

TABLE 1: Basic parameters of the vehicle and DMCPs.

Name	Value	Unit
Vehicle mass ( $M_{\text{vehicle}}$ )	18000	kg
Tire radius ( $r$ )	0.4785	m
Rolling resistance coefficient ( $f$ )	0.015	Null
Windward area ( $A$ )	7.5438	m <sup>2</sup>
Air resistance coefficient ( $C_D$ )	0.8	Null
Final drive ratio $i_0$	6.34	Null
Maximum torque of the motor ( $T_{\text{max}}$ )	410	Nm
Maximum rotate speed of the motor ( $N_{\text{max}}$ )	6000	rpm
Characteristic parameter of PGT ( $K$ )	3.5	Null

The paper is organized as follows. In Section 2, the dual-motor coupling-propulsion electric bus model is described, followed by an explanation of the preliminary rule-based control strategy. The dynamic optimization problem and the DP procedure are introduced in Section 3. The optimal results for the energy-loss-only and energy-loss/shifting-frequency optimization cases are given in Section 4. Section 5 describes the design of improved rule-based control strategies. Finally, conclusions are presented in Section 6.

## 2. DMCPEB Configuration and Preliminary Rule-Based Control Strategy

**2.1. DMCPEB Configuration and Modeling.** The target vehicle is a conventional bus whose engine and part transmission were replaced by a DMCPs developed by Beijing Institute of Technology [10]. The schematic of the vehicle is given in Figure 1. The power source was the main motor and auxiliary motor and the two powers coupled together through a planetary gear train. The main motor is connected to the sun gear while the auxiliary motor is connected to the ring gear. The coupled power output through planet carrier and the planet carrier was linked to the wheels by transmission system. B stands for a wet clutch which can realize mode switch by locking the ring gear smoothly. Important parameters of the vehicle and DMCPs are given in Table 1.

**2.2. Preliminary Rule-Based Control Strategy.** Compared with HEV, BEV's power management strategy seems much simpler, as most of BEVs only have one driving motor which means that the output power of motor is directly determined by the driver's power requirement. For two-motor coupled driving system, there are four possible operating modes: one-motor driving, two-motor driving, one-motor regenerative braking, and two-motor regenerative braking. In order to reduce the energy loss, the power management controller has to decide which operating mode to use and determine the proper power split between the two power sources while meeting the driver's demand. When the system is working in two-motor condition, the situation can be classified into torque coupling and speed coupling according to the structure of the driving system. For torque coupling driving system, the power split of power sources can be realized by determining the torque split, while, for the speed coupling driving system, the power split of power sources can be realized by determining the speed split between the two sources. The simple rule-based power management strategy was developed on the basis of engineering intuition and simple analysis of vehicle's driving characteristics and vehicle's dynamic requirements [11], which is a very popular design approach in electric vehicle. According to the vehicle status, the operation of the controller is determined by one of the two control modes: mode switch control and power split control. The basic logic of each control rule is described below.

**Mode Switch Control.** Based on the working property of the driving system and the efficiency map of the motor, if the vehicle speed exceeds  $v_{p+}$  or is below  $v_{p-}$ , the mode switch control will be applied to determine whether the auxiliary motor works or not, as shown in (2). The relationship of  $v_{p-}$  and  $v_{p+}$  can be expressed as follows:

$$v_{p-} = v_{p+} - A, \quad (1)$$

$$\begin{aligned} \text{one-motor to two-motor} \quad & v_{\text{vehicle}} > v_{p+}, \quad P_{\text{require}} \geq 0, \\ \text{two-motor to one-motor} \quad & v_{\text{vehicle}} < v_{p-}, \quad P_{\text{require}} < 0. \end{aligned} \quad (2)$$

The speed discrepancy  $A$  is to avoid continual mode switch which will influence the vehicle ride comfort.

**Power Split Control.** As this vehicle's driving system is speed coupling mode, the power split ratio is proportional to the speed ratio. There are two situations in terms of the power split control. In one-motor working situation, the driving system does not need power split control. The main motor will provide all the needed power, according to the vehicle speed and the pedal motion. In two-motor working situation, considering the motor's efficiency property the main motor will be working on the fixed relative high speed point  $N_{\text{main}}$  and the auxiliary motor speed will change according to the vehicle speed requirements. The output torque of motors will change simultaneously according to the pedal motion.

The detailed information of the speed split can be expressed as follows:

$$\begin{aligned}
 N_s &= \frac{S_{\text{vehicle}} \times 60 \times (1 + K)}{3.6 \times R_{\text{tire}} \times 2\pi \times i_0 \times i_2} \text{ one-motor mode,} \\
 Nr &= 0, \\
 N_s &= N_{\text{main}}, \\
 Nr &= \frac{S_{\text{vehicle}} \times 60 \times (1 + K)}{3.6 \times R_{\text{tire}} \times 2\pi \times i_0 \times i_2 \times K} - \frac{N_s}{K} \text{ two-motor mode,}
 \end{aligned} \tag{3}$$

where  $N_s$  is the speed of main motor, which is connected to the sun gear directly, and  $N_r$  is the speed of auxiliary motor, which is connected to the ring gear directly.  $K$  can be got by  $K = Z_r/Z_s$ ,  $Z_r$  and  $Z_s$  is the number of tooth for ring gear and sun gear.

### 3. Dynamic Optimization Problem

Compared with rule-based algorithms, the dynamic optimization approach can find the best control strategy relying on a dynamic model (see [12, 13]). Given a driving cycle, the DP-based algorithm can obtain the optimal operating strategy minimizing the system's energy loss subject to the diverse constraints. A numerical-based DP approach is adopted in this paper to solve this finite horizon dynamic optimization problem.

*3.1. Problem Formulation.* In the discrete-time format, a model of the battery electric vehicle can be expressed as

$$x(k+1) = f(x(k), u(k)), \tag{4}$$

where  $u(k)$  is the vector of control variables such as shifting command of the driving system and desired speed ratio increments of the auxiliary motor.  $x(k)$  is the state vector of the system such as the working mode of the system (one-motor mode or two-motor mode) and the speed ratio of the motors. The sampling time for the control problem is selected to be one second. The optimization goal is to find the control input  $u(k)$  to minimize a cost function, which consists of the weighted sum of energy loss and the frequency of the mode change. The cost function to be minimized has the following form:

$$\begin{aligned}
 J &= \sum_{k=0}^{N-1} L(x(k), u(k)) \\
 &= \sum_{k=0}^{N-1} L_m(k) + L_a(k) + L_c(k) + \alpha \times |\text{Shift}(k)|,
 \end{aligned} \tag{5}$$

where  $N$  is the duration of the driving cycle and  $L$  is the instantaneous cost including main-motor energy loss  $L_m(k)$ , auxiliary-motor loss  $L_a(k)$ , power-coupling gear-box loss  $L_c(k)$ , and mode change cost  $\alpha \times |\text{Shift}(k)|$ . For an energy-only problem, the weighting factor  $\alpha$  is set to be zero. The case  $\alpha > 0$  represents a comprehensive problem which considered

the energy loss and the number of mode changes. During the optimization, it is necessary to impose the following inequality constraints to ensure safe/reasonable operation of the main motor and auxiliary motor:

$$\begin{aligned}
 T_{s.\text{min}}(N_s(k)) &\leq T_s(N_s(k)) \leq T_{s.\text{max}}(N_s(k)), \\
 N_{s.\text{min}} &\leq N_s(k) \leq N_{s.\text{max}}, \\
 T_{r.\text{min}}(N_r(k)) &\leq T_r(N_r(k)) \leq T_{r.\text{max}}(N_r(k)), \\
 N_{r.\text{min}} &\leq N_r(k) \leq N_{r.\text{max}},
 \end{aligned} \tag{6}$$

where  $T_s$  is the output torque of the main motor and  $T_r$  is the output torque of the auxiliary motor. In addition, to satisfy the systems properties, besides this basic constraints, other constraints are needed:

$$N_s(k) \times N_r(k) \geq 0, \tag{7}$$

this constrain is to avoid the power cycling which can increase power loss greatly and is undesirable in reality. Another constrain is that when  $N_s = 0$ , the speed of  $N_r$  should also be zero. This is because our current system only has one wet clutch and it is fixed with the ring gear. This means that when the vehicle is running, the sun gear must be running too.

*3.2. Model Simplification.* The detailed DMCPs and DMCPeB models are not suitable for dynamic optimization due to their high number of states. Thus, a simplified but sufficiently complex vehicle model is developed. This DMCPs is a speed coupling system and can be classified into two working modes (one-motor working mode and two-motor working mode). As the two aspects are the main influence factors when the DMCPs's parameters are determined, it was decided that only these two state variables needed to be kept: the two motors' speed ratio and DMCPs's working mode. The simplifications of the subsystems motors, vehicle, transmission, battery, and the planetary gear train are described below.

*Motors.* The electric motor characteristics are based on the efficiency data obtained from [10] as shown in Figure 2. From Table 1 we can get that though the DMCPs needs two motors, they have the same specifications and they are of the same type. So here we only display one efficiency map of the electric motor. Considering the regenerative braking, here we assume that when the output torque of motor is negative, the efficiency is the same as when the motor output positive torque whose value is the same as the absolute value of the negative torque. The motor efficiency  $\eta_m$  can be expressed as

$$\eta_m = f(|T_m(N_m)|, N_m), \tag{8}$$

where  $|T_m|$  is the absolute value of the motor's output torque and  $N_m$  is the rotate speed of the motor. When the vehicle is braking in emergency condition, the DMCPs cannot provide enough braking force. Here the braking strategy is determined to be series strategy: when the DMCPs can provide enough brake force, all the brake force will be provided by the DMCPs, and when the needed brake force

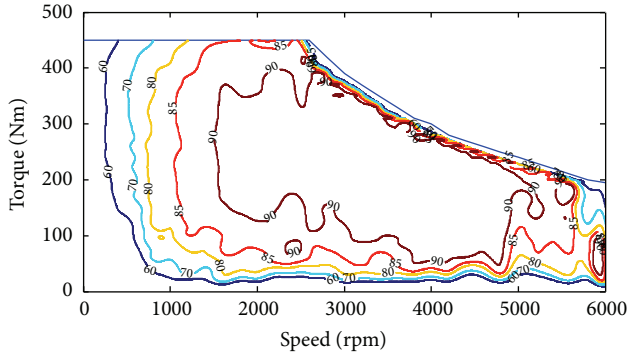


FIGURE 2: Efficiency map of the electric motor.

exceeds the DMCPs's ability, the DMCPs will provide the maximum torque while the extra force will be provided by the friction braking system. The output torque  $T_m(N_m)$  can be expressed as follows:

$$|T_m(N_m)| = \begin{cases} |T_{m,req}| & \text{if } |T_{m,max}(N_m)| \geq |T_{m,req}| \\ |T_{m,max}(N_m)| & \text{if } |T_{m,max}(N_m)| < |T_{m,req}| \end{cases}, \quad (9)$$

where  $T_{m,req}$  is the required torque.

*Vehicle.* The vehicle is modeled as a point mass:

$$V_{vehicle}(k+1) = V_{vehicle}(k) + \frac{\left( (T_s(k) \times (1+K) \times i_0 \times i_2 - T_b(k)) - F_f - F_a(V_{vehicle}(k)) \right) (M_r)^{-1}}{r_t}, \quad (10)$$

where  $T_b(k)$  is the friction brake force,  $i_0$  is the reduction ratio of the gear reducer,  $K$  is the property parameter of the planetary gear train,  $F_f$  and  $F_a$  are the rolling resistance force and the aerodynamic drag force, respectively,  $r_t$  is the tire radius,  $M_r$  is the effective mass of the vehicle, and  $J_r$  is the equivalent moment of inertia of the rotating components in the vehicle.  $F_f$ ,  $F_a$ , and  $M_r$  can be got from the following equations:

$$\begin{aligned} F_f &= M_{vehicle} \times g \times f, \\ F_a &= \frac{C_D A u_a}{21.5}, \\ M_r &= M_{vehicle} + \frac{J_r}{r_t^2}, \end{aligned} \quad (11)$$

where  $M_{vehicle}$  is the mass of the vehicle,  $g$  is the gravity acceleration,  $f$  is the rolling resistance coefficient,  $C_D$  is

aerodynamic drag coefficient,  $A$  is the effective projected area of vehicle, and  $u_a$  is the speed of the vehicle.

*Transmission.* The working modes (one-motor working mode and two-motor working mode) are modeled as a discrete-time dynamic system with 1 s time increment

$$m_x(k+1) = \begin{cases} 1, & m_x(k) + \text{Shift}(k) > 1 \\ 0, & m_x(k) + \text{Shift}(k) < 0 \\ m_x(k) + \text{Shift}(k), & \text{otherwise,} \end{cases} \quad (12)$$

where state  $m_x$  is the main working mode and the control shift to the transmission is constrained to take on the values of  $-1, 0$  and  $1$ , representing downshift, sustain and upshift, respectively.

*The Battery.* The Lithium-Ion Battery is used. A lot of work has been done about estimating the state of charge (SOC) of the battery [14–16], which is very important for HEV and BEV. As this paper mainly focused on the DMCPs and for the BEV the batteries just provide the needed power and cannot be optimized as the needed power is fixed according to the certain drive cycle, here we assume that the battery can always meet the drive cycle's power requirement and no energy loss is coming from the battery.

*The Planetary Gear Train.* Based on the planetary gear train's working property, we can get that different control strategy can also lead to the different energy loss due to the different efficiency, and so the planetary gear train's efficiency model should also be built to calculate the energy loss. As the planetary gear train is a TWO-DOF mechanism, the efficiency  $\eta_E$  can be got from the following formula [17]:

$$\begin{aligned} \eta_{Ea} &= \frac{N_c}{N_s / (1-K) \eta_{r(s-c)} - N_r K / (1-K) \eta_{s(r-c)}} \\ \eta_{Ed} &= \frac{K p \eta_{s(c-r)} N_r + \eta_{r(c-s)} N_s}{(1+Kp) N_c}, \end{aligned} \quad (13)$$

where  $\eta_{Ea}$  stands for the efficiency when the vehicle is accelerating,  $\eta_{Ed}$  stands for the efficiency when the vehicle is decelerating,  $\eta_{r(s-c)}$  denotes the efficiency that when the ring gear is fixed, the power is input into the sun gear and output from planet carrier, and  $\eta_{s(r-c)}$  denotes the efficiency that when the sun gear is fixed, the power is input into the ring gear and output from planet carrier.  $\eta_{s(c-r)}$  denotes the efficiency that when the sun gear is fixed, the power is input into the planet carrier and output from ring gear, and  $\eta_{r(c-s)}$  denotes the efficiency that when the ring gear is fixed, the power is input into the planet carrier and output from sun gear.

*3.3. Dynamic Programming Method.* The DP technique is based on Bellman's Principle of Optimality, which states that the optimal policy can be obtained if we first solve a one stage subproblem involving only the last stage and then gradually extend to subproblems involving the last two stages, last three

stages, . . . , and so forth, until the entire problem is solved. In this manner, the overall dynamic optimization problem can be decomposed into a sequence of simpler minimization problems as follows (see [18, 19]).

Step  $N - 1$ : consider

$$J_{N-1}^*(x(N-1)) = \min_{u(N-1)} [L(x(N-1), u(N-1)) + G(x(N))]. \quad (14)$$

Step  $k$ : for  $0 \leq k < N - 1$ ,

$$J_k^*(x(k)) = \min_{u(k)} [L(x(k), u(k)) + J_{k+1}^*(x(k+1))], \quad (15)$$

where  $J_k^*(x(k))$  is the optimal cost-to-go function or optimal value function at state  $x(k)$  starting from time stage  $k$ . It represents the optimal cost that if at stage  $k$  the system starts at state  $x(k)$  and follows the optimal control law thereafter until the final stage. The above recursive equation is solved backward to find the optimal control policy. The minimizations are performed subject to the inequality constraints shown in (6) and the equality constraints imposed by the driving cycle.

**3.4. Numerical Computation.** As the DMCPs is a nonlinear system, this DP has to be solved numerically by some approximations. A standard way to solve (15) numerically is to use quantization and interpolation (see [2, 18]). For continuous state space and control space, the state and control values are first discretized into finite grids. At each step of the optimization search, the function  $J_k(x(k))$  is evaluated only at the grid points of the state variables. If the next state  $x(k+1)$  does not fall exactly on a quantized value, then the values of  $J_k^*(x(k))$  in (15) as well as  $G(x(N))$  in (14) are determined through linear interpolation.

### 4. Dynamic Programing Results

The DP procedure described above produces an optimal, time-varying, state-feedback control law. In the following, two cases are presented: energy-loss-only problem and energy-loss/ mode-change problem.

**4.1. Energy-Loss Optimization Results.** When optimizing for only fuel economy, the weighting  $\alpha$  is set to zero. The Chinese typical city drive cycle is used. The simulation results of the vehicle under the DP policy are shown in Figures 3, 4, and 5. From Figures 3 and 4 we can get that when the vehicle speed is low, the main motor is going to provide the needed speed and power, and when the vehicle speed is high, the motor speed tends to decrease to a very low point and the most vehicle speed and power will be provided by the auxiliary motor. This is because the motor efficiency will be much lower in the working condition of high speed and low output torque. From Figure 2 we can get that the motor efficiency will also be low in the working condition of low speed and low output torque, but in this condition the output power is also low, so

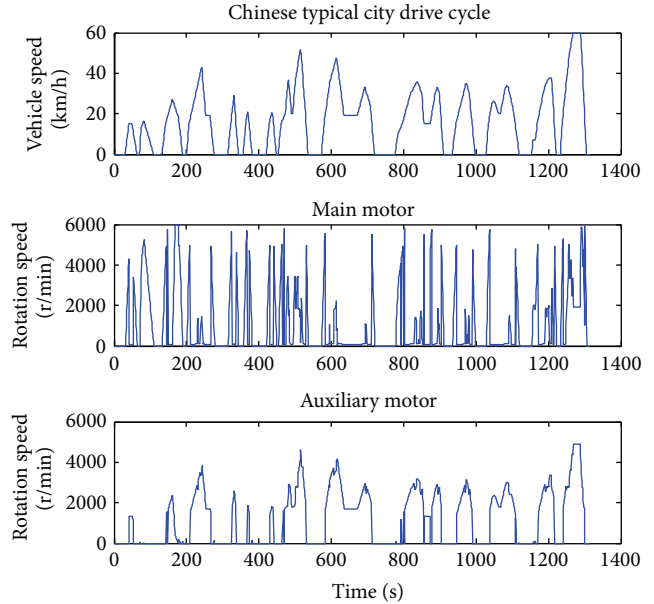


FIGURE 3: The rotating speed of the two motors.

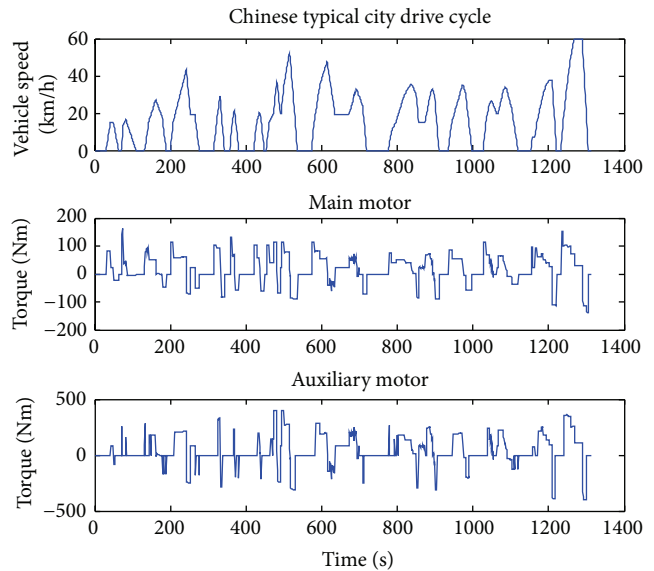


FIGURE 4: The output torque of the two motors.

the energy loss is lower than that in high speed. Compared with the main motor, the auxiliary motor tends to work on the high speed and high torque condition which is within high efficiency location.

From Figure 5 we can get that the DMCPs's energy loss can be classified into three categories: main motor loss, auxiliary motor loss, and coupling box loss. Among them the auxiliary loss accounts for the main part, while the main motor loss and coupling box loss are almost equal. This is because the auxiliary motor is always working in the high power condition although its working efficiency is relatively higher than the main motor.

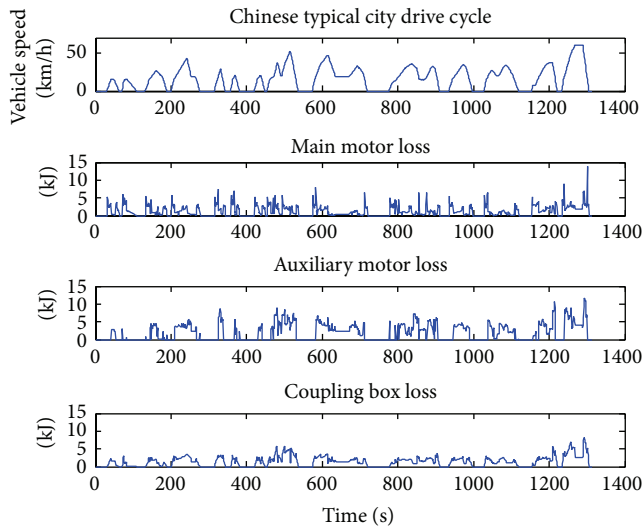


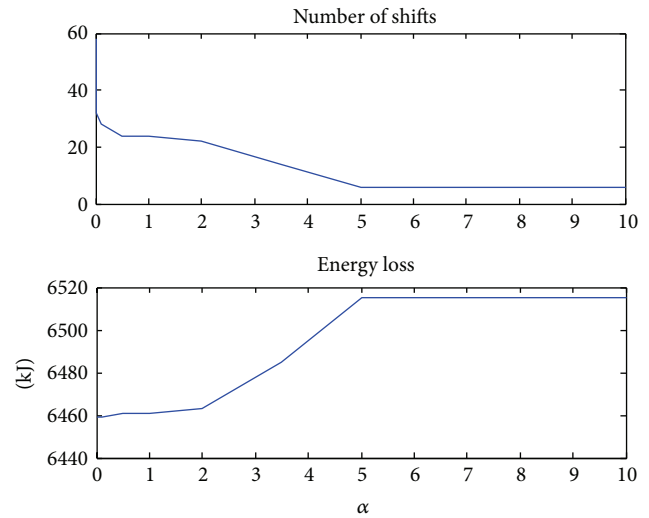
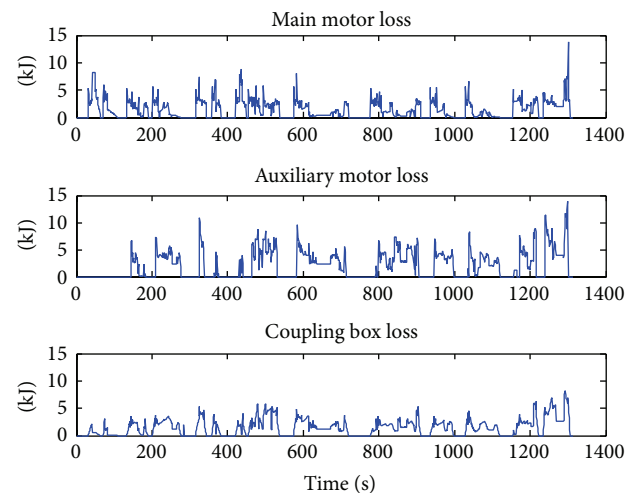
FIGURE 5: Energy-loss distribution.

**4.2. Energy Loss and Shifting Frequency Optimization Results.** To study the tradeoff between energy loss and shifting frequency the weight factors are varied  $\alpha = [0, 0.01, 0.1, 0.5, 1, 2, 3.5, 5, 10]$ . The possible values of  $\alpha$  are chosen based on the reasonable meanings in formula (5). This tradeoff study is important in the early design process because it provides useful information about the sensitivity between the energy loss and shifting frequency. The trend of the energy loss and the number of shifts with the change of  $\alpha$  are shown in Figure 6. From Figure 6 we can get that when  $\alpha < 1$ , the number of shifts decreased rapidly (from 58 to 24) with the increase of  $\alpha$  while the energy loss increased only a little which can be neglected. When  $\alpha$  increases between 1 and 2, the energy loss and number of shifts only change a little. When  $\alpha$  increases from 2 to 5, the number of shifts decreases fast again and the energy loss increases fast. When  $\alpha$  exceeds 5, both the number of shifts and the energy loss stay constant. So the reasonable value will be between 1 and 2. Here we set  $\alpha = 2$  for further discussion.

From Figure 7 we can get that to reduce the number of shifts the main motor tends to work more in the low speed. Compared with Figure 5, the number of shifts reduces from 58 to 22, which is only 38% of the original DP results, while the energy loss increased from 5943 to 6431 KJ, which only increased 8.2%.

## 5. Development of Improved Rule-Based Controls

The DP control policy is not implementable in real driving conditions because it requires knowledge of future speed and load profile. Nonetheless, analyzing its behavior provides useful insight into possible improvement of the rule-based controller. Based on the above discussion simulation results, here we abstract the shift control strategy including upshift and downshift strategy and power split strategy.

FIGURE 6: The trend of the energy loss and number of shifts with the change of  $\alpha$ .FIGURE 7: Energy-loss distribution for  $\alpha = 2$ .

**5.1. Working Mode Shift Control.** The working mode shift is crucial to the reduction of energy loss and riding comfort. In the original DP results the DMCPs needs frequent shifting to reduce the energy loss, which may influence the riding comfort, and when  $\alpha = 2$ , the energy loss did not increase a lot but the shifting number is only 38% of the original DP result. Figures 8 and 9 show the abstracting procedure of the downshifting and upshifting threshold based on the DP results data when  $\alpha = 2$ . In Figure 8 the first graph shows the working condition when the vehicle is accelerating, while the second graph shows the working condition when the vehicle is braking. By drawing a line manually to depart the working mode the shifting strategy can be got. The merit of this work compared with other methods is that this method not only determined the reasonable shifting point but also helped us decide when to upshift and downshift, which can avoid

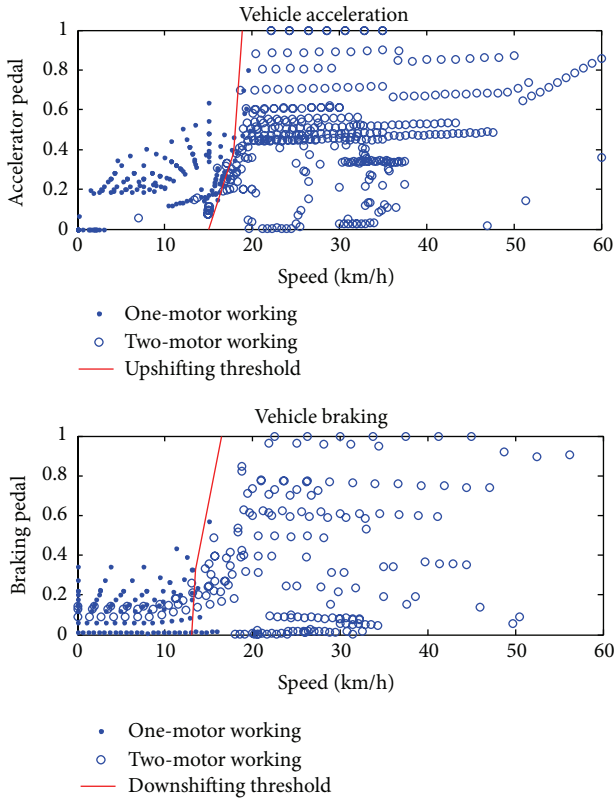


FIGURE 8: Abstracting of shifting strategy.

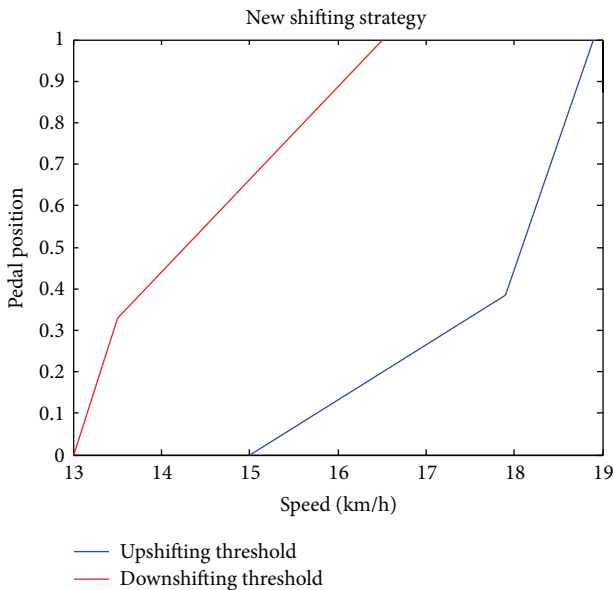


FIGURE 9: New shifting strategy.

frequent shifting in application. And the result is expressed in Figure 9.

5.2. Power Split Control. In this section, we study how power split control of the preliminary rule-based algorithm can be

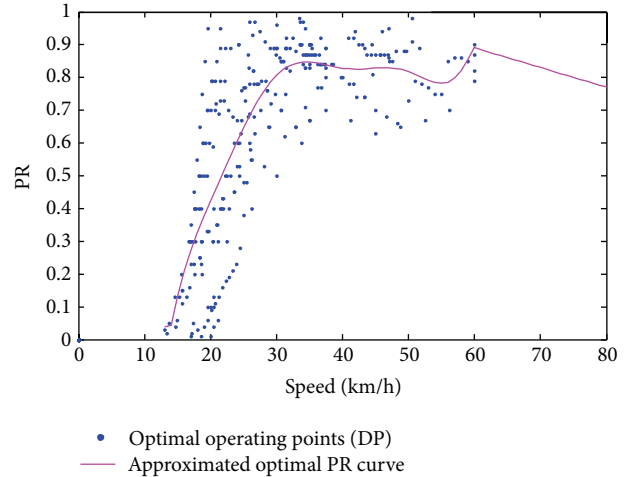


FIGURE 10: New power split strategy.

improved by analyzing the DP results when  $\alpha = 2$ . The power split ratio PR can be expressed as follows:

$$PR = \frac{P_r}{P_r + P_s} \tag{16}$$

Two working modes are defined: single motor working mode ( $PR = 0$ ) and power coupling working mode ( $0 < PR < 1$ ). It should be noted that the range of PR is [0,1]. In one-motor working mode ( $PR = 0$ ), as above discussed the control rule is unique. Here we only talk about the coupling condition. Figure 10 gives the new power split strategy abstracted from the data based on DP results. It can be seen from the curve that the split ratio tends to fluctuate around 0.77 when the speed exceeds 20 km/h; this is because the planet mechanism's property parameter  $K$  is set to 3.5 and in this ratio the efficiency of coupling box is relatively higher than other ratios. This demonstrates that though the energy loss from coupling box is not the most compared one with the auxiliary motor, it plays an important role in reducing the energy loss.

5.3. Performance Evaluation. After incorporating the working mode shift control and power split control outlined in the previous sections, the improved rule-based controller is evaluated using Chinese typical city drive cycle. Table 2 shows the comparison of different control rules. We can get from the table that the new rule-based strategy can reduce the DMCPs's energy loss effectively. Specifically, the main loss is coming from the main motor in the preliminary rule-based strategy while in the new rule-based strategy and DP operation the main loss is coming from the auxiliary motor. Though the new rule-based strategy reduces the energy loss by about 22%, the DMCPs still has a significant reducing potential as the DP operation reduces the energy loss by 36.9%. From Table 3 we can get that the new rule-based strategy does not need to increase the shifting number but cannot improve the shifting performance too. On the contrary DP ( $\alpha = 2$ ) can realize reducing the shifting number by about 15.34%.

TABLE 2: Comparison of different control strategy in energy loss.

Loss type	Main motor (KJ)	Auxiliary motor (KJ)	Coupling box (KJ)	Total (KJ)	Improvement in total (%)
Preliminary rule-based	5302	2781	2158	10240	0%
New rule-based	2938	3017	2030	7987	22%
DP ( $\alpha = 2$ )	1848	2691	1922	6461	36.9%

TABLE 3: Comparison of different control strategy in shifting number.

	Shifting number	Improvement in total (%)
Preliminary rule-based	26	0%
New rule-based	26	0%
DP ( $\alpha = 2$ )	22	15.34%

## 6. Conclusion

Based on the simplified model, DP is applied to solve the globally optimal control strategy. Designing the control strategy for DMCPEB by extracting rules from the dynamic programming results has the clear advantage of being near optimal, accommodating multiple objectives, and systematic. Depending on the overall objective, one can easily develop control laws that emphasize low energy loss and riding comfort. By analyzing the DP results the approximate optimal upshift threshold, downshift threshold, and power split ratio were determined. The improved rule-based control strategy can reduce the energy loss by about 22%, while the DP ( $\alpha = 2$ ) can reduce the energy loss by 36.9%.

## Conflict of Interests

The authors declare that there is no conflict of interests regarding the publication of this paper.

## Acknowledgments

The authors gratefully acknowledge the support from the National Natural Science Foundation of China (Grant no. 51175040) and the Research Fund for the Doctoral Program of Higher Education of China (Grant no. 20111101110037).

## References

- [1] Y. Zou, H. Shi-Jie, L. Dong-Ge, G. Wei, and X. Hu, "Optimal energy control strategy design for a hybrid electric vehicle," *Discrete Dynamics in Nature and Society*, vol. 2013, Article ID 132064, 8 pages, 2013.
- [2] C. C. Lin, H. Peng, J. W. Grizzle, and J. M. Kang, "Power management strategy for a parallel hybrid electric truck," *IEEE Transactions on Control Systems Technology*, vol. 11, no. 6, pp. 839–849, 2003.
- [3] B. M. Baumann, G. Washington, B. C. Glenn, and G. Rizzoni, "Mechatronic design and control of hybrid electric vehicles," *IEEE/ASME Transactions on Mechatronics*, vol. 5, no. 1, pp. 58–72, 2000.
- [4] N. J. Schouten, M. A. Salman, and N. A. Kheir, "Fuzzy logic control for parallel hybrid vehicles," *IEEE Transactions on Control Systems Technology*, vol. 10, no. 3, pp. 460–468, 2002.
- [5] C. Kim, E. NamGoong, and S. Lee, "Fuel economy optimization for parallel hybrid vehicles with CVT," SAE Paper 1999-01-1148, 1999.
- [6] G. Paganelli, G. Ercole, A. Brahma, Y. Guezennec, and G. Rizzoni, "A general formulation for the instantaneous control of the power split in charge-sustaining hybrid electric vehicles," in *Proceedings of the 5th International Symposium on Advanced Vehicle Control*, Ann Arbor, Mich, USA, 2000.
- [7] A. Brahma, Y. Guezennec, and G. Rizzoni, "Dynamic optimization of mechanical electrical power flow in parallel hybrid electric vehicles," in *Proceedings of the 5th International Symposium on Advanced Vehicle Control*, Ann Arbor, Mich, USA, 2000.
- [8] U. Zoelch and D. Schroeder, "Dynamic optimization method for design and rating of the components of a hybrid vehicle," *International Journal of Vehicle Design*, vol. 19, no. 1, pp. 1–13, 1998.
- [9] C.-C. Lin, J. Kang, J. W. Grizzle, and H. Peng, "Energy management strategy for a parallel hybrid electric truck," in *Proceedings of the American Control Conference*, pp. 2878–2883, Arlington, Va, USA, June 2001.
- [10] X. H. Wu, *Matching and control strategy of dual motors coupled driving system on electric buses [Ph.D. thesis]*, Institute of Technology, Beijing, China, 2011.
- [11] P. D. Bowles, *Modeling and energy management for a parallel hybrid electric vehicle (PHEV) with continuously variable transmission (CVT) [M.S. thesis]*, University of Michigan, Ann Arbor, Mich, USA, 1999.
- [12] H. He, H. Tang, and X. Wang, "Global optimal energy management strategy research for a plug-in series-parallel hybrid electric bus by using dynamic programming," *Mathematical Problems in Engineering*, vol. 2013, Article ID 708261, 11 pages, 2013.
- [13] R. Wang and S. M. Lukic, "Dynamic programming technique in hybrid electric vehicle optimization," in *Proceedings of the IEEE International Electric Vehicle Conference (IEVC '12)*, pp. 1–8, Greenville, SC, USA, March 2012.
- [14] R. Xiong, X. Gong, C. C. Mi, and F. Sun, "A robust state-of-charge estimator for multiple types of lithium-ion batteries using adaptive extended Kalman filter," *Journal of Power Sources*, vol. 243, pp. 805–816, 2013.
- [15] R. Xiong, F. Sun, X. Gong, and C. Gao, "A data-driven based adaptive state of charge estimator of lithium-ion polymer battery used in electric vehicles," *Applied Energy*, vol. 113, pp. 1421–1433, 2014.
- [16] R. Xiong, F. Sun, Z. Chen, and H. He, "A data-driven multi-scale extended Kalman filtering based parameter and state estimation approach of lithium-ion polymer battery in electric vehicles," *Applied Energy*, vol. 113, pp. 463–476, 2014.

- [17] E. Pennestri, L. Mariti, P. P. Valentini, and V. H. Mucino, "Efficiency evaluation of gearboxes for parallel hybrid vehicles: theory and applications," *Mechanism and Machine Theory*, vol. 49, pp. 157–176, 2012.
- [18] D. P. Bertsekas, *Dynamic Programming and Optimal Control*, Athena Scientific, Belmont, Mass, USA, 1995.
- [19] Y. Zou, S. Hou, E. Han, L. Liu, and R. Chen, "Dynamic programming-based energy management strategy optimization for hybrid electric commercial vehicle," *Automotive Engineering*, vol. 34, no. 8, pp. 663–668, 2012.